11-1-1999

Fabrication of phase masks and microlenses using binary optics

Joseph Summa

FABRICATION OF PHASE MASKS AND MICROLENSES USING BINARY OPTICS

by

Joseph R. Summa
B.S. Rochester Institute of Technology
(1991)

A thesis submitted in partial fulfillment of the
Requirements for the degree of Master of Science
In the Chester F. Carlson Center for Imaging Science
of the College of Science
Rochester Institute of Technology

November 1999

Signature of the Author _____

Accepted by Henry E. Rhody 11/10/99
Coordinator, M.S. Degree Program Date

CHESTER F. CARLSON
CENTER FOR IMAGING SCIENCE
COLLEGE OF SCIENCE
ROCHESTER INSTITUTE OF TECHNOLOGY
ROCHESTER, NEW YORK

CERTIFICATE OF APPROVAL

M.S. DEGREE THESIS

The M.S. Degree Thesis of Joseph R. Summa
has been examined and approved by the
thesis committee as satisfactory for the
thesis requirement for the
Master of Science degree

Dr. Bruce Smith, Thesis Advisor

Dr. Roger Easton

Dr. Richard Lane

11/10/99
Date

THESIS RELEASE PERMISSION
ROCHESTER INSTITUTE OF TECHNOLOGY
COLLEGE OF SCIENCE
CHESTER F. CARLSON
CENTER FOR IMAGING SCIENCE

Title of Thesis: Fabrication Of Phase Masks And Microlenses Using Binary Optics

I, Joseph Summa, hereby grant permission to the Wallace Memorial Library of R.I.T. to reproduce my thesis in whole or in part. Any reproduction will not be for commerical use of profit.

Signature: _____

Date: 11/15/99

FABRICATION OF PHASE MASKS AND MICROLENSES USING BINARY OPTICS

by

Joseph R. Summa

Submitted to the
Chester F. Carlson
Center for Imaging Science
College of Science
in partial fulfillment of the requirements
for the degree of Master of Science
at the Rochester Institute of Technology

ABSTRACT

A process for the fabrication of binary optics at the Rochester Institute of Technology was established and tested. A sacrificial aluminum layer was used to provide both a conductive substrate for electron beam exposure, and a clean highly resistant etch stop for reactive ion etching. This enabled the use of a low pressure CF_4 RIE process that minimized the rates of polymerization during etch and provided stable etch rates necessary to achieve 100 angstrom etch depth control. Alignment errors of up to 1 micron were attributed to stage drifts on the electron beam exposure system. No systematic errors were found to indicate problems with the MEBES alignment system and alignment mark detection.

Simulations of multiphase PSMs were performed using a program developed as a part of this work capable of simulating a 1024 pixel array of arbitrary magnitude and phase under conditions of partially coherent illumination. Cases of annular (off-axis) illumination and defocus are also allowed. The program has demonstrated rapid calculation as well as flexibility of user input using a graphical user interface.

A three-etch, 8-phase level binary optic process was used to produce phase shifting masks and a quartz microlens array. Submicron "chromeless" phase mask features were demonstrated and gradient phase transitions were successfully used to eliminate unwanted lines at phase boundaries. Although photoresist process limitations prevented the realization of significant benefits from phase shifting, the electrical metrology structures demonstrated the ability to rapidly gather CD data useful in identifying problem areas.

ACKNOWLEDGMENTS

I would like to thank my mentor Dr. Bruce Smith for imparting to me a small part of his knowledge of semiconductor lithographic processes and for rapidly debunking foolish ideas and flawed reasoning . Profound thanks also to Roger Easton for introducing me to the wonderful world of Fourier Analysis and intuition for the behavior of complex objects in coherent optical systems and Dr. Richard Lane for assistance with the Plasma Etch processes.

I am also indebted to Dr. Lynn Fuller and Advanced Micro Devices for their support of this work.

DEDICATION

To my wife Anna, without whom I would be (at best) only partially coherent myself.

TABLE OF CONTENTS

LIST OF FIGURES

LIST OF TABLES

INTRODUCTION

Semiconductor lithography has been driven by the constant desire for better spatial resolution to allow production of more densely packed, high-speed integrated circuits. Microlithography typically is performed by imaging a patterned glass plate (mask) through a reduction system using projection optics. Since these systems are essentially diffraction limited, optical resolution is simply a function of the numerical aperture (NA) and the wavelength of the illumination (X). Efforts to improve resolution have driven typical NA's increase from around 0.28 in the early 80's, to higher than 0.6 in current systems. In a similar fashion, operating wavelengths have been shortened from 436nm to 365nm and now are poised to extend into the deep ultraviolet region at wavelengths of 248, 193, and 157nm.

These advances have not been without technical difficulties. Increasing NA and decreasing wavelengths both reduce the usable depth of focus (DOF) of the system. Focal depth is essential for maintaining a stable and manufacturable process with variations in substrate topography and processing conditions. Another factor driving advanced photomask technology involves the costs of installing "next generation" equipment. Though the initial cost of these machines is considerable, often more significant are the long term costs associated with new (and more expensive) materials that require significant engineering time to develop into stable processes. For these reasons techniques to improve resolution without degradation of the DOF using the existing equipment and materials, have been the topic of considerable research.

There are two methods to improve the optical performance of a diffraction-limited lithographic system. The first is to increase the spatial bandwidth of the system. This essentially involves increasing NA and/or decreasing the wavelength of light used. The other method is to optimize or modify the available spatial information to produce a higher quality image. This can be accomplished either by modifying the mask, or through the use of spatial filtering at the pupil of the optical system. Mathematically, both approaches are equivalent. The first modifies the object in the space domain while the other makes changes at the frequency plane. In practice, certain operations are much easier to accomplish using one approach than the other due to practical limitations involved with the fabrication of the necessary masks and filters. In general, pattern-dependent modifications of a localized nature are best accomplished on the mask plane, while global operations such as focus shifting or band pass filtering are best attempted at the pupil plane.

Spatial filtering at the pupil plane has been largely neglected in semiconductor lithography due to the simple fact the no production equipment has been designed to make this plane accessible. The incorporation of a planar spatial filtering element into the pupil plane would be a source of spherical aberration that must be corrected through the modification of other lens elements. Since this approach can not be directly applied to existing systems, alteration of the spatial content of lithographic images may be best attempted at the image (mask) plane.

In a perfect projection imaging system the mask (image) would simply be a magnified version of the desired circuit pattern (object). Unfortunately optical systems act as a low

pass filters that produce lower contrast images of the object. This degraded image is by no means optimized for the patterning operation to be performed. Superior results can be realized by altering the mask pattern.

Imaging can be described as a process by which magnitude and phase information from an object are acted upon by an optical system to produce and image. Standard "binary" masks utilize two transmission levels (0 and 1) and constant phase. Simple optimizations of these designs involved simply biasing lines to produce the desired final linewidth. Serifs have been added to "square" corners in the images. Both techniques significantly improved image fidelity, even within the constants of a binary system.

In the early 1980's Levenson' applied the concept of phase-shift masking to semiconductor lithography. Initial work involved the addition of 180 degree phase retarders to alternating spaces in a grating. Later phase elements below 180 degrees (typically 90, or 120,60) were added to enable a gradual phase transitions from 180 to 0. The incorporation of phase information adds a new degree of freedom for mask designers.

Still the question remains, given complete freedom in mask design, i.e. the capability to produce continuous tone magnitude and phase elements, what design would produce the highest contrast images over the largest process window? The principle challenges associated with utilizing phase information to enhance lithographic performance can be placed in two categories. The first involves the capability to produce the desired phase levels on the mask. The second involves the ability to simulate and optimize complex objects under partially coherent illumination. Phase will be adjusted by etching trenches in fused silica substrates that correspond to the desired optical phase retardation. Multiple phase levels will be created using the *binary optics* approach used in the production of blazed gratings and quartz micro lenses. (See chapter 2). Simulations will be carried out using commercially available software based on the SPLAT algorithm developed at U.C. Berkeley[4] as well as a simplified (1-D) model developed as part of this thesis.

Together, the phase and attenuation elements in the proposed advanced photomask have the potential to improve the resolution capability of existing systems while extending the useful limits of conventional photolithography.

CHAPTER 1:

THEORY AND SIMULATION OF PARIALLY COHERENT IMAGERY

Introduction

Any discussion of the effect of complex (magnitude and phase) objects on optical system performance must be rooted in a fundamental understanding of the imaging processes involved. Typically, systems utilized in semiconductor lithography are 5X-reduction refractive optical systems that can be described fully with knowledge of the conditions of illumination, and the imaging properties of the objective lens. The objective is defined in terms of the angular size of the entering cone of light (the numerical aperture) and lens aberrations, while the illuminator or condenser lens defines the "coherence" of the system based on its (angular) size relative to that of the objective lens.

The following background discussion is based on Hopkin's theory[3] of partially coherent illumination. Computational algorithms developed by Kintner[7] and Subramanian[10] that utilize Hopkin's equations to simulate 1-D aerial images will also be reviewed. These algorithms serve as the basis for a computer program (described in Chapter 3) developed to simulate and optimize the phase masks produced as a part of this work.

The Quasimonochromatic Source

A pure monochromatic source would emit a continuous sinusoidal electromagnetic wave of constant amplitude and frequency (figure 1.1a). The Fourier transform of such a source would be pair of delta functions indicating the presence of that frequency (figure 1.1b). (Only the positive frequencies are shown). Elemental radiators in real sources (atoms) behave more like damped dipole oscillators. Light is emitted in short pulses that vary in amplitude. The electronic transitions that cause these disturbances have a duration on the order of 10^{-9} seconds[1]. A simple pulse can be modeled as a cosinusoidal wave (the central frequency ν_c) modulated by a gaussian envelope as shown in figure 1.1c. The width of this gaussian in the time domain is referred to as the coherence time (Δt) of the source. The Fourier spectrum of this wave packet is simply a delta function convolved with a gauss (figure 1.1d).

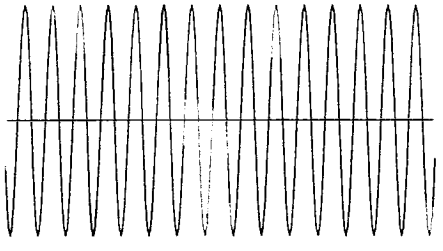

Figure 1.1(a)

Figure 1.1(b)

Illustration of a simple sinusoidal wave in time (a) and frequency (b) domains.

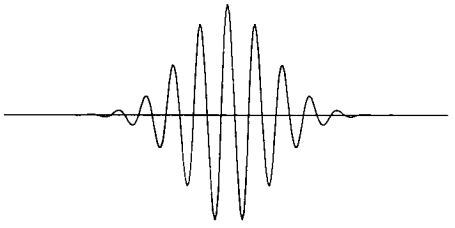

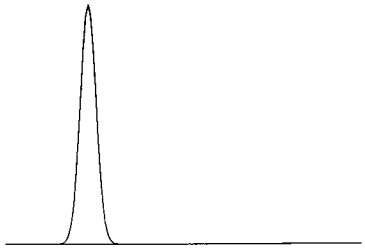

Figure 1.1c Figure 1.1d

Illustration of a pulse represented by a cosinusoidal wave modulated by a gaussian envelope in both time (c) and frequency (d) domains. This type of pulse can be used to approximate the behavior of elemental radiators (atoms) in real sources.

The width of the gaussian in the frequency domain is defined by the reciprocal of the coherence time (Δt) and termed the spectral bandwidth ($\Delta\nu=1/\Delta t$). Since the speed of light is known, a third parameter, the coherence length (Δl), can be calculated representing the average pulse length.

$$\Delta l = c\,\Delta t \qquad (1)$$

Typically these light pulses are emitted in long chains with each "pulse" differing from the previous disturbance by some random phase shift. For an element of such source to appear monochromatic (or quasimonochromatic) two general criteria must be satisfied. The bandwidth must be small compared to the central frequency ($\Delta\nu/\nu_c<<1$), and the longest optical path difference (d) must be small compared to the coherence length ($d<<\Delta l$).[2] The second criterion ensures that light originating from such a source element and (for example) imaged on some plane is comprised only of light from that single pulse and not some successive pulse that has undergone a random phase shift. Since coherence lengths can be of the order of the wavelength of light, this second condition is not always satisfied. Nevertheless, for the purpose of the ensuing discussions we will assume the quasimonochromatic conditions are satisfied, and treat individual source elements as independent monochromatic sources.

Definition of Coherence:

Two sources are said to be coherent if the phase difference between them is constant. In reality, source elements undergo independent random phase shifts causing the phase difference between them to also change randomly. During the few billionths of a second between these phase shifts, the phase difference is constant and interference fringes could theoretically be observed if a sufficiently fast detector were used. (This type of interference has only been observed using separate laser sources with sufficiently long coherence times). For all practical purposes separate elements of a thermal source can be treated as completely incoherent.

If both waves originate from the same source element, they have the same initial phase. Any phase difference at a subsequent plane in the imaging system is simply a result of the different optical paths traversed (again assuming d<<Δl).

Hopkins, in his classic article on partial coherence[3], begins with an equation for the intensity resulting from the addition of two plane waves of the form $A_n e^{i\Psi_n}$, where A is the magnitude, Ψ is the phase, and $\langle\ \rangle$ represents a temporal average.

$$I_p = \langle A_1^2 \rangle + \langle A_2^2 \rangle + 2\langle A_1 A_2 \cos(\Psi_1 - \Psi_2) \rangle \qquad (2)$$

The first two terms represent the intensities of the individual incident waves. The third term represents the interaction between the two waves and is a function of the phase difference between them.

In the incoherent case, the random phase difference $(\Psi_1 - \Psi_2)$ results in an average value of zero for the cosine function. The resultant intensity is then simply the algebraic sum of two incident wave intensities. When the waves originate from the same source element (i.e. they are coherent) the average of the cosine term takes on some constant value between -1 and 1. (A zero value indicates incoherence while positive and negative values represent constructive and destructive interference respectively). This suggests one could define the cosine term as a mutual phase coherence factor (γ_{12}) and rewrite equation (2) as:

$$I_p = A_1^2 + A_2^2 + 2A_1 A_2 \gamma_{12} \qquad (3)$$

Hopkins evaluated this factor based on the general case shown in figure 1.2. Consider two waves emitted by an area element (dσ) of some source (of area Σ) that produce complex amplitudes u1 and u2 at points P1 and P2. These waves then propagate through some arbitrary system (S) resulting in complex amplitudes f1 and f2 at point P.

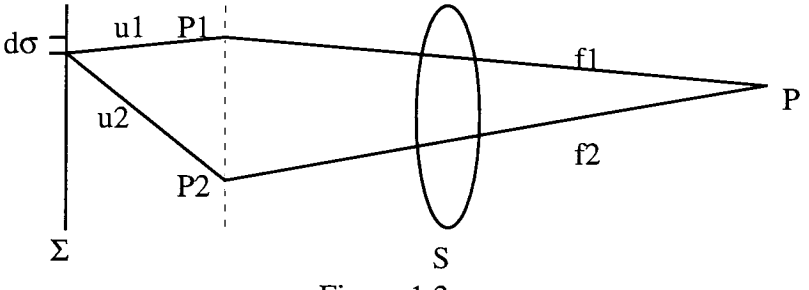

Figure 1.2

The contribution to the complex disturbance E at P due to dσ can then be represented by the sum:

$$dE_p = (u_1 f_1 + u_2 f_2) d\sigma \qquad (4)$$

The intensity as seen by a detector at P is:

$$dI_p = \left\langle (u_1 f_1 + u_2 f_2)(u_1^* f_1^* + u_2^* f_2^*) d\sigma \right\rangle \tag{5}$$

By integrating both sides and using the identity: $z_1 z_2^* + z_1^* z_2 = 2\,\mathrm{Re}\{z_1 z_2^*\}$, the total intensity is obtained.

$$I_p = \left\{ \int_\Sigma |u_1| d\sigma \right\} |f_1|^2 + \left\{ \int_\Sigma |u_2| d\sigma \right\} |f_2|^2 + 2\,\mathrm{Re}\left\{ \int_\Sigma u_1 u_2^* d\sigma\, f_1 f_2^* \right\} \tag{6}$$

Note that f_1 and f_2 have been removed from the integral since they represent properties of the imaging system, not of the source. The first two bracketed quantities are the intensities I_1 and I_2 at points P_1 and P_2 respectively due to contributions from the entire source. The coherence factor γ_{12} is defined as follows:

$$\gamma_{12} = \frac{1}{\sqrt{I_1 I_2}} \int_\Sigma u_1 u_2^* d\sigma \tag{7}$$

and substitution of I_1, I_2, and γ_{12} into equation (6) yields an equation similar in form to equation (3).

$$I_p = I_1 |f_1|^2 + I_2 |f_2|^2 + 2\sqrt{I_1 I_2}\,\mathrm{Re}\{\gamma_{12} f_1 f_2^*\} \tag{8}$$

Equation (7) is an expression which defines the phase coherence factor γ_{12} between two points illuminated on a plane by an extended source (Σ). Hopkin's evaluates the phase coherence factor for the simple case shown in figure 1.3.

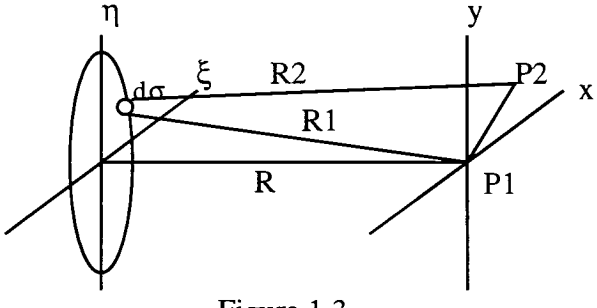

Figure 1.3

The complex magnitudes u_1 and u_2 at points P1 and P2 can be written as

$$u_1 = \frac{\sqrt{I(\xi,\eta)}}{R_1} e^{-ikR_1} \qquad u_2 = \frac{\sqrt{I(\xi,\eta)}}{R_2} e^{-ikR_2} \tag{9}$$

where R_1 and R_2 are the distances from source element $d\sigma$ as shown. By substituting these relationships into equation (7)

$$\gamma_{12}(x,y) = \frac{1}{\sqrt{I_1 I_2}} \int_\Sigma \frac{I(\xi,\eta)}{R_1 R_2} e^{-ik(R_2 - R_1)} d\sigma \tag{10}$$

Taking $d\sigma$ to be located at (ξ,η) and P2 at (x,y) the expression R_1-R_2 can be written in the form:

$$R_2 - R_1 = \frac{\sqrt{x^2+y^2}}{R_2+R_1} - \frac{2}{R_2+R_1}(x\xi + y\eta) \tag{11}$$

For small x and y (compared to the distance R), $R_1 \cong R_2 \cong R$, and $\sqrt{x^2+y^2}/R \cong 0$ so equation (10) can be presented in the more familiar form:

$$\gamma_{12}(x,y) = \frac{1}{R^2\sqrt{I_1 I_2}} \int_{\Sigma} I(\xi,\eta) e^{-i\frac{k}{R}(x\xi+y\eta)} d\xi d\eta \tag{12}$$

where the phase coherence factor γ_{12} for two points on a plane some distance (R) from the source is proportional to the Fourier transform of the source distribution.

This result is an illustration of Fourier's theorem that the disturbance produced by a finite physical source can be expressed as the sum of strictly monochromatic and therefore infinitely long wave trains.[4] The kernel of the transform in equation 12 represents a phase coherence element of unit magnitude and linear phase. Each source point produces such a phase coherence term of unit magnitude that impinges on the object plane. Since all points in the object plane have a phase coherence of unit magnitude, a single source element (as one might expect) behaves as a coherent source (γ_{12} =1). The phase coherence parameter $\gamma_{12}(x,y)$ is simply the sum of the contributions from each source point.

Equation (12) describes only the simple case of the illumination at a plane some distance from an extended source. In actual systems the object plane is typically illuminated by some system of condenser lenses. Once $\gamma_{12}(x,y)$ at the object plane is known, the inverse transform can be taken to represent an 'effective source'[5]. Physically, the effective source corresponds to the intensity distribution in the pupil of the condensing lens system.[6]

Now let us extend the discussion used to derive the phase coherence factor to include the complete imaging system (shown schematically in figure 1.4). Suppose a source element $d\sigma$ produces a complex amplitude u_1 at point (x_1,y_1) in the object plane. If the complex transmission of the object is represented by the function f(x,y), the disturbance due to $d\sigma$ at point (x_1,y_1) in the object plane becomes $u_1 f(x_1,y_1)$. Let $k(x'-x_1',y'-y_1')$ be the complex amplitude produced at point $(x'-x_1',y'-y_1')$ in the image plane due to a disturbance of unit amplitude and zero phase at point (x_1,y_1) in the object plane. The function $k(x'-x_1',y'-y_1')$ represents a complex amplitude distribution around (x_1',y_1') equivalent to the impulse response of the system.

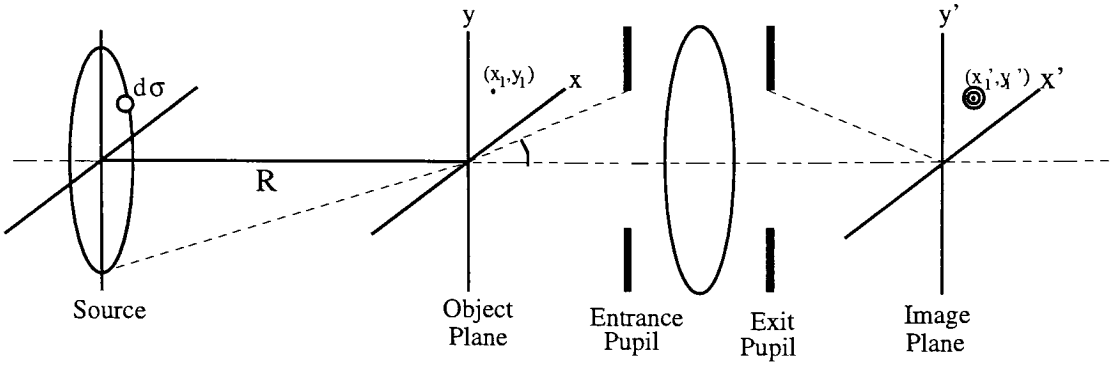

Figure 1.4

The complex amplitude at (x',y') due to a single source element (dσ) interacting with a single object point (x_1,y_1) will be

$$u_1 f(x_1,y_1)k(x'-x_1,y'-y_1). \tag{13}$$

Integration over the entire object plane yields an expression for the total complex amplitude at point (x',y') due to dσ.

$$\iint u_1(x_1,y_1)f(x_1,y_1)k(x'-x_1,y'-y_1)dx_1dy_1 \tag{14}$$

An equivalent expression can be obtained by using an independent point (x_2,y_2). The intensity (using identity $|A|^2 = AA^*$) at point (x',y') due to dσ is then given by

$$dI=\left\{\iint u_1(x_1,y_1)f(x_1,y_1)k(x'-x_1,y'-y_1)dx_1dy_1\iint u_2^*(x_2,y_2)f^*(x_2,y_2)k^*(x'-x_2,y'-y_2)dx_2dy_2\right\}d\sigma \tag{15}$$

Since all factors but u_1 and u_2 are independent of the source, integrating over the entire source yields the expression,

$$I(x',y')=\iiint\left\{\int_\Sigma u_1(x_1,y_1)u_2^*(x_2,y_2)d\sigma\right\}f(x_1,y_1)k(x'-x_1,y'-y_1)f^*(x_2,y_2)k^*(x'-x_2,y'-y_2)dx_1dx_2dy_1dy_2 \tag{16}$$

where the expression in brackets is in the form of equation (7) and represents the phase coherence function of the system. Equation (16) can then be rewritten as

$$I(x',y')=\iiint\gamma_{12}(x_1-x_2,y_1-y_2)f(x_1,y_1)f^*(x_2,y_2)k(x'-x_1,y'-y_1)k^*(x'-x_2,y'-y_2)dx_1dx_2dy_1dy_2 \tag{17}$$

(Spatially) Coherent and Incoherent Cases:

Equation (17) can be simplified considerably in the case of completely coherent and completely incoherent illumination. First, consider the case of coherent illumination where the effective source (or condenser aperture) is a point on the optic axis. The phase coherence function $\gamma_{12}(x,y)$ is defined by the Fourier transform of the source (equation 12). In the case of a point source $\gamma_{12}=1$ for all x and y. Equation (17) can then be written

$$I(x',y') = \iint\iint f(x_1,y_1)f^*(x_2,y_2)k(x'-x_1,y'-y_1)k^*(x'-x_2,y'-y_2)dx_1dx_2dy_1dy_2 \qquad (18)$$

For clarity we will consider only a function of one dimension in the remainder of this discussion. (The reasoning is easily expanded to 2-D). Note that the x_1 and x_2 terms can be separated in equation (18) to yield

$$I(x') = \int f(x_1)k(x'-x_1)dx_1 \int f^*(x_2)k^*(x'-x_2)dx_2 \qquad (19)$$

The integrals in equation (19) are convolutions of f(x) and k(x) that can be written in the form,

$$I(x') = \left[f(x')*k(x')\right]\left[f^*(x')*k^*(x')\right] \qquad (20)$$

or more simply,

$$I(x') = \left|f(x')\right|^2 = \left|f(x')*k(x')\right|^2 . \qquad (21)$$

As expected, the transfer function of a coherent system is a scaled replica of the pupil function (denoted by the function k(x)) of the objective. Note also that coherent illumination is linear in complex amplitude.

In the case of purely spatially incoherent illumination, the effective source is an infinite plane of unit magnitude. The Fourier transform of a plane is simply a delta function, so equation (17) (in one dimension) becomes,

$$I(x',y') = \iint \delta(x_1-x_2)f(x_1)f^*(x_2)k(x'-x_1)k^*(x'-x_2)dx_1dx_2 . \qquad (22)$$

By the sifting theorem equation (22) simplifies to the form,

$$I(x',y') = \iint f(x_2)f^*(x_2)k(x'-x_2)k^*(x'-x_2)dx_1dx_2 = \iint \left|f(x_2)\right|^2 \left|k(x'-x_2)\right|^2 dx_1dx_2 \qquad (23)$$

Again the equation is in the form of a convolution integral representing the expression:

$$I(x') = \left|f(x')\right|^2 * \left|k(x')\right|^2 = I(x')*\left|k(x')\right|^2 \qquad (24)$$

Incoherent imaging is linear in intensity with an impulse response equivalent to the squared magnitude of the coherent impulse response. The incoherent transfer function is the Fourier transform of the incoherent impulse response:

$$\Im\left\{\left|k(x')\right|^2\right\} = K(\xi) \star K(\xi) \qquad (25)$$

Let us consider a one-dimensional case where the pupil function of the objective is a Rectangle (an ideal lowpass filter). In the coherent case, spatial frequencies below some cut-off will be passed unaltered, while frequencies larger than this value will be totally blocked by the system. (We will assume this cut-off to be at λ/2NA. A coarse derivation

of this parameter will be presented in the section on off-axis illumination). The coherent transfer function is simply a scaled replica of the pupil function (a scaled RECT) in frequency space as shown in figure 1.5. The incoherent transfer function is the autocorrelation of the RECT which is a TRI (triangle) function.

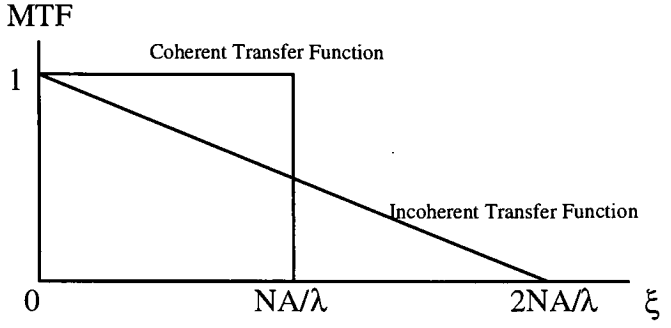

Figure 1.5

An equivalent line of reasoning may be derived for the space domain. In the example above, the coherent impulse response would be a SINC. Taking the squared magnitude of this SINC yields the incoherent impulse response (a $SINC^2$ function). As expected, the Fourier transform of the $SINC^2$ produces a TRI function equivalent to the incoherent transfer function in figure 1.5.

It should be noted that since coherently illuminated systems are linear in complex amplitude, and incoherent systems in intensity, the comparison of transfer functions in figure 1.5 is somewhat ambiguous. For the purpose of this discussion the coherent transfer function can be taken to represent modulation in intensity rather than complex amplitude. (We will see later that these representations are equivalent in the case of three-beam interference). Further difficulties arise when one tries to fit partially coherent illumination into this picture. Imaging with partially coherent illumination is a non-linear operation that does not have a general transfer function. Nevertheless, a modulation transfer function (MTF) can be calculated for specific inputs (a series of gratings for example) and compared to the coherent and incoherent cases. A typical curve is shown below.

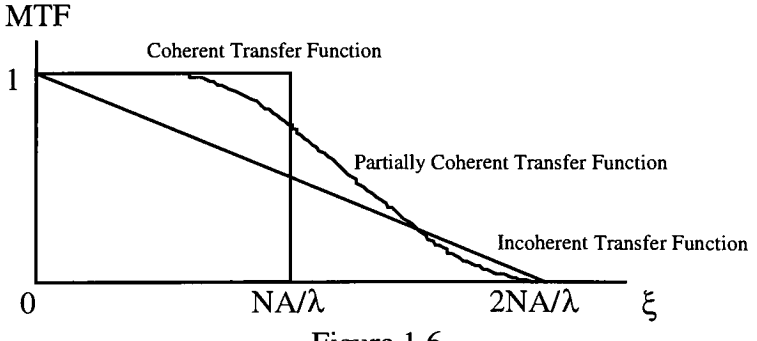

Figure 1.6

Partially coherent illumination has the potential to provide better modulation than incoherent illumination beyond the coherent resolution limit.

Calculation of Partially Coherent Images:

The following is a summary of the procedure outlined by Kintner[7] for the calculation of two-dimensional image intensity distributions using aberration-free systems with partially coherent illumination. Kintner's approach restricts Hopkins' theory to unaberrated systems and one-dimensional binary transmission gratings to enable rapid calculation (on a 1980 vintage VAX computer). This basic model was used as the basis for the C program described in chapter 3.

The algorithm uses object-plane coordinates (x',y') which are converted to dimensionless Cartesian coordinates x and y,

$$x = x' \frac{NA_o}{\lambda} \tag{26}$$

$$y = y' \frac{NA_o}{\lambda} \tag{27}$$

NA_O is the numerical aperture of the objective, λ is the mean wavelength of the quasimonochromatic source, and (x,y) are geometrical coordinates in the object plane. Division by the wavelength eliminates the geometric units, while multiplying by the numerical aperture of the condenser is essentially a normalization in the frequency (pupil) plane that defines a pupil of unit magnitude.

Hopkins' formula (equation 17) can be written in the frequency plane in the form;

$$I(\xi,\eta) = \int_{-\infty}^{+\infty}\int T(\xi+\xi',\eta+\eta';\xi',\eta')F(\xi+\xi',\eta+\eta')F^*(\xi',\eta')d\xi' d\eta'. \tag{28}$$

$F(\xi,\eta)$ is the Fourier transform of the object function f(x,y) and $T(\xi,\eta,\xi',\eta')$ is the transmission cross coefficient (TCC) defined by the equation:

$$T(\xi_1,\eta_1;\xi_2,\eta_2) = \int_{-\infty}^{+\infty}\int J(\xi'',\eta'')K(\xi_1+\xi'',\eta_1+\eta'')K^*(\xi_2+\xi'',\eta_2+\eta'')d\xi'' d\eta'' \tag{29}$$

where $J(\xi,\eta)$ is the Fourier transform of the mutual coherence function j(x,y) and $K(\xi,\eta)$ is the pupil function of the objective lens system. The TCC describes the imaging properties of system including contributions from both the source (condenser) and objective. In the case of Kohler illumination, the aperture of the condenser is imaged onto the entrance pupil of the objective. In this arrangement the pupil function of the condenser is equivalent to the 'effective source' illuminating the image plane as described by Hopkins. Furthermore, since the mutual coherence function j(x,y) has been shown to equal the transform of the effective source for small angles, the quantity $J(\xi,\eta)$ is equivalent to the intensity distribution in the pupil of the condenser.

In the case of circular apertures, the functions $J(\xi,\eta)$ and $K(\xi-\xi_1,\eta-\eta_1)$ and $K^*(\xi-\xi_2,\eta-\eta_2)$ are non-zero only within circles of a given radius centered around (0,0), (ξ_1,η_1), and (ξ_2,η_2) respectively. We may now consider the bounds of the integral in equation (29) to be defined by the area of intersection of three circles in the pupil plane of the objective (Figure 1.7). The radius defining the limits of the pupil function $K(\xi,\eta)$ is the numerical aperture of the condenser NA_O normalized to unit magnitude in the coordinate system defined by equations (26) and (27).

Similarly, the radius of the objective pupil function $J(\xi,\eta)$ is the numerical aperture of the condenser normalized by the objective NA. This leads to the definition of a parameter σ which is sometimes termed the 'partial coherence parameter' of the optical system.

$$\sigma = \frac{NA_c}{NA_o} \tag{30}$$

For circular apertures, small angles, and uniform illumination, this single parameter is sufficient to describe the illumination conditions. If the source intensity distribution is non-uniform, it is convenient to assume uniform illumination and to suppose that the incident light passes through some screen of suitable non-uniform intensity that covers the object.[8]

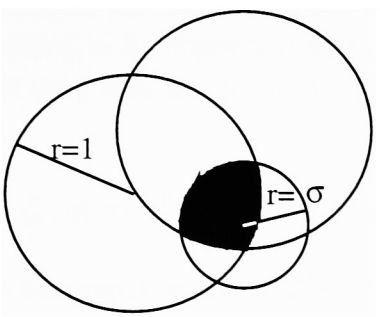

Figure 1.7

Illustration of the overlap region of the two objective pupil functions (circles of unit radii) $K(\xi,\eta)$ and $K^*(\xi,\eta)$ centered at points (ξ_1,η_1) and (ξ_2,η_2) in the frequency plane and the condenser pupil function $J(\xi,\eta)$.

In an unaberrated system under uniform illumination the functions J, K, and K^* all define circular regions of unit magnitude. In this case the TCC integral in equation (29) is the geometric area of intersection of the three circles. The TCC is evaluated for each pair of spatial frequencies (ξ_1,η_1) and (ξ_2,η_2) in the pupil plane. The result is a value between 0 and π that scales their contribution to the object spectrum. (Note that the area of overlap in figure 1.7 can not exceed π). Although the algorithm to determine the geometric overlap involves a fairly strenuous exercise in logic, the calculation is quick and straightforward[9].

In an aberrated system, the pupil functions $K(\xi,\eta)$ and $K^*(\xi,\eta)$ are no longer smooth surfaces of unit magnitude. Aberrations modeled as phase components in the pupil function result in complex valued TCCs. It may not be possible to analytically solve for the intersected volume of the surfaces enclosed by the union of the pupil functions when arbitrary aberrations are introduced. A reasonably efficient method of evaluating the TCC in the case of defocus was explored by Subramanian[10] using numerical integration techniques, and later extended to all circularly symmetric aberrations. The SPLAT (Simulation of Projection Lens Aberrations via TCC's) program, developed at U.C. Berkeley, uses an adaptive gaussian quadrature routine to evaluate the TCC[11]. Although this approach is time consuming, it permits the use of any arbitrary pupil function.

The 1DSIM program (described in detail in chapter 3) restricts pupil function aberrations to cases of defocus. This limitation is quite reasonable for applications in semiconductor lithography since defocus is the major source of image degradation in what are essentially diffraction-limited optical systems. The quadratic phase terms representing a defocused system

are also extremely will behaved in the TCC integral and enable rapid calculation. A defocused optical system can be represented in the pupil function by a quadratic phase of the form[10]

$$K(\xi,\eta)=e^{iC_1(\xi^2+\eta^2)} \quad \text{and} \quad K^*(\xi,\eta)=e^{-iC_1(\xi^2+\eta^2)} \tag{31}$$

where C_1 is a constant defined by the equation:

$$C_1=d\frac{NA_o^2}{2\lambda} \tag{32}$$

and d is the distance from the image plane to the plane of perfect focus. In the case of 1-D patterns periodic in the x direction, the functions K and K* are shifted along the ξ axis during the TCC calculation by some value ξ_1 or ξ_2. (Note that with these restrictions, the functions J, K, and K* are always centered about the y axis, i.e. η_1 and $\eta_2 = 0$). A more general form of equation (31) can be written :

$$K(\xi-\xi_1,\eta)=e^{iC_1[(\xi-\xi_1)^2+\eta^2]} \quad \text{and} \quad K^*(\xi,\eta)=e^{-iC_1(\xi^2+\eta^2)} \tag{33}$$

In the region where $J(\xi,\eta)$ is non-zero (i.e. where $\xi^2 + \eta^2 \le \sigma$) equation (29) can be written as:

$$TCC(\xi_1,\xi_2)=\iint e^{iC_1[(\xi-\xi_1)^2+\eta^2]}e^{-iC_1[(\xi-\xi_2)^2+\eta^2]}d\xi d\eta=\iint e^{iC_1[\xi_1^2-\xi_2^2+2\xi(\xi_2-\xi_1)]}d\xi d\eta \tag{34}$$

Removing a constant factor of ξ_1 and ξ_2 and making the substitution $u=2iC_1(\xi_2-\xi_1)\xi$ yields:

$$TCC(\xi_1,\xi_2)=\frac{e^{iC_1(\xi_1^2-\xi_2^2)}}{2iC_1(\xi_2-\xi_1)}\iint e^u du d\eta \tag{35}$$

The integral of e^u is simply e^u. At this point it is necessary to determine the region of overlap to find the limits of integration for ξ and η. Consider the simple case as shown in figure 1.8, where the condenser aperture defines the region of overlap.

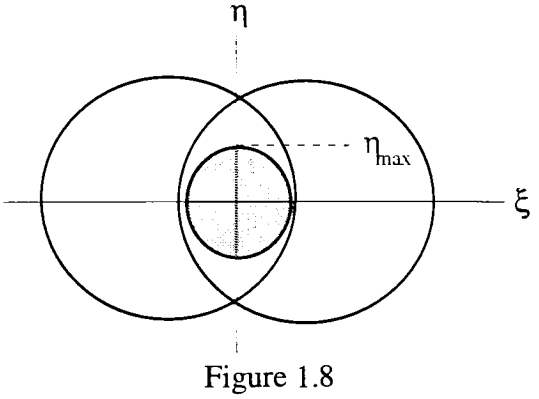

Figure 1.8

The bounds of ξ are defined by the circle $\xi^2 + \eta^2 = \sigma^2$ or $\xi = \sqrt{\sigma^2 - \eta^2}$. Substituting $C_3 = 2iC_1(\xi_2 - \xi_1)$ and u = $C_3\xi$ yields the equation:

$$TCC(\xi_1, \xi_2) = \frac{e^{iC_1(\xi_1^2 - \xi_2^2)}}{2iC_1(\xi_2 - \xi_1)} \int e^{2iC_1(\xi_2 - \xi_1)\sqrt{\sigma^2 - \eta^2}} - e^{-2iC_1(\xi_2 - \xi_1)\sqrt{\sigma^2 - \eta^2}} d\eta \qquad (36)$$

The limits of η in this example range from 0 to η_{max} (where $\eta_{max} = \sigma$ in this example). Note that since the TCC is symmetrical about the ξ axis in the 1-D defocus-only case, the integral can be evaluated from 0 to η_{max} and simply doubled to include the lower area of overlap. Since the integral in equation (36) does not have an analytical solution, a numerical integration is performed along the h axis. The integrand is evaluated at uniform intervals from 0 to η_{max}, and multiplied by the interval width $\Delta\eta$. The resulting equation is the finite sum:

$$TCC(\xi_1, \xi_2) = \frac{2e^{iC_1(\xi_1^2 - \xi_2^2)}}{C_3} \sum_{\eta=0}^{\eta=\eta_{max}} \Delta\eta e^{C_3\sqrt{\sigma^2 - \eta^2}} - e^{-C_3\sqrt{\sigma^2 - \eta^2}} \qquad (37)$$

The accuracy of equation 37 is a function of the number of samples along the η axis. One hundred slices are sufficient for typical values of defocus. Since the frequency of the oscillations in the pupil function increase as the level of defocus increases, a greater sampling rate may be necessary for unusually large values of defocus.

Having established the theoretical basis for the evaluation of the image intensity distribution produced by a partially coherent imaging system, we will now discuss the practical considerations required for computation. First, computation involving continuous functions must naturally involve a finite number of points. The TCC's will be evaluated for a finite array of points (frequencies) in the pupil with separations $\Delta\xi$ and $\Delta\eta$. Sampling in the frequency domain naturally implies a periodic pattern in the space domain (the transform of COMB($\xi/\Delta\xi$) is proportional to COMB($x\Delta\xi$)) where the period in x and y are defined as:

$$P_x = \frac{1}{\Delta\xi} \qquad P_y = \frac{1}{\Delta\eta} \qquad (31)$$

Typically an object distribution F(x,y) is designed with a specific period and values for $\Delta\xi$ and $\Delta\eta$ calculated. Non-periodic features are approximated by simply increasing the period (the distance until the next instance of the pattern). This approach (sometimes referred to as "zero padding") increases the sampling frequency and more closely approximates the continuous spectrum of a non-periodic object.

It also will be necessary to define limits to this array of points in frequency space; ξ_{max}, ξ_{min}, η_{max}, and η_{min}. These limits define the region where the TCC is non-zero, that is, where there is finite overlap of the circles in figure 1.8. If $\xi_1 \geq \xi_2$ and $\eta_1 \geq \eta_2$ then the limits are defined as follows:

$$\begin{aligned} \xi_{max} &= \xi_1 + 1 & \eta_{max} &= \eta_1 + 1 \\ \xi_{min} &= \xi_2 - 1 & \eta_{min} &= \eta_2 - 1 \end{aligned} \qquad (32)$$

(Note if $\xi_1 \le \xi_2$ or $\eta_1 \le \eta_2$ the η_1 and η_2 or ξ_1 and ξ_2 would be exchanged). These equations simply limit the summation to the values where the distance between the centers of the two pupil functions (having unit radii) is less than two (i.e. where they overlap).

The TCC can then be evaluated over these limits,

$$T(\xi_1, \eta_1; \xi_2, \eta_2) = \int_{\eta_{min}}^{\eta_{max}} \int_{\xi_{min}}^{\xi_{max}} J(\xi'', \eta'') K(\xi_1 + \xi'', \eta_1 + \eta'') K^*(\xi_2 + \xi'', \eta_2 + \eta'') d\xi'' d\eta''. \qquad (33)$$

Note that even though there are only a discrete number of points over which the TCC must be evaluated, the functions J and K are still continuous and the integral in equation (33) must be evaluated analytically (or numerically if aberrations are present). Equation (28) can be evaluated as a finite summation once the TCC's are known.

$$I(\xi, \eta) = \sum\sum T(\xi + \xi', \eta + \eta'; \xi', \eta') F(\xi + \xi', \eta + \eta') F^*(\xi', \eta') \qquad (34)$$

The program described in chapter 3 is an implementation of the algorithms described by Kintner and Subramanian with extensions that include the ability to define and simulate arbitrary complex objects using both standard and annular illumination.

CHAPTER 2:
Review of Phase Shifting Masks and Binary Optics:

Introduction to Phase Shifting

It has been known for centuries that waves impinging on an aperture produce disturbances beyond the geometric shadow of the obstruction. These diffraction effects manifest themselves differently depending upon the coherence of the optical system. If the illumination is incoherent, the light traveling through adjacent apertures can be treated independently. The resulting intensity distribution is simply the sum of the intensities produced by the individual apertures. In the case of coherent or partially coherent illumination, light diffracted by adjacent apertures will interfere to some degree. In the case of a standard transmission mask, diffracted light will often interfere constructively causing significant light intensity in the supposedly "dark" regions shadowed by the mask. This added intensity degrades both the modulation (a ratio relating the maximum and minimum intensities) and the aerial image log-slope (a measure of image contrast).

$$mtf = \frac{I_{\max} - I_{\min}}{I_{\max} + I_{\min}} \quad (1) \qquad \log\text{-}slope = \frac{\log(\Delta I)}{\Delta x} \quad (2)$$

It has been shown[1] that by arranging the apertures so that waves transmitted through adjacent apertures are 180 degrees out of phase with one another, destructive interference will occur between the apertures. In this case the interference or "ringing" is used to dampen the energy between the apertures and amplify the peak intensity.

A phase difference (or phase shift) can be induced between two light waves by altering the optical path distance (OPD) each must traverse. The wave that has traveled a longer (optical) distance will 'lag' in phase light that has traversed a shorter distance. The OPD equation is simply,

$$OPD = nd \quad (3)$$

where n is the refractive index, and d is the physical distance traveled. Phase-shifting masks accomplish this optical path difference by passing one wave through a material of higher refractive index than the other. (See figure 2.1)

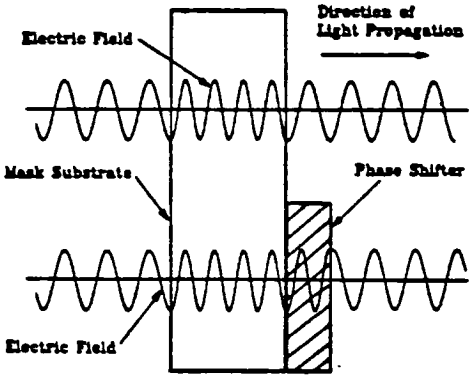

Figure 2.1

The difference in the optical path between two waves traveling a distance d through materials with different refractive indices is given by equation (4).

$$\Delta OP = n_2 d - n_1 d = d(n_2 - n_1) \tag{4}$$

Multiplying by $2\pi/\lambda$ converts optical path difference to phase difference ($\Delta\phi$). The resulting equation gives the distance (d) necessary for light (of wavelength λ) traveling through two materials with refractive indices (n_1 and n_2) to emerge with a specified phase difference ($\Delta\phi$).

$$d = \frac{\lambda(\Delta\phi)}{2\pi(n_2 - n_1)} \tag{5}$$

In the case where a 180-degree (or π radians) phase shift is desired and the second material is air ($n_2 = 1$), equation (4) reduces to:

$$d = \frac{\lambda}{2(n - 1)} \tag{6}$$

The following table gives typical thickness (d) values for common materials and wavelengths. Note the refractive index of fused silica changes significantly as function of wavelength over the wavelengths of interest.

Material	Refractive Index	Wavelength (um)	Thickness (um)
PMMA	1.62	.436	.3516
Fused Silica (quartz)	1.46	.436	.4739
Fused Silica (quartz)	1.476	.365	.3834
Fused Silica (quartz)	1.508	.248	.2440
Fused Silica (quartz)	1.561	.193	.1720

Table 2.1

Alternating (Levenson) Phase Shift Masks:

Though knowledge of improved resolution using adjacent apertures that are 180 degrees out of phase has been utilized in the fields of astronomy and radio communications for decades, it was not applied to semiconductor lithography until Levenson's work in 1982[2]. Levenson first constructed a standard binary transmission mask using patterned chrome on glass as the attenuating medium. A layer of PMMA (polymethylmethacrylate) was then coated and patterned such that material was present only over selected apertures. The PMMA thickness was such that the phase of the light passing through the material was retarded by 180 degrees relative to light transmitted through an adjacent (uncoated) region.

The performance improvement of this type of mask over conventional techniques is due to the bipolar nature of the electric field at the mask. (See Figure 2.2). While the normalized electric field due to the conventional mask alternates between 1 and 0 within

a single line/space pair, the phase mask oscillates between 1 and -1 in twice the period. This effectively halves the spatial bandwidth necessary to image the grating.

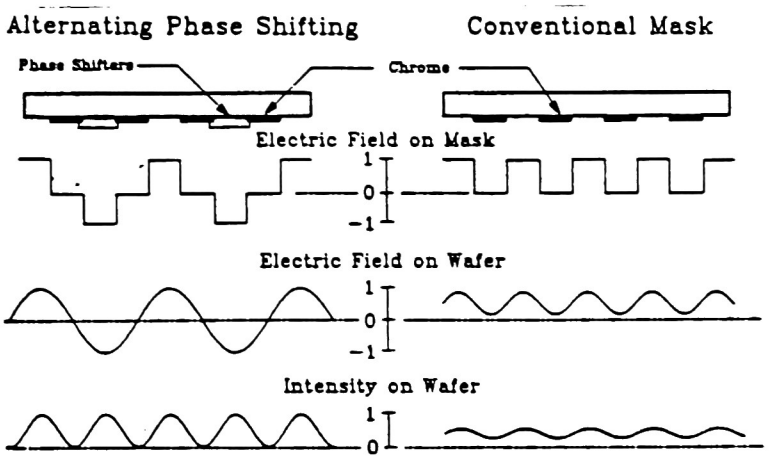

Figure 2.2

Although Levenson reported a 40-percent increase in usable resolution with minimal reduction in depth of focus for some structure tested, it was observed that an ideal solution could not be obtained in the case of an arbitrary pattern. Consider the layouts in Figure 2.3(a) and 2.3(b) where the distances between adjacent apertures are below the resolution limit without the use of phase shifting. In figure 2.3(a) the alternating 180 - 0 pattern is preserved across the top of the design, but not between apertures A and B, and C and D. Since no resolution enhancement is present in these areas the horizontal lines between A and B, and C and D will not be resolved while the vertical lines print correctly. Similarly, if the phase shifters are adjusted so that the aperture pairs A-B and C-D are 180 degrees out of phase as in Figure 2.3(b), the alternating phase nature is disrupted for the vertical lines at the bottom of the layout.

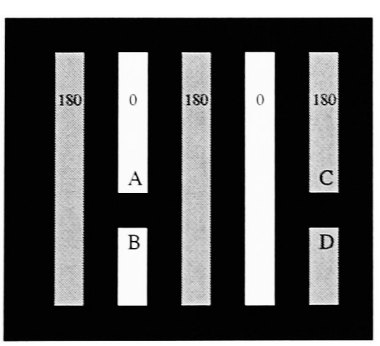

Figure 2.3(a)

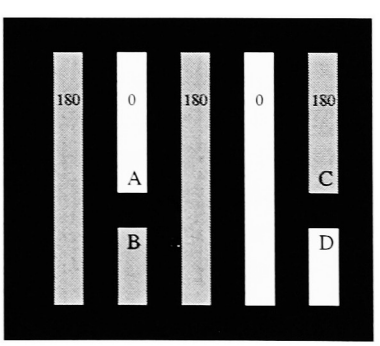

Figure 2.3(b)

Illustration of the difficulties encountered maintaining alternating 0 and 180-degree apertures for arbitrary patterns. Vertical and horizontal alternating phases are preserved in 3a and 3b respectively, but can not be achieved in a single layout.

These examples illustrate the tradeoffs involved in the design of alternating phase shifting masks. The lines that will or will not be enhanced by the phase shifters must be chosen such that deviations from the alternating patterns occur in non-critical areas.

A significant aspect of Levenson's mask design not discussed in this initial work involved the use of only negative tone features. Consider the illustration in Figure 2.4.

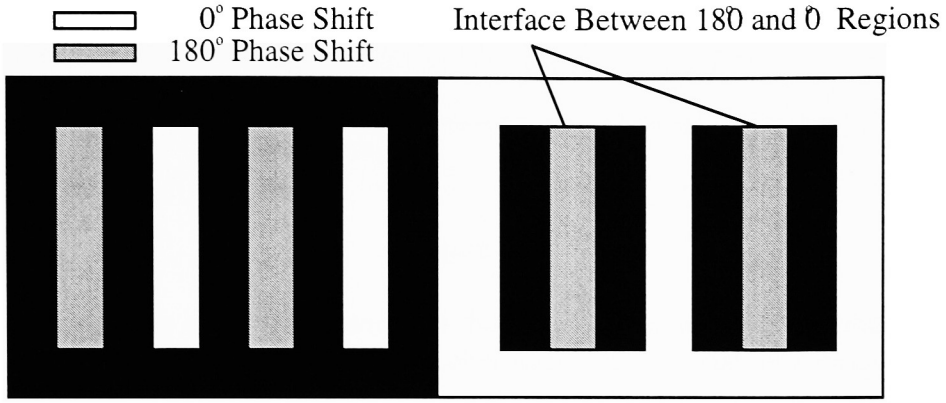

Figure 2.4

In the case of the negative-tone (dark-field) mask, the 180° and 0° regions are bounded by an opaque material, (usually chromium). The 180° and 0° apertures in the positive-tone (light-field) mask are bounded by the unphase-shifted (0°) field. This results in an abrupt transition between 0° and 180° regions as shown in figure 2.4. Neureuther[15] observed that since light waves originating at opposite sides of the boundary are 180 degrees out of phase, a region of strong destructive interference will be present at the interface. This effect manifests itself as extremely fine dark line along the phase boundary. In the case of the positive tone mask in figure 2.4, this line would cause a bridge (a short circuit) to form between the lines.

Chromeless (Non-Attenuated) Phase Shift Masks:

Consider the simple case of a glass (quartz) plate with a thickness variation such that a 180° phase difference is achieved. (Figure 2.5). Since no attenuating material is present one would expect the magnitude of the electric field at the mask to be constant (normalized to unity) as the phase shift serves only to change the polarity of the electric field. This polarity change causes a discontinuity at the phase boundary that forces the electric field through zero. The image plane intensity, which is proportional to the square of the electric field, is also forced through zero at the phase shifter edge. The resulting intensity profile is analogous to the impulse response of the system, the width of which is determined by the wavelength and numerical aperture of the optical system.

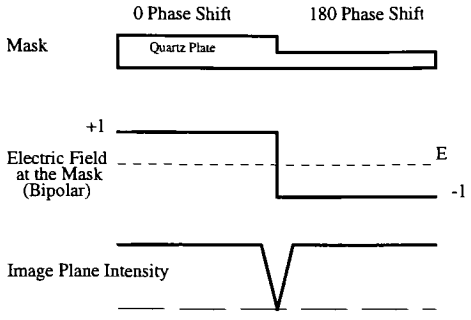

Figure 2.5

The following table contains the width of the aerial image intensity distribution at an intensity of 0.3, (which corresponds reasonably well with the final photoresist image).

Wavelength	Numerical Aperture	Sigma	Linewidth (μm)
436	.29	.68	.69
436	.48	.5	.5
365	.3	.5	.4
365	.48	.5	.25
248	.3	.5	.25
248	.6	.5	.15

Table 2.2

Although the presence of abrupt 180-to-0 phase transitions has been shown to cause problems in the application of alternating-phase masks, the extremely small linewidths that can be achieved are clearly valuable in their own right. Potential applications were explored by Toh[12] in a paper describing the "Chromeless Phase-Shifted Mask". As the name implies, the mask functions without the presence of an attenuating medium (typically chrome for semiconductor applications). Opaque areas on the mask are formed using multiple 180/0 transitions. If the width of the phase shifted regions is large, as in figure 2.6(a), an array of "chromeless" lines are formed. As the period of the phase grating is increased, the dark lines will overlap resulting in a dark region in the image plane. (Figure 2.6(b)).

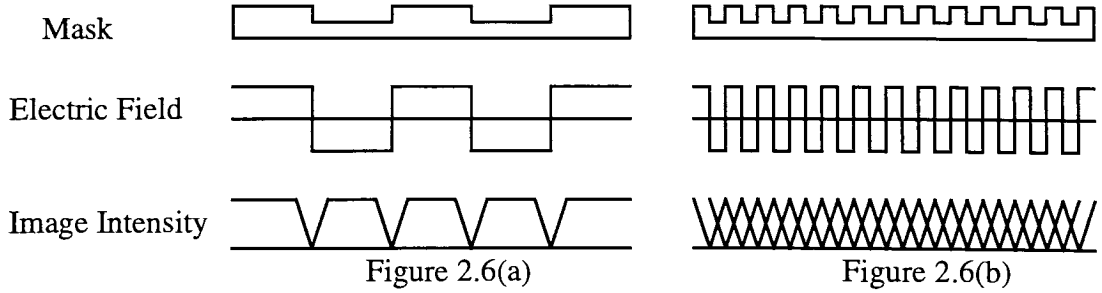

Figure 2.6(a)

Figure 2.6(b)

In this way an arbitrary pattern can be created by controlling the location and period of the 180/0 phase transitions.

Toh reported that phase-shifter widths of $0.3\lambda/NA$ or less produced this dark field effect. Since the average value of the electric field is zero, no 0^{th}-order (DC) diffracted wave exists. If the 1^{st}-order harmonic is a frequency that is not captured by the lens, (i.e. the mask pattern has a spatial frequency that exceeds the spatial bandwidth of the system), none of the orders will be imaged by the lens, thus resulting in a dark field. Extreme off-axis illumination can shift the orders such that a significant intensity is produced in these regions in the image plane even if Toh's design criteria are satisfied. A sigma value of 1.0 produces a background intensity that is 6 percent of that due to a clear field mask. The intensity is essentially zero for $\sigma < 0.8$.

There are several drawbacks to the chromeless mask approach. The fact that large opaque areas must be created using millions of tiny phase pixels dramatically increases the amount of time and data capacity it takes to build the mask using direct write electron beam lithography. A more fundamental problem is associated with the fact that the image will form at the phase shifter edge. In a conventional transmission mask changes in the chrome width simply cause corresponding changes in the imaged linewidths. Dimensional variations of the phase shifters in a chromeless mask will cause errors in the *position* of the resulting lines. This behavior must be considered in the mask design and fabrication processes.

Another difficulty in the practical application of chromeless PSMs involves the same unwanted transition problem described for alternating-type approaches. In even the most simple chromeless patterns 180/0 phase transitions occur in areas where no lines are desired. Consider an array of minimum geometry (chromeless) lines. (Figure 2.7)

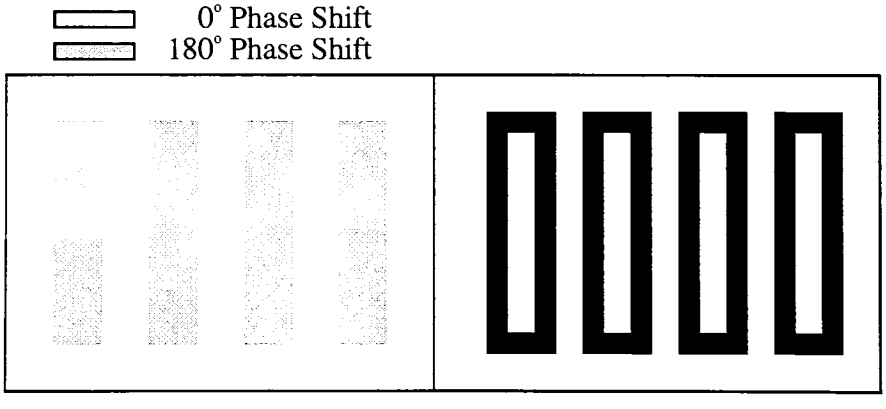

"Chromeless" Mask Pattern Actual Positive Resist Image

Figure 2.7

Rather than printing an array of individual parallel lines, the resulting image is a series of closed loops corresponding to the phase shifter edges on the mask. Single chromeless lines are not achievable with this type of binary phase (180 or 0) mask.

Attenuating Phase Shift Masks:

Design difficulties involved with the use of alternating-type phase shifting on actual integrated circuit layouts have thus far restricted its use to research and development

settings. These challenges are mainly associated with the problems of aperture placement and unwanted chromeless lines previously discussed. Attempts to overcome these problems have involved considerable modification to the mask design, and can require extensive aerial image simulations over an entire mask. The attenuating phase-shift mask was proposed[17] as a compromise between the performance of an alternating PSM and the ease of design and fabrication of conventional mask technologies.

Unlike the Levenson-type mask where a π-phase shift is introduced between adjacent apertures, an attenuating phase mask utilizes a π-phase shift between a partially absorbing attenuating material and adjacent apertures. The small percentage of light (typically 6 to 8 percent) transmitted through the attenuating material destructively interferes with the light from an adjacent aperture. Figure 2.8 illustrates the difference between alternating and attenuated PSMs. (Note that the transmission of the semi-transparent regions has been exaggerated for clarity).

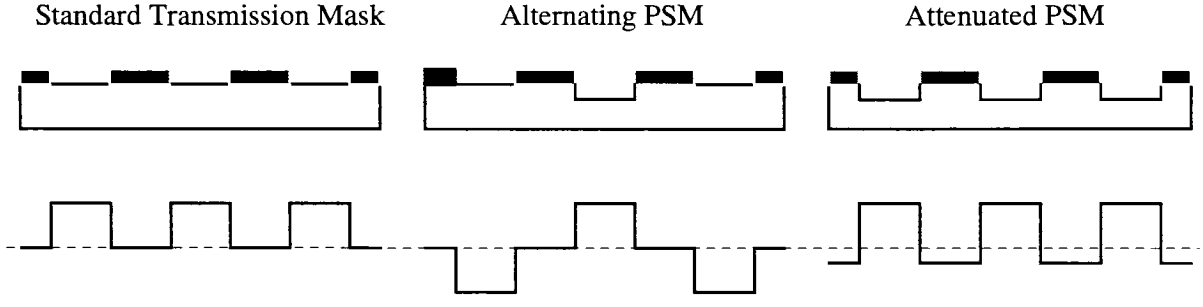

Figure 2.8

The primary frequency in the modulation of the electric field for the alternating PSM is half that of the standard and attenuated PSM masks. Although the electric field of the attenuated mask oscillates at the same frequency as the standard transmission mask, the field passes though zero thus forcing the intensity to zero at the edge of the apertures. This results in destructive interference at the attenuator edge that reduces the intensity of the diffracted light and increases image contrast. Since all 180/0 transitions occur at the attenuator edge, unwanted "chromeless" line formation does not occur. Furthermore, the design layout for the attenuated PSM is identical to that of the standard mask. The only difference is that a phase shifting material must be added to either the apertures or the attenuators.

Rim and Outrigger Phase Shifting Masks:

All phase mask approaches discussed so far have focused on dense and/or periodic mask structures. Isolated lines and spaces are also a part of nearly all integrated circuit designs. Consider first the case of an isolated space, i.e. a dark-field mask with a single slit. Since there is only a single aperture, the alternating approach cannot be directly applied (there are no adjacent apertures to phase shift). A solution first proposed by Hirai[16] was simply to add sub-resolution phase shifted apertures (termed "outriggers") on

either side of the isolated space. The light transmitted through the phase shifted apertures destructively interferes with diffracted light from the main aperture, thus increasing the image contrast. The outrigger width and position must be optimized to provide adequate intensity for significant destructive interference to occur, while ensuring outrigger intensity is such that the outriggers themselves are not printed.

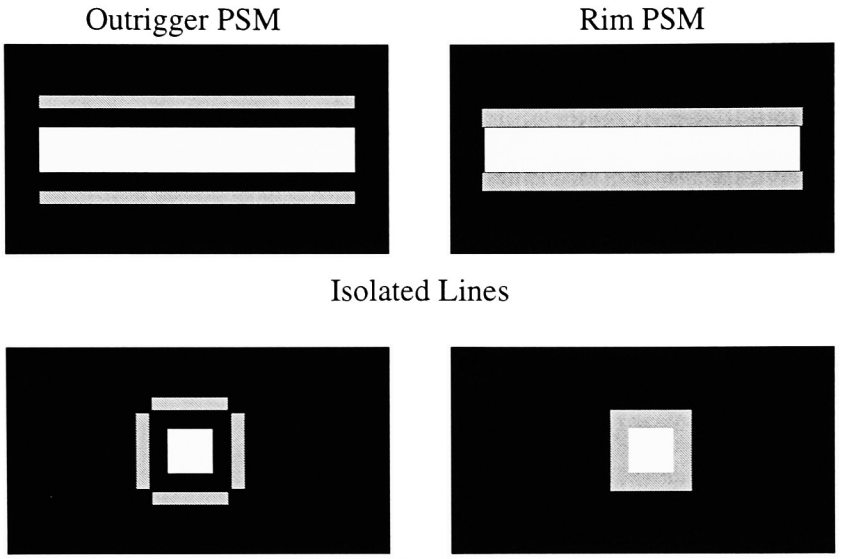

Figure 2.9

The second approach for resolution enhancement of isolated features illustrated in figure 2.9 has been termed "rim" phase shifting. A 180-degree phase shifted region is added at the edge of the apertures to induce destructive interference at the feature boundary. The effect is to define the edge of the image using an extremely high contrast (since the E-field is again forced to zero) chromeless line.

Multi-Stage Phase Shifting Masks:

It has been shown that a 180-degree phase shift in a clear area of the mask will cause a printable artifact in the image. This limits the usefulness of the chromeless and alternating PSM approaches previously discussed. A solution first proposed by Miyazaki[16] involved the incorporation of a 90-degree phase shift level that acted as a buffer between the 180 and 0 phase regions. The abrupt 180/0 phase interface is transformed into a two 90-degree (180/90 and 90/0) transitions. Still, the intensity drop at the 90-degree phase steps can be on the order of 40 percent. Under non-ideal exposure condition (i.e. in cases with defocus) these transitions may print. (Figure 2.10).

A two-stage transition (180/120/60/0) explored by Nistler[17], was shown to provide acceptable intensity losses while enabling a more fault tolerance mask fabrication process. Intensity losses at the phase interfaces were less than 15 percent. (Figure 2.10).

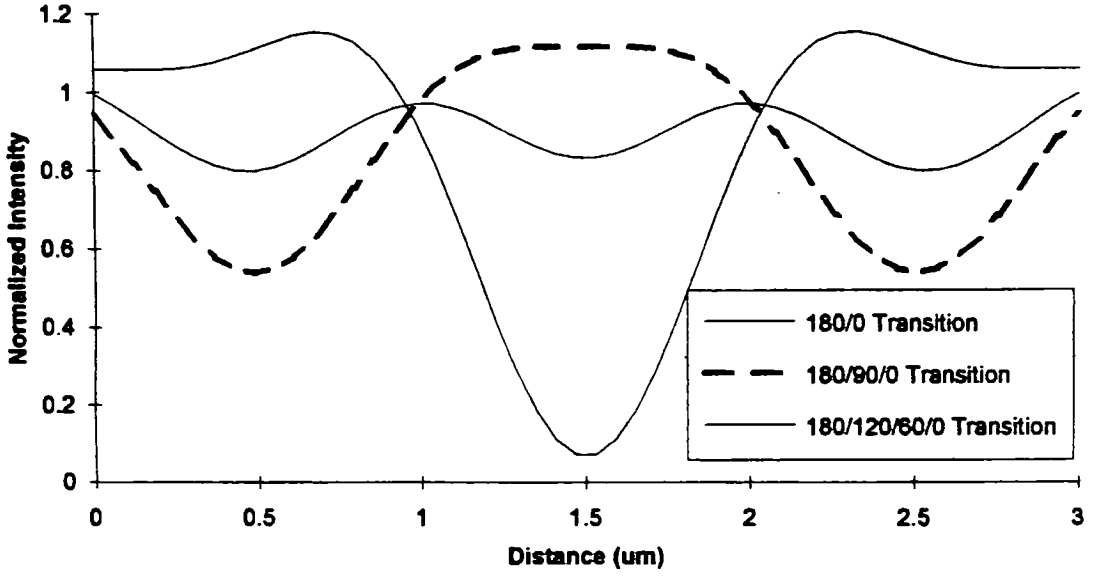

Figure 2.10

Binary Optics and Microlenses

Introduction

The term "binary optics" refers to a method of fabricating stepwise approximations of curved optical surfaces by etching into a planar substrate. Applications exist over the entire light spectrum: from x-ray zone plates and ultraviolet refractive lens aberration correctors, to visible lenses.[14] The ability to produce multiple phase levels or "steps" in a quartz substrate is essential to the fabrication of the complex phase shifting masks and microlens arrays investigated in this work. The fabrication process is based on a series of etches, that double in depth from one level to the next. Different combinations can be used to produce a range from zero (no etch) to the total of all etches. Consider the following diagram of a three etch binary optics process that produces a phase gradient.

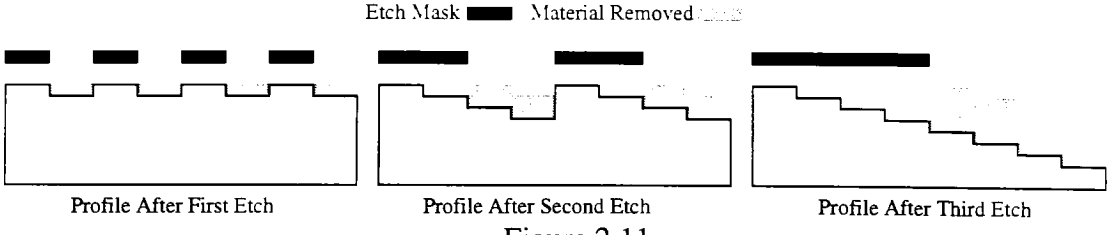

Figure 2.11

Three etch steps produces 2^3 possible step levels. Unfortunately this type of process is extremely sensitive to alignment. Consider a case identical to figure 2.11 in which the mask for the second etch has a been shifted slightly to the right (Figure 2.12).

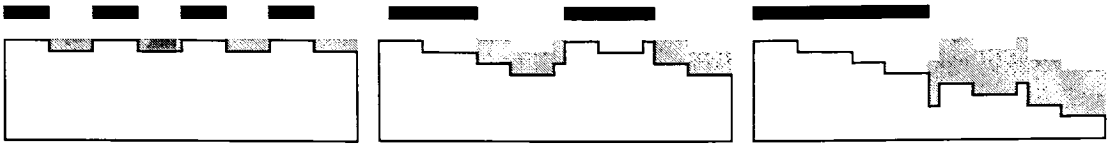

Figure 2.12

When an etch level is misaligned, the resulting profile contains "error pixels" that are equal in size to the misalignment. If the misalignment exceeds the resolution of the etch, the final profile will be distorted. A similar effect will occur if process variations alter the width of the etch mask. Consider the examples in figures 2.13 and 2.14 in which a sizing error is present in the second level etch mask.

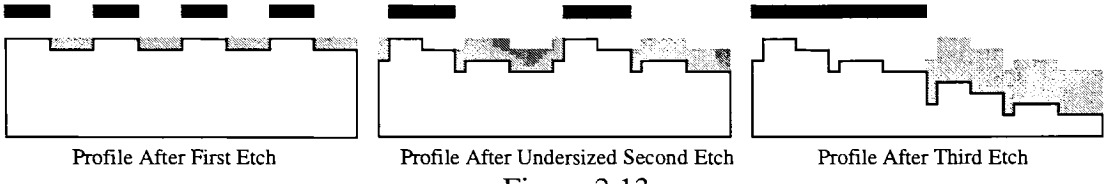

Figure 2.13

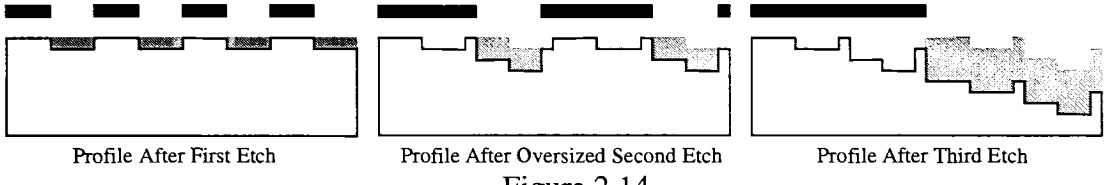

Figure 2.14

Note that an undersized etch mask produces a trough at the boundary of the misaligned etch region, while an oversized mask results in a pillar or "lip" in these areas. Etch mask dimension and mask alignment must be controlled to the same tolerances for satisfactory results to be achieved. Typical alignment tolerances range from 0.01 to 0.5 μm depending upon the application and capabilities of the etch equipment.

Alignment tolerances can be relaxed for applications such as alternating PSMs where phase regions terminate on chrome. In this case the edge of the resist mask is designed to land within the chrome region such that the chrome opening masks the phase etch rather than the resist edge which is subject to placement errors.

The following figure illustrates the fabrication steps for an eight-level binary optics microlens as described by Stern[14].

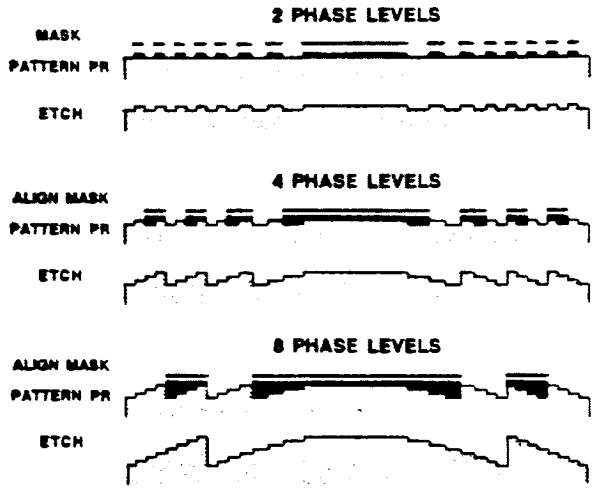

Fabrication steps for a binary optic microlens with 8 phase levels
Figure 2.15

Each zone in a Fresnel lens contains a range of etch depths corresponding to phase shifts of between 0 and one step less than 2π. The maximum etch depth, d_{max} (that corresponding to a 2π phase shift) can calculated by substituting $\Delta\phi=2\pi$ into equation 5 in chapter 2.

$$d_{\max} = \frac{\lambda}{(n-1)} \tag{7}$$

Since the etch depth is halved for each successive layer, the desired thickness d for a particular etch follows the series $d_1=d_{max}/2$, $d_2=d_{max}/4$, $d_3=d_{max}/8$ etc., or more simply:

$$d_M = \frac{\lambda}{2^M(n-1)} \tag{8}$$

where M is the etch level number, n is the refractive index, and λ is the illuminating wavelength. Note that the maximum total etch depth for a three-etch binary optics process is $d_1 + d_2 + d_3 = \frac{7}{8} d_{\max}$. Since an etch depth of d_{max} corresponding to a 2π phase shift is equivalent to a zero degree phase shift, an etch level of depth d_{max} is not needed. The situation is slightly different when binary optics techniques are used to fabricate graded phase transitions from $\pi/2$ (180 degree) to 0 phase regions in phase shifting mask applications. In this case where a full $\pi/2$ total depth is required equation 8 becomes:

$$d_M = \frac{2^{N-M-1}\lambda}{(2^N-1)(n-1)} \tag{9}$$

where N is the total number of etches.

Design of Microlenses:

The approximation of a lens using stepwise increments in phase involves the creation of a series of circular zones for each of the etch masks. The radii, r_k, of the k circular zones satisfy the relation[14],

$$\sqrt{r_k^2 + f^2} - f = k\lambda / N \tag{10}$$

where N is the number of phase steps, and f is the desired focal length of the lens. Appendix IV contains a C-program that uses equation 10 to generate a binary optic layout in CIF (Cal-tech Intermediate Format). Each zone, k, is defined by an annulus with inner and outer radii of r_k and r_{k+1} respectively. The frequency of zones will increase as N increases as N is equal to 2^j, where j is the etch number. (Note: While in this discussion etch number one (j=1) corresponds to the deepest etch, the actual fabrication process begins with the most shallow etch. This is to minimize difficulties encountered when imaging over uneven topography).

CHAPTER 3:

1DSIM 1-D Aerial Image Simulator

Introduction

1DSIM is a C-program for the simulation of 1-D aerial images based on Kintner's algorithm as described in Chapter 1. The program expands on Kintner's work to include a graphical user interface, and the ability to easily define and simulate arbitrary complex object functions including cases of defocus and the use of annular illumination. It is limited to 1-D periodic patterns and optical systems with circular apertures. (It should be noted that although the patterns are purely a function of x, it is assumed to be constant over y and does in fact represent a two-dimensional object. The modeled optical system also is described in two dimensions). The input file is a 1024-pixel complex array (in magnitude/phase format). The user is prompted to input illuminating wavelength, numerical aperture, partial coherence (σ), field size (pitch), linewidth, and defocus. The output is an array of aerial image intensity as a function of position that is both plotted on screen and written to a file. Although all features are assumed periodic, isolated features can be approximated by choosing a large pitch (field size) between features.

1DSIM: Calculation Algorithms

The loop shown below (part of the *tccmain* function) is at the core of the 1DSIM program. The inner loop (n) and outer loop (m) scan through all possible spatial frequencies where an overlap can exist between the objective pupil functions K and K* (the clear unit circles) and the condenser pupil function J (the gray circle with a radius equal to the sigma of the system). The transmission cross coefficient (TCC) (which is the region of overlap of the three circles) can thus be calculated for each pair of frequencies (n and m). The final output intensity at frequency m is the sum of the TCCs multiplied by the input function F and F* for each combination of frequencies. (These equations are described at length in Chapter 1).

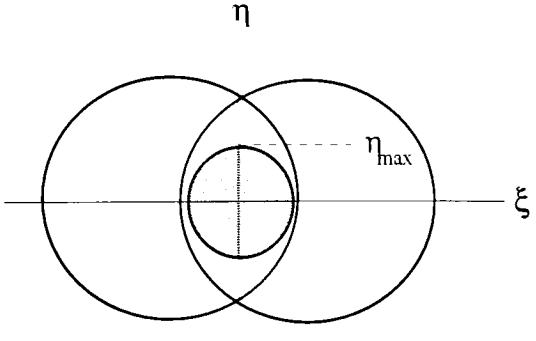

```
for(m=-1*m_index;m<=m_index;m++)
  {
    if(m<0) {mloc=m+MAXNUM;} else {mloc=m;}

    xoutput[mloc].real=0;
    xoutput[mloc].imag=0;

    for(n=-1*n_index;n<=n_index;n++)
    {
          if(n<0) {nloc=n+MAXNUM;} else {nloc=n;}
          if((n+m)<0) {nmloc=n+m+MAXNUM;} else {nmloc=n+m;}
          TCC((double)(n+m)/fieldsize,(double)(n)/fieldsize);
          tccreal=tccreal/tcc00;
          tccimag=tccimag/tcc00;

          temp_real = (xinput[nmloc].real*xinput[nloc].real)+(xinput[nloc].imag*xinput[nmloc].imag);
          temp_imag = (xinput[nmloc].imag*xinput[nloc].real)-(xinput[nloc].imag*xinput[nmloc].real);
          xoutput[mloc].real=xoutput[mloc].real + (temp_real*(float)(tccreal)) -
          (temp_imag*(float)(tccimag));
           xoutput[mloc].imag=xoutput[mloc].imag + (temp_imag*(float)(tccreal)) +
         (temp_real*(float)(tccimag));
    }
```

In a defocused system, the objective pupil functions K and K^* are no longer smooth surfaces of unit magnitude. Since these functions contain quadratic phase components, the TCCs calculated from the area on these surfaces enclosed by the union of the pupil functions will be complex valued and may not have an analytical solution. The 1DSIM program utilizes a numerical integration algorithm where the region of overlap is divided into 100 horizontal stripes of width gstep. A line integral along each horizontal stripe can be solved analytically (for the simple case of defocus as the only aberration) as the sum of sines and cosines shown in the code below. By multiplying the result by the vertical width (gstep), the area of each stripe can be approximated and summed together to give the complex TCC represented by the entire overlap region.

```
for(g=g;g<g_limit[1];g=g+gstep)
{
   rtcc=rtcc+(cos(c3*(sqrt((r1*r1)-(g*g))+o1))*gstep)-(cos(c3*(( -1*sqrt((r2*r2)-(g*g)) ) +o2))*gstep);
   itcc=itcc+(sin(c3*(sqrt((r1*r1)-(g*g))+o1))*gstep)-(sin(c3*(( -1*sqrt((r2*r2)-(g*g)) ) +o2))*gstep);
}
```

The two sections of code described above are the central to the calculations performed by the program. Many additional lines of code are dedicated to treat the various ways (cases)

the three circles can overlap so that the area can be calculated directly or (for defocused systems) the limits of the numerical integration determined.

1DSIM: User Interface Overview

I. Screen Layout

The 1DSIM user interface screen is divided into five major sections. The magnitude and phase of the input signal and the "intensity" of the output are graphically displayed on the left side of the screen. The menu bar and simulation parameter control panel are located to the right.

a) Model Input Parameters:

Magnitude and Phase Arrays

The 512 pixel magnitude and phase arrays are normalized to ± 1 and $\pm\pi$ respectively. Crude editing of these arrays can be accomplished by clicking on a line segment with the left mouse button. Holding the button will allow the segment to be "dragged" to a new location (the x and y location of the cursor will be displayed at the bottom right of the screen). Clicking on the drag boxes on either end of the segment will allow a change in the slope of the line, though "stretching" the line in the x direction is not permitted. Modification of these input arrays can also be accomplished using the "Edit" and "Layout" features on the menu bar discussed in the following sections.

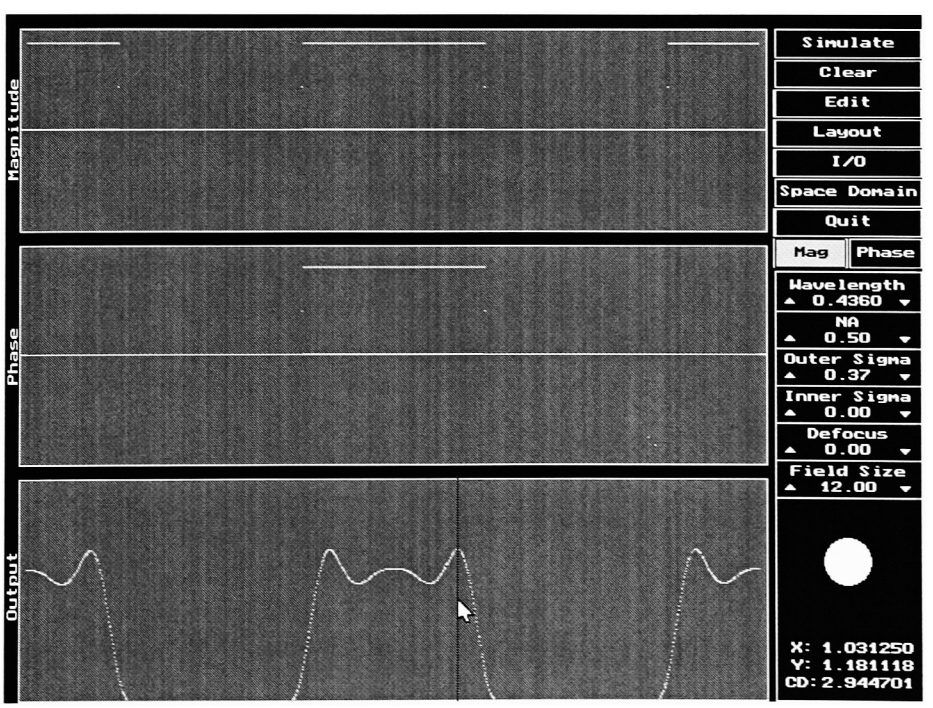

Optical System Input Parameters

The wavelength, numerical aperture (NA), partial coherence (Sigma), and defocus (μm) of the optical system to be modelled can be adjusted by clicking on the *up* and *down* arrows to the right and left of the parameters. Clicking on the area just inside the arrows of the wavelength parameter will cause the value to toggle through the wavelengths commonly used in semiconductor lithography. Wavelength values are displayed in microns.

Independent specification of an "inner" and "outer" sigma allow annuli of different dimensions to be easily specified. A graphical representation of the condenser pupil function is displayed in the lower right corner of the screen. An inner sigma of zero represents conventional illumination.

The *Field Size* parameter defines the size of the 512 pixel input window in microns. Changing this value essentially changes the horizontal scale of the input magnitude and phase windows as seen by the simulation. In the periodic line/space example shown above, since the defined field size is 12 μm, the lines and spaces are each 3 μm in with.

The magnitude and phase arrays shown in the above example are shown in the space domain. A frequency domain representation of the same input arrays can be displayed by toggling the *Space Domain* button. The vertical lines on the frequency plots indicate the numerical aperture of the system.

b) Output "Intensity" Array:

The output of a simulation run is normalized such that a constant input of unit magnitude will result in an output of unit magnitude. Magnitudes in excess of "one" result from interference effects. If the cursor is positioned in the output window a line will appear and the x and y (amplitude) coordinates corresponding to the cursor position will be displayed in the lower right portion of the screen. Holding down the left mouse button will cause the critical diminsion (CD) of the feature to be displayed. This calculation is based on where the intensity profile crosses the 30% intensity threshold to the left and right of the cursor. Selecting the *Clear* button will erase the current contents of the "Intenity" window.

c) "Edit" functions:

Selecting the Edit button enables the following three menu options:

Add RECT: Prompts the user for the magnitude, width, and center of a RECT function to be added to the input array. If the *Mag* button is highlighted, the RECT will be added to the "Magnitude" of the input array. Similarly, the *Phase* button will cause the edits to be made to the "Phase" component of the array.

Linear Phase: This function allows a linear gradient function to be added with a specified width and number of steps.

Annular: This button is highlighted when a non-zero "Inner Sigma" is specified.

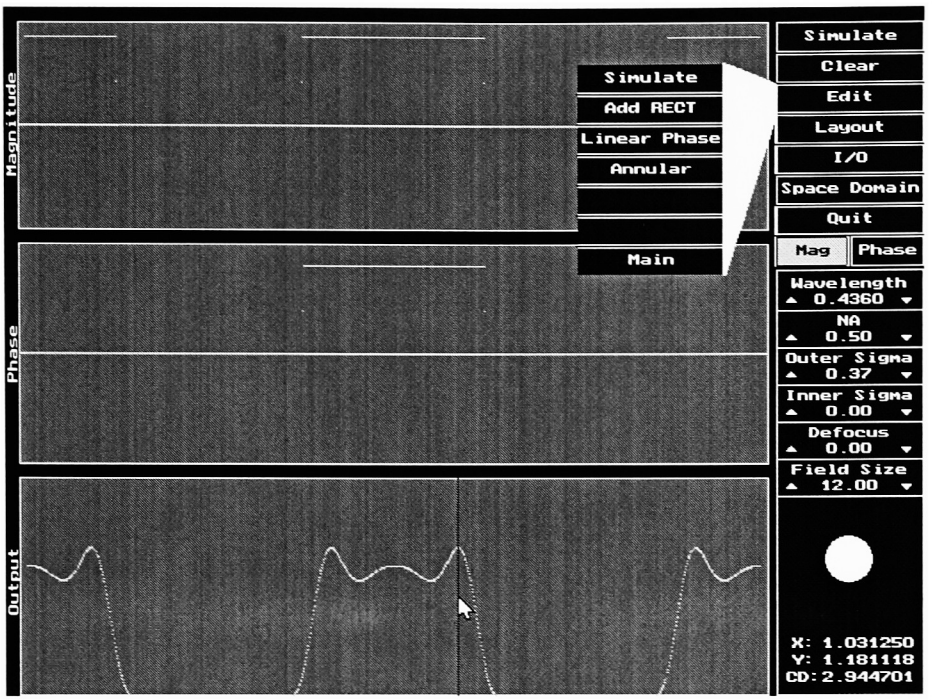

d) "Layout" functions:
Selecting the *Layout* button enables the following five menu options:

Alt PSM: Creates a periodic Alternating Phase Shifting Mask input array. The phase of each line alternates between 0 and 180 degrees.

Att PSM: Generates an input array corresponding to an Attenuated Phase Shifting Mask. The "dark" spaces between the lines actually contain 9% of the total intensity. The light transmitted through these spaces is phase shifted by 180 degrees from the light transmitted through the lines.

Rim PSM: Generates an input array representing an isolated Rim Phase Shifted Line.

Standard: Creates a standard "binary" or "magnitude only" periodic mask.

Chromeless: Creates a chromeless (0 and 180 degree phase only) periodic pattern.

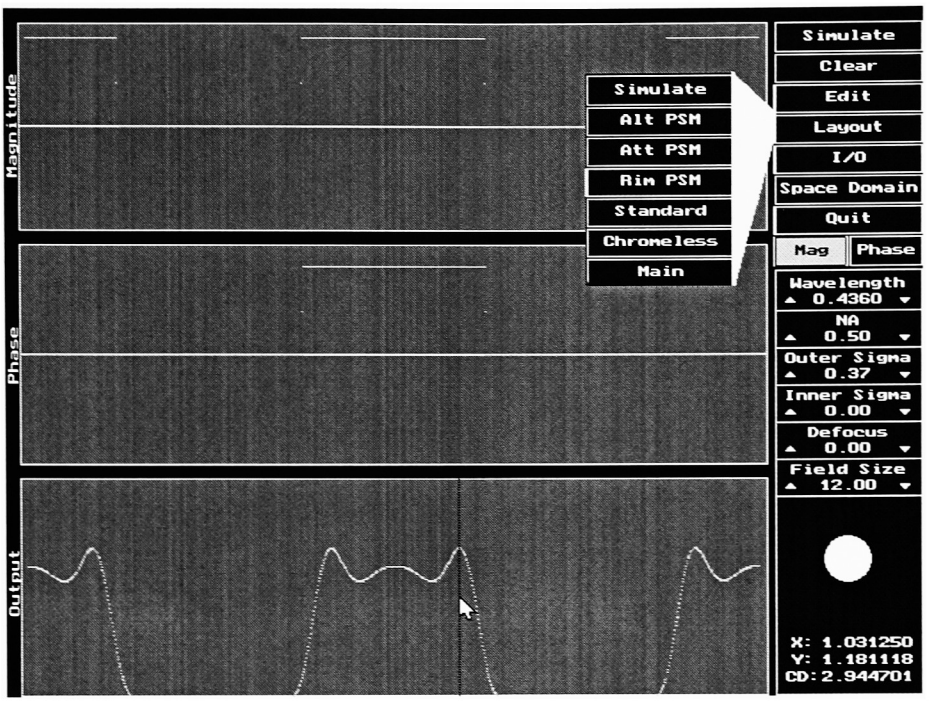

e) "I/O" functions:
Selecting the *Layout* button enables the following five menu options:

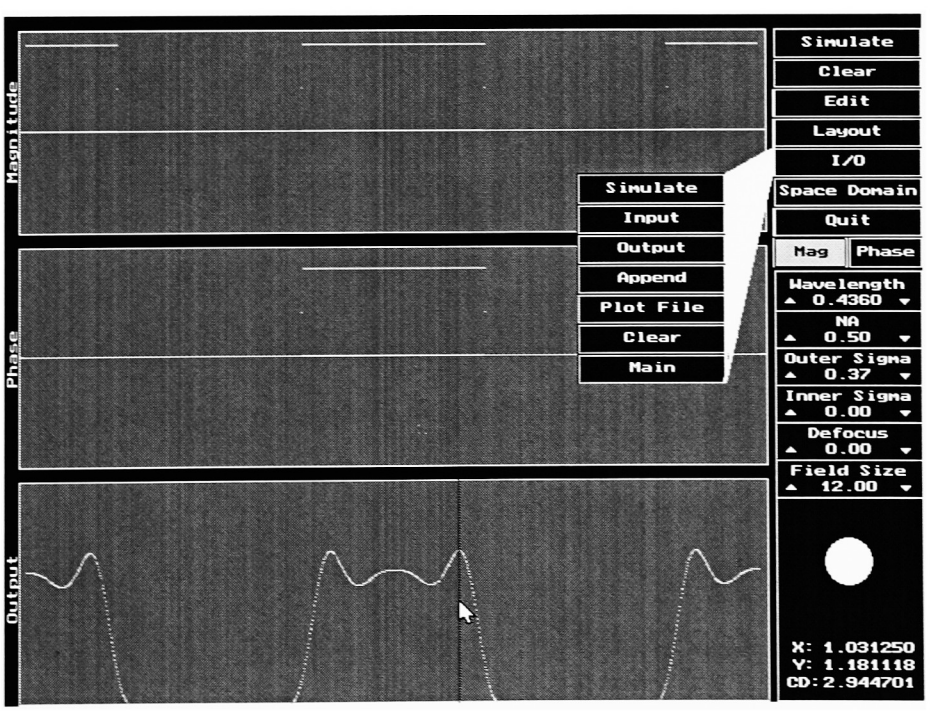

Input: Prompts the user to specify the name of an input array file of the form shown in appendix 5.

Output: Writes the X (coordinate) and Y (intensity) data from the output array to the 1DSIM.OUT file. The format of this file is also shown in appendix 5.
Note: The existing 1DSIM.OUT file is overwritten each time this option is sellected.

Append: Performs the same function as Output except that the data is appended to 1DSIM.OUT (the previous output is not overwritten).

CHAPTER 4:
Approach: Design and Fabrication of Complex Phase Masks

Introduction:

This section describes the experimental approach used in the design and fabrication of complex phase masks. Design targets, process flows, and mask layout information are discussed in detail.

Etch Depth Target Values:

The following table contains etch depths in fused silica for an eight-phase binary optics process corresponding to a 2π phase shift at commonly used wavelengths. These values were calculated using equation (3) in chapter 2.

Wavelength (nm)	Refractive Index	d_1	d_2	d_3	d_{Total}
193	1.561	1263	631	316	2210
248	1.508	1395	697	349	2441
365	1.476	3834	1917	958	6709
436	1.467	4668	2334	1167	8169
441	1.467	4721	2361	1180	8262
632	1.4572	6990	3490	1750	12230

Table 4.1

Table 4.2 contains etch depths for a $\pi/2$ phase shifting mask using binary optics at wavelengths typically used in optical lithography. (Again calculations are based on fused silica phase shifter material).

Wavelength (nm)	Refractive Index	d_1	d_2	d_3	d_{Total}
193	1.561	983	491	246	1720
248	1.508	1395	697	349	2441
365	1.476	2191	1095	548	3834
436	1.467	2667	1334	667	4668

Table 4.2

Test Mask Design:

Binary Optic Phase Shifting Mask Layout:

The eight-level phase shifting mask layout shown in figure 4.1 contains an array of twenty electrical linewidth modules designed to measure features from 0.4 to 1.8 microns. These 0.5mm by 1.5mm modules utilize a standard 16 pad configuration for the Prometrix Lithomap EM1 electrical probe station. Contact size and linewidth structures for each individual feature size are contained on different modules, with each module

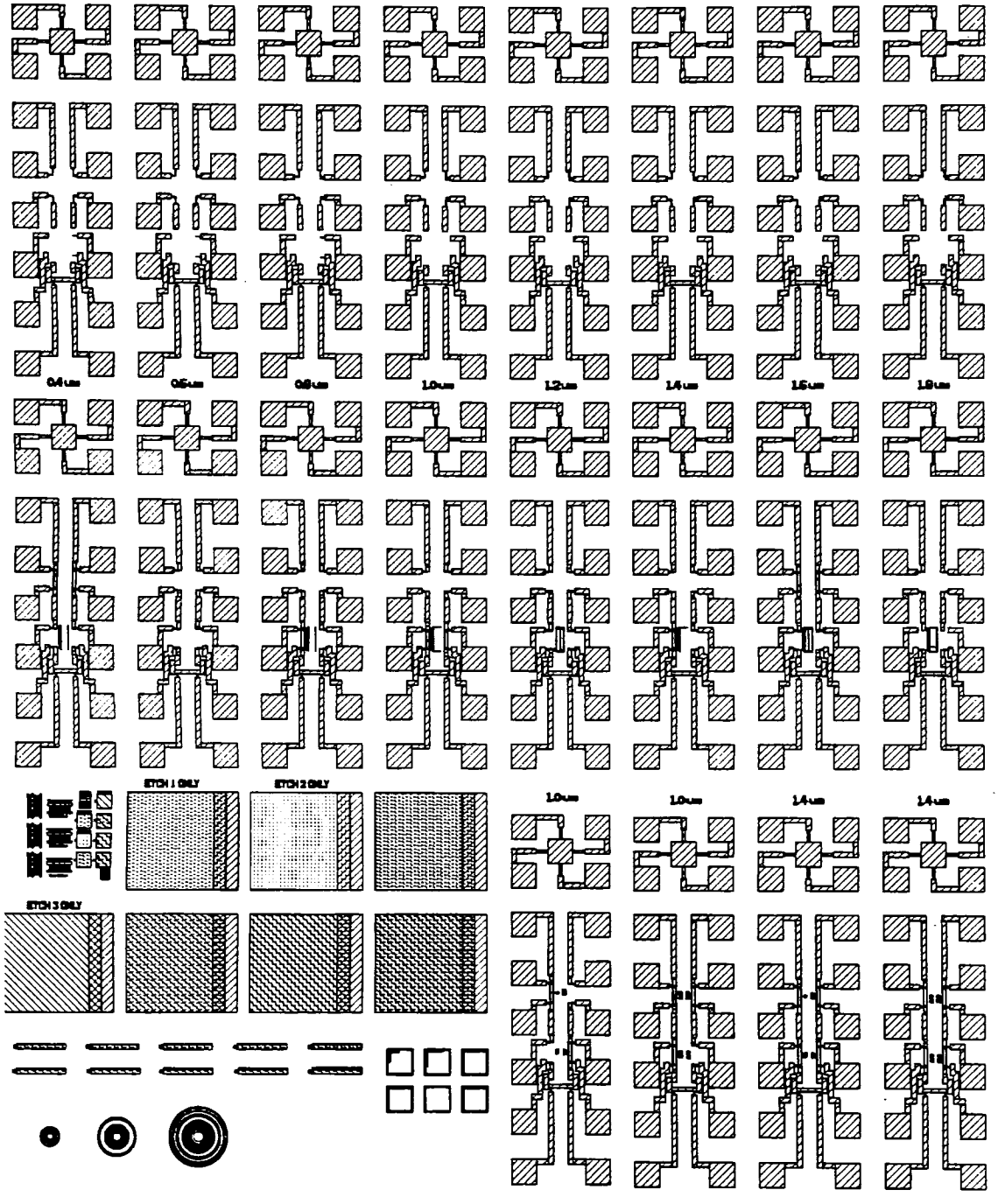

Eight-level phase shifting mask layout. Design includes electrical linewidth and contact size measurement structures, phase gradient test structures, microlenses, and etch depth measurement sites.

Figure 4.1

further divided into four independent test structures. Linewidth modules contain: a densely packed equal line/space size line structure, an identical dense line structure with alternating phase shifting, an isolated line, and an isolated line with rim phase shifting. Contact modules contain; standard contacts, "biased" contacts, rim shifted contacts, and

outrigger-type contacts. Figure 4.2 shows the linewidth and contact modules for the 1.8 micron feature size. A enlargement of the 8 individual structures in included in figure 4.3. Contacts are placed in a 3 by 19 array with a four micron center-to-center spacing.

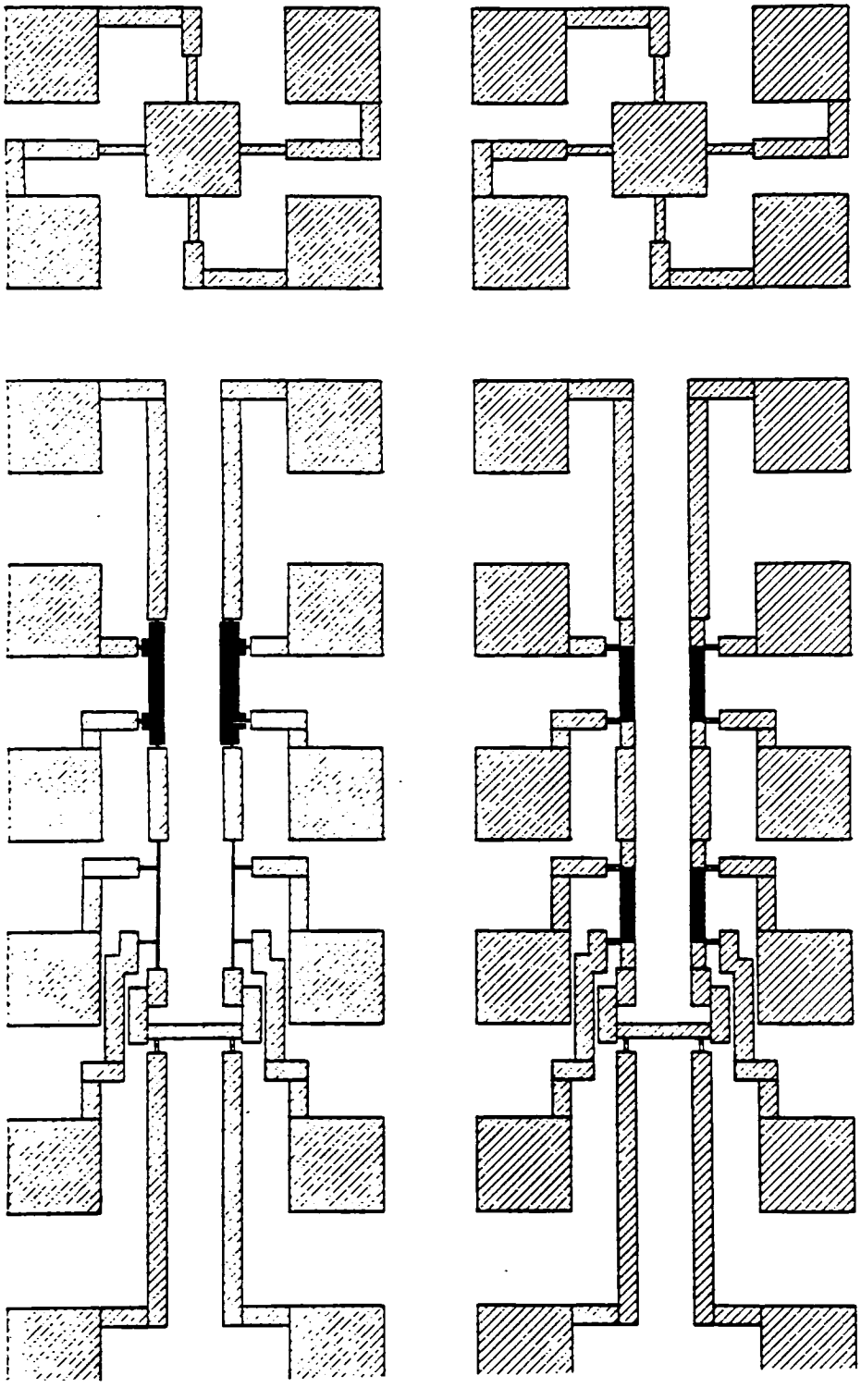

Enlarged view of 1.8um electrical measurement structures.
Figure 4.2

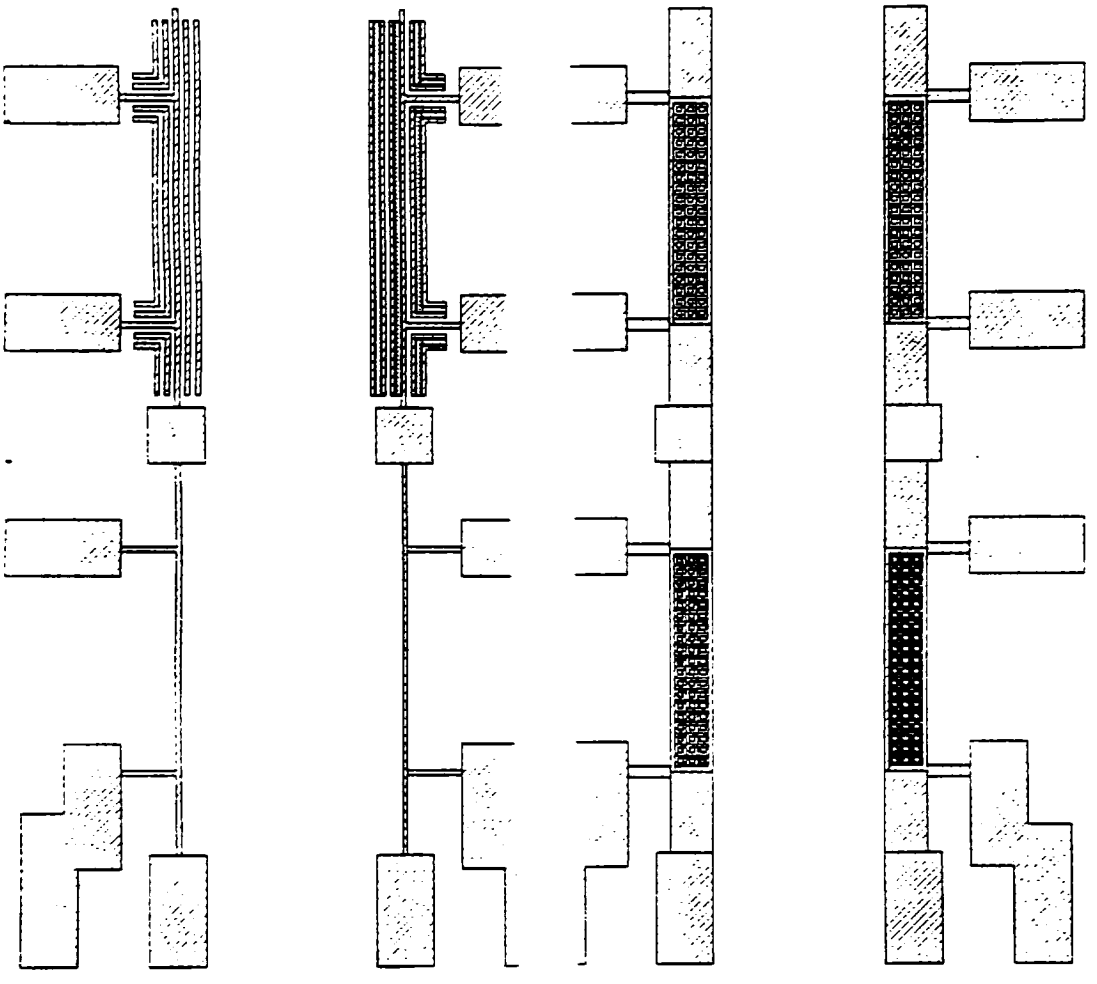

Magnified view of electrical measurement sites. Nested and Isolated lines are show with and without phase shifting elements. Arrays of phase shifted and non-phase shifted contacts are also shown.

Figure 4.3

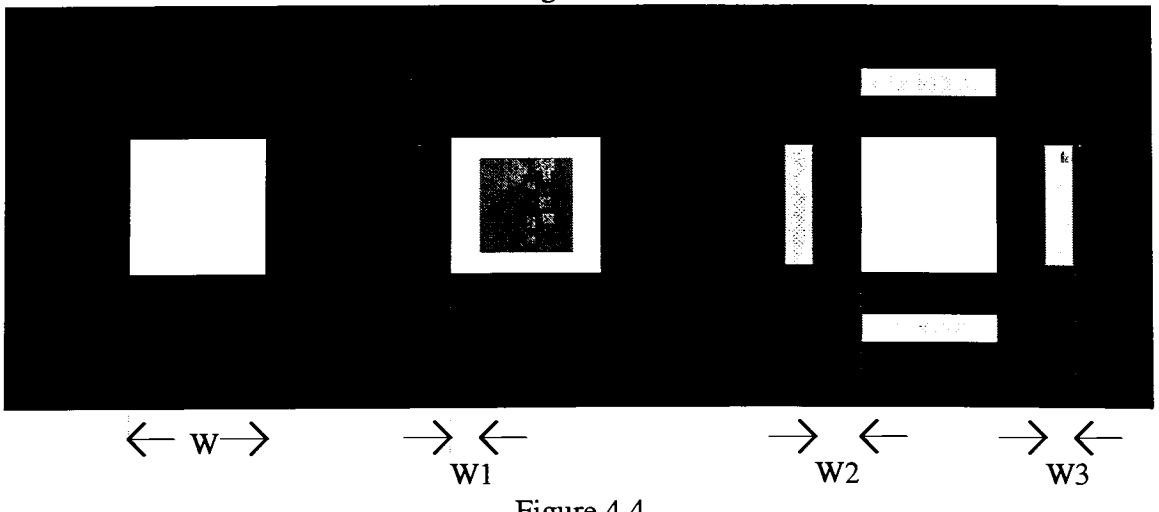

Figure 4.4

Table 4.3 contains the dimensions of each of the four contact types for given feature sizes. A minimum mask feature size of 2μm was used to remain within the capability of the positive resist process used. Since the actual mask is scaled 5X, this 2μm design rule corresponds to a 0.4μm minimum feature size in the chip layout. (Note all outrigger widths (W2) are at this minimum size). Simulations were performed using SPLAT[11] and the 1DSIM program to optimize these designs within the limitations of the fabrication process.

	Standard	Biased	Rim		Outrigger		
	W (μm)	W (μm)	W (μm)	W1(μm)	W(μm)	W2(μm)	W3(μm)
0.4μm	0.4	0.5	1.0	0.2	0.8	0.3	0.4
0.6μm	0.6	0.7	1.1	0.2	0.8	0.5	0.4
0.6μm	0.8	0.9	1.2	0.2	1.0	0.2	0.4
1.0μm	1.0	1.1	1.3	0.2	1.1	0.4	0.4
1.2μm	1.2	1.3	1.5	0.2	1.4	0.4	0.4
1.4μm	1.4	1.5	1.7	0.2	1.5	0.4	0.4
1.6μm	1.6	1.7	2.0	0.2	1.6	0.5	0.4
1.8μm	1.8	1.9	2.2	0.2	1.8	0.5	0.4

Table 4.3

Dense and isolated line layouts are unbiased with equal sized lines and spaces. The 1.0 μm linewidth module for example, contains densely packed 1μm lines separated by 1μm, and 1μm isolated lines.

The lower left (figure 4.1) section of the layout contains process metrology structures as well as chromeless test patterns and non-functional microlenses. (These lenses were included for test purposes. The etch depths used to create a G-line phase shifting reticle are different than those needed for the microlenses). Metrology structures include optical alignment verniers and large etch trenches for AlphaStep measurements.

Chromeless "dark field" checkerboard arrays have been included with pixel sizes of 0.5, 1.0, 1.5, 2.0, 3.0 and 4.0μm. These values correspond to 0.33, 0.66, 1.0, 1.33, 2.0, and 2.66 λ/NA using G-line (0.436μm) illumination with an NA of 0.29.

Quartz Microlens Test Reticle Layout

The microlens test reticle layout is shown in figure 4.5. Each quadrant contains a 4x4 array of identical lenses. Lenses were designed using the layout program contained in appendix IV for use with a 441nm He-Cad laser. This laser was selected because it is close to the 436nm mercury arc lamp peak used in the GCA 6700 stepper. Lens diameters were limited by the point at which the zone widths reached the 2μm resolution limit of the fabrication process.

Focal Length (mm)	Lens Diameter	F#
5	0.3mm	16.66
15	0.8mm	18.75
25	1.8mm	13.9
35	2.5mm	14

Table 4.4

Alignment and etch metrology structures have been included at the bottom of the layout. Box-in-box alignment structures are located at the outer four corners.

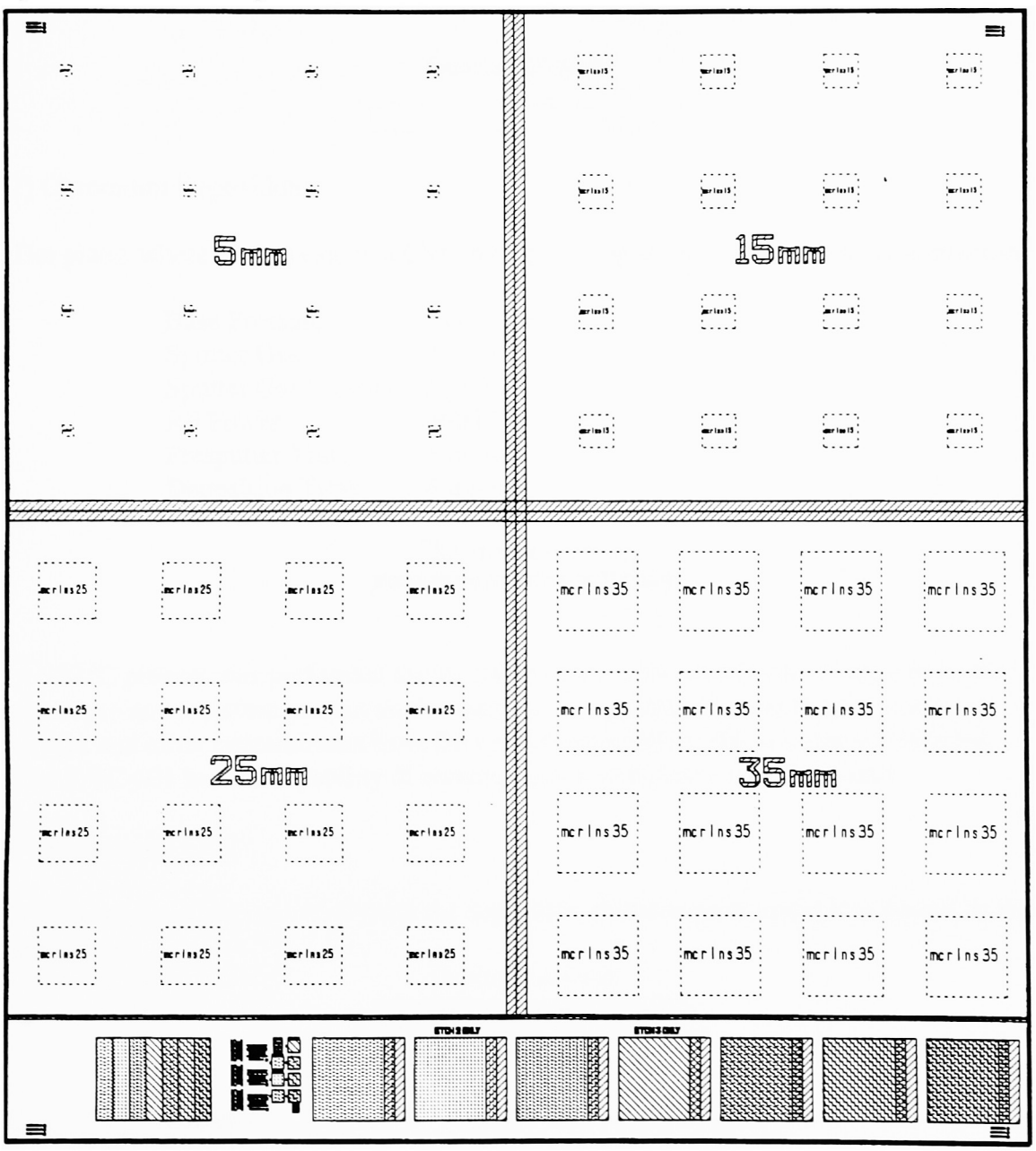

Layout of the microlens array test mask. Focal lengths of 5, 15, 25, and 35mm are represented.

Figure 4.5

Experimental Procedure (Mask Fabrication Process Flow):

1) Substrate preparation:

Five-inch square EMT fused silica (quartz) plates were first stripped in NanoStrip (to remove any photoresist or other organic material) and placed in chrome etch (CR-9) to clear any residual chrome from the plate. A gentle scrub using CA-40 photomask cleaning solution was performed to remove particulate from the surface. Plates were then rinsed, air dried, and dehydrated in a convection oven at 170°C for 2 hours.

Quartz Substrate

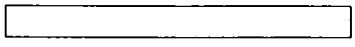

2) Chromium Deposition:

The plates where then placed in a CVC-601 sputtering system with typical parameters of:

Base Pressure	: $3x10^{-6}$ torr
Sputter Gas	: Argon
Sputter Gas Pressure	: 5 mtorr
RF Power	: 3600 Watts
Presputter Time	: 5 minutes
Deposition Time	: 4 minutes

Chrome Deposition

A 300°C preheat was performed during pump down to minimize outgassing and further eliminate any moisture present on the samples. The presputter is performed to remove oxides and other contaminants from the sputter target before the samples are exposed. The CVC 601 has the capability of coating eight 5 inch plates simultaneously.

3) Photoresist Coat:

Within minutes after removal from the deposition chamber photoresist was coated on the substrates.

Photoresist Coat

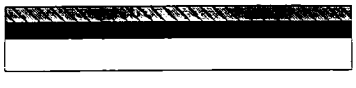

Material	: OeBr 514 Photoresist Lot#
Spin Speed	: 2000rpm
Spin Time	: 30 seconds

Bake (Hotplate) : 2 min. at 110°C
Expected Thickness : 6000Å

4) Electron Beam Exposure and Development:

Exposures were conducted on a MEBES I (Manufacturing Electron Beam System). MEBES job decks used have been included in Appendix 3. This initial exposure delineates the chrome (attenuating layer) as well as the alignment marks used to properly overlay subsequent levels.

Beam Diameter : 0.5 μm
Address Size : 0.5 μm
Beam Current : 40 nanoamps
Accelerating Voltage : 10 KV
Exposure Dose : 17 uC (17 repeat counts)
Post Exposure Bake : None
Developer : 5:4 PLSI developer to DI water
Develop Time : 2 min

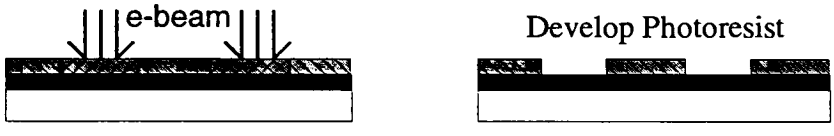

5) Chromium Etch

The chrome was removed using Cyantek CR-9 Chromium photomask etchant. Etch times ranged from 60 to 90 seconds with agitation depending on the chrome thickness and age of the etch solution. Plates were removed approximately 15 seconds after the time the field appeared to clear.

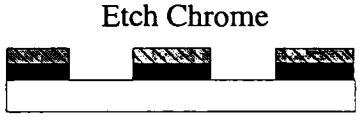

6) Photoresist Strip and Dehydration Bake

Photoresist was removed by placing the masks in Nanostrip for 10 minutes. The plates were then rinsed and spin dried before being placed in a convection oven at 170°C for 2 hours to ensure dryness.

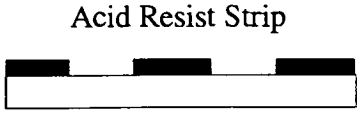

7) Aluminum Deposition

Masks were taken directly from the convection oven and placed in the CVC601 sputtering system.

Base Pressure	: $3x10^{-6}$ torr
Sputter Gas	: Argon
Sputter Gas Pressure	: 5 mtorr
RF Power	: 3600 Watts
Presputter Time	: 5 minutes
Deposition Time	: 2.5 to 3.5 minutes

Final aluminum thicknesses were measured using a Tencor Alpha-Step profilometer and ranged between 1100 and 1500 angstroms depending on the deposition time.

Aluminum Deposition

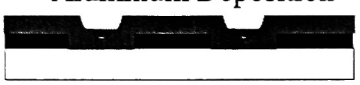

The aluminum layer is necessary to ensure a conductive substrate during the subsequent electron beam exposure. If a layer of photoresist was coated directly over quartz and exposed via electron beam, charge buildup in the quartz would divert the beam and distort the pattern.

8) Photoresist Coat:

Within minutes after removal from the deposition chamber photoresist was coated on the substrates.

Material	: OeBr 514 Photoresist Lot#
Spin Speed	: 2000rpm
Spin Time	: 30 seconds
Bake (Hotplate)	: 2 min. at 110°C
Expected Thickness	: 6000Å

Photoresist Coat

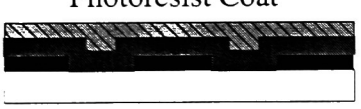

9) Electron Beam Exposure and Development of Phase Levels:

Phase level exposures were conducted on a MEBES I (Manufacturing Electron Beam System). MEBES job decks used have been included in Appendix 3. This exposure delineates the aluminum pattern that defines areas exposed to the oxide (quartz) etch process. Marks patterned in the chrome layer are used for alignment.

Beam Diameter	: 0.5 μm

Address Size	: 0.5 μm
Beam Current	: 40 nanoamps
Accelerating Voltage	: 10 KV
Exposure Dose	: 17 uC (17 repeat counts)
Post Exposure Bake	: None
Developer	: 5:4 PLSI developer to DI water
Develop Time	: 2 min

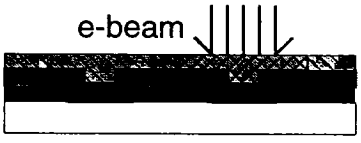

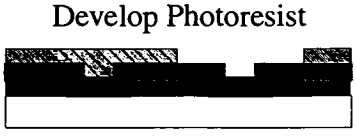

10) Aluminum Etch

Aluminum etching is accomplished by submerging the plate in a solution that is 16 parts phosphoric acid, 1 part nitric acid, 1 part acetic acid, and 1 part water.

Etch Temperature	: 40°C
Etch Time	: 45-60 seconds
Etch Rate	: 2000 Å/min

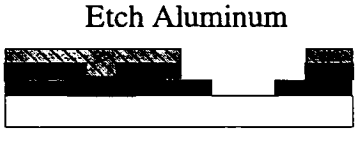

11) Plasma Etch Process

A low pressure oxygen plasma was struck in an empty chamber before the first plate of a given session was etched to clean the chamber. These were conducted at 300 mtorr, 100W, with 50 sccms of O_2 for times in excess of 10 minutes.

The plasma etch process that followed involved two stages accomplished sequentially without removing the plate from the plasma chamber; plasma photoresist strip, and quartz etch. The first step was an oxygen plasma that removed the photoresist.

Gas Flow	: 50 sccms O_2
Pressure	: 50 mtorr
Power	: 100W
Temperature	: 28°C
Time	: 10 minutes

After Plasma Resist Strip

The second etch utilized a CF_4 plasma to etch the quartz substrate material not protected by either chrome or aluminum. The use of these materials as etch masks (rather than the photoresist itself) eliminated the need to add hydrogen to the plasma to improve selectivity to photoresist.

Gas Flow	: 50 sccms CF_4
Pressure	: 19.4-19.7 mtorr
Power	: 150W
Temperature	: 28°C
Etch Rate	: 260 Å/min

After Quartz Etch

12) Aluminum (Acid) Strip

This final step removed the aluminum etch mask using the same solution described in step 10. A higher temperature and extended etch time were used to ensure complete aluminum removal in the presence of a polymer film deposited during the quartz etch.

Etch Temperature	: 50°C
Etch Time	: 15 minutes

Final Profile

CHAPTER 5:

Results: 1DSIM, Binary Optics, and Microlenses

1DSIM Program Simulation Results:

Sample outputs from the 1DSIM program are shown in figures 5.1 and 5.2. A grating of equal (1μm) line space pairs (fieldsize=2) was used in both examples. Partial coherence (σ) values of 0.05 (approximately coherent), 0.50 (partially coherent), and 1.0 (approximately incoherent) are shown for each. The system in figure 5.1 easily resolves the 1μm features. Note that the coherent and partially coherent images exhibit superior image slope and modulation (based on maximum intensity) than the incoherent image. As expected, a significant amount of ringing is present in the coherent image that is eliminated in the incoherent case. Values larger than unity are due to constructive interference. The normalization of intensity is such that a "blank" field will produce an output of unit magnitude. Small negative "intensities" are artifacts of the inverse Fourier transform process.

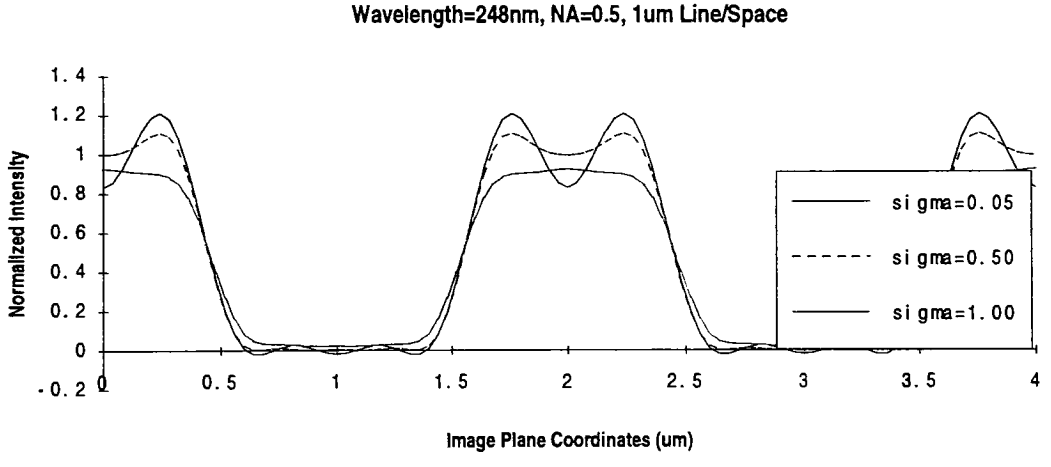

Sample output of 1DSIM program showing the image of a 1um line/space pattern using 248nm illumination and different partial coherence (sigma) values.
Figure 5.1

The same input is near the coherent resolution limit of the system shown in figure 5.2. Since only one Fourier component is present, there is no ringing in any of the images. Again the maximum modulation is produced with coherent illumination.

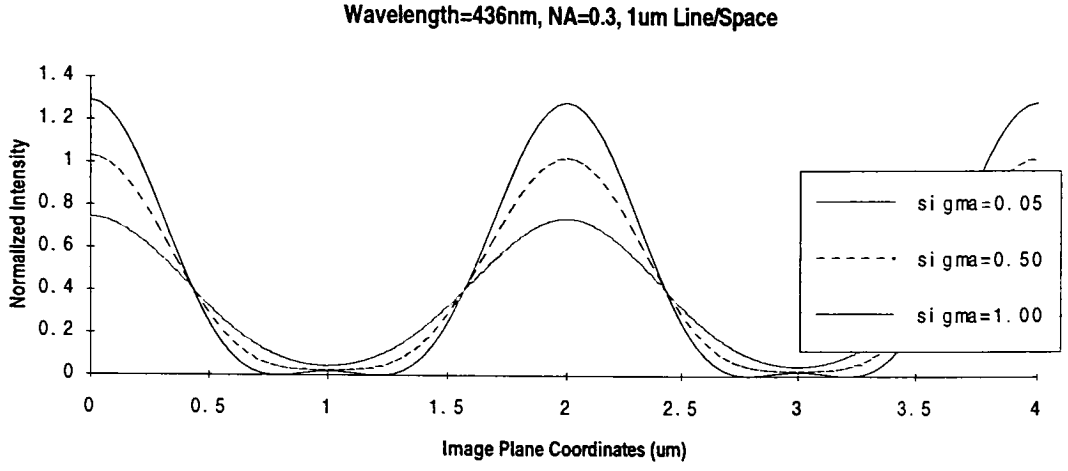

Sample output of 1DSIM program showing the image of a 1um line/space pattern using 436nm illumination and different partial coherence (sigma) values.
Figure 5.2

Etch Process Results

Optimization of an oxide etch process involves four major variables; power, pressure, gas flow rate, and fluorine-to-carbon (F/C) ratio. (A detailed description of this process is included in Appendix II: Reactive Ion Etching of Fused Silica). The F/C ratio is controlled by the type and relative quantity of gas species used. Initial experiments were conducted using pure CF_4 since the relatively aggressive 4:1 F/C ratio was likely to produce fused silica etching over a wide range of process parameters. Samples were prepared by imaging an optical photoresist (Shipley 812) an a bare 5 inch chrome plate using a GCA4800 photorepeater. Typical results are shown in table 5.1.

Gas Type/Flow Rate (sccms)	Power (Watts)	Pressure (mtorr)	Etch Rate (Å/min)	Selectivity
CF_4/75	75	100	200	1:2.5
CF_4/75	75	200	70	1:1.4
CF_4/75	140	100	480	1:2.6

Table 5.1

Etch rates were enhanced as power increased and pressure decreased since both high power and low pressure raise the bombardment energy of ions in the plasma. Etch rate of the photoresist in all cases exceeded that of the fused silica by roughly a factor of two. While oxide etching involves both chemical and physical processes, photoresist removal is almost exclusively the result of the physical bombardment. For this reason, the conditions that enhanced the fused silica etch rates also degraded selectivity.

Hydrogen was added to facilitate the formation of a protective polymer film over the photoresist to improve selectivity. It should be noted that while Table 5.2 shows fairly typical values, etch rates varied dramatically from 0 to 130 Å/min.

Gas Type/Flow Rate (sccms)	Power (Watts)	Pressure (mtorr)	Etch Rate (Å/min)	Selectivity
CF_4/75 H_2/8	75	100	0	NA
CF_4/75 H_2/8	75	200	0	NA
CF_4/75 H_2/4	75	100	130	>5:1
CF_4/75 H_2/4	140	100	100	>5:1

Table 5.2

Hydrogen concentrations of around ten percent (8 sccms) caused all etching to cease, while five percent hydrogen produced low etch rates with high values of selectivity. If consistent etch rates could be maintained the later case would be ideal for controlled phase etches. Unfortunately, this was not the case since the operating point of the process was near the boundary between polymerization (0 etch rate) and selective etching. At this point small variations in gas flow or pressure could produce a substantial on the rate of polymer deposition and corresponding changes in the etch rate.

Since changes in hydrogen concentration were found to strongly impact the etch rate, a sequence of tests were conducted using pure CHF_3. The inclusion of hydrogen directly within the etch species ensured a fixed hydrogen concentration by eliminating possible fluctuations caused by a hydrogen mass flow controller (MFC). In an attempt to further reduce etch rate variability, the pressure was reduced to 50 mtorr to increase bombardment and reduce instability due to excessive polymerization over the etched areas. The following table contains initial data from the CHF_3 process.

Gas Type/Flow Rate (sccms)	Power (Watts)	Pressure (mtorr)	Etch Time (m:s)	Etch Depth (Å)	Etch Rate (Å/min)	Selectivity
CHF_3/100	100	50	27:00	4100	152	>5:1
CHF_3/100	100	50	10:00	1750	175	>5:1
CHF_3/100	100	50	15:00	2450	163	>5:1
CHF_3/100	100	50	08:30	828	97.5	>5:1
CHF_3/100	100	50	04:15	0	0	NA
CHF_3/100	100	50	15:00	0	0	NA

Table 5.3

While the first three runs listed (performed on different days) exhibit a reasonably consistent etch rate of around 160Å/min, the etches that immediately followed the third etch demonstrated a sharp decline and eventual cessation of the rate of oxide removal. This behavior is indicative of increased polymer deposition, possibly due to the buildup of contamination from sputtered photoresist or a rise in operating temperature, since temperature was not controlled on the machine. A series of tests were conducted to better understand these effects. A plate with resist over patterned aluminum (see step 10 in the process sequence of the procedure section) was placed in the etcher following a 20

minute oxygen chamber clean. Table 5.4 documents the sequence of process steps performed on this plate.

Gas Type/Flow Rate (sccms)	Power (Watts)	Pressure (mtorr)	Temp (°C)	Etch Time (m:s)	Etch Depth (Å)	Etch Rate (Å/min)
CF_4/50	100	50	27	11:00	3000	270
O_2/50	100	50	27	10:00	NA	NA
CF_4/50	100	50	26	4:00	0	0
CF_4/50	100	50	26	7:00	0	0
CF_4/50	100	20	26	7:00	1000	142

Table 5.4

Following the initial etch, subsequent CF_4 etches of 4 and 7 minutes failed to produce any additional oxide removal at a constant temperature of 26 °C. Only after the pressure was reduced to 20 mtorr did etching resume. These results support the theory that a layer of polymer was deposited on the fused silica surface that inhibited the etch process. Increasing the bombardment energy (by lowing the pressure) accelerated the removal of this film via sputtering and enabled the oxide etch to resume.

The etch process parameters used for the fabrication of the fused silica microlenses and phase shifting masks were chosen to maintain a high level of bombardment to limit the effect of polymer formation on etch rate and minimize contamination due to resist removed via sputtering. Redeposition of this material in the etched regions was another potential source of variability to be avoided. A two stage etch process was introduced to minimize these effects in which the resist was removed in an oxygen plasma immediately prior to the CF_4 fused silica etch.

The plates (again at stage 10 - patterned aluminum and with photoresist) were first placed in a low pressure oxygen plasma for 10 minutes. Typically all resist was removed within the first five minutes. Additional time was allowed for the substrate to reach a stable temperature and provide an opportunity for the deadsorption of volatile contaminants on the fused silica surface (i.e water). It was hoped that the resulting surface conditions would be fairly consistent from plate to plate.

Immediately (within 60 seconds) following the oxygen plasma, the CF4 plasma was initiated at 20 mtorr and 150W. These values maximized bombardment while maintaining sufficient fluorine concentrations to facilitate etching. (It should be noted that the availability of chrome and aluminum as etch mask materials enabled the use of plasma conditions beyond the range suitable for a typical photoresist etch mask with sufficient selectivity). The resulting process exhibited excellent stability over a period of weeks and dozens of process runs.

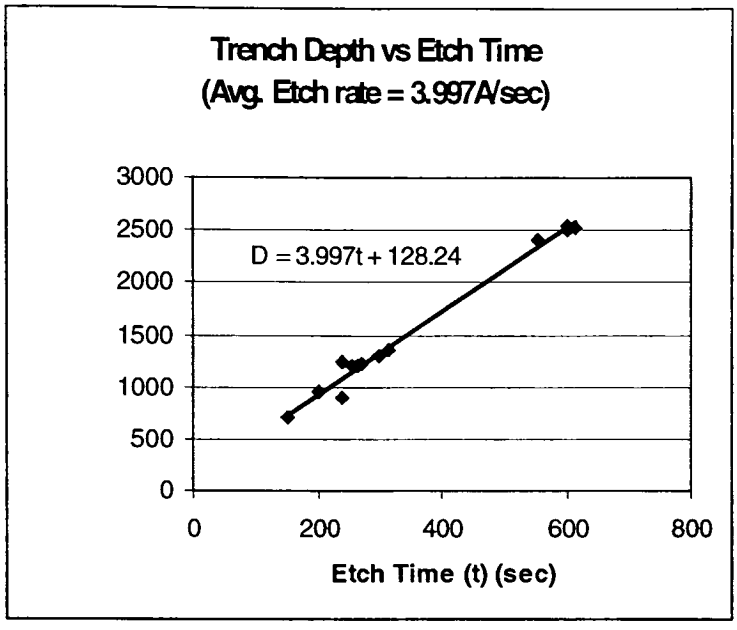

Demonstration of etch rate stability for multiple runs nsing the fused silica etch process developed for the fabrication of complex phase masks.

Figure 5.3

The etch rates are closely distributed around the average of 265 Å/min with the exception of two outliers at 225 and 312 Å/min. Deeper etches were done in two or three steps with measurements to adjust etch times as needed. In most cases target depths were hit within 100 Å.

Etch process optimization involved the removal of material in previously unetched regions. To produce a phase gradient using binary optics it is necessary to etch a region as many as three times. The binary optic fabrication technique described in chapter 2 assumes material is removed from previously unetched regions at the same rate as in areas that were etched in an earlier process step. It is conceivable that the initial polished fused silica surface could etch slower than a rough etched region with more exposed surface area. The following table contains data from each of the seven "phase steps" for three G-line binary optic phase shift masks. The actual measured step height is compared to the height estimated by summing the contribution of each individual etch. For example, the 1+2 data in the far left set shows a measured depth of 2025Å, while the theoretical sum of the first two etches (1075+1175=2250) is 225Å higher than the measured value.

Etch	Actual (Å)	Est. (Å)	Diff. (Å)
1	1075	-	-
2	1175	-	-
1+2	2025	2250	-225
3	2500	-	
1+3	3900	3575	+325
2+3	3875	3675	+200
1+2+3	4800	4750	+50

Actual (Å)	Est. (Å)	Diff. (Å)
750	-	-
1350	-	-
2175	2100	+75
2525	-	
3425	3275	+150
4000	3875	+125
4800	4625	+175

Actual (Å)	Est. (Å)	Diff. (Å)
950	-	-
1325	-	-
2325	2275	+50
-	-	-
3500	-	-
3875	3875?	0?
4800	4725?	+75?

Table 5.5

In general, combinations of etches exceeded the sum of their individual components by between 50 and 300Å. It is likely these discrepancies are in part due to systematic measurement errors related to the different scales used. (The 750Å step was measured in the 0 to 1000Å range while 4800Å steps required the use of the 0-10000Å scale). The measurements themselves exhibit uncertainties of at least +/- 50Å that are compounded when readings are added together. Although the differences are small compared to the uncertainties, the positive trend in the data may warrant further study.

Registration Data

The microlens test mask contained box-in-box verniers such as those shown in figure 5.4. Alignment errors are found by measuring the offset of the second level (center box) from the center of the first level. The Nikon 2i measurement system was used to collect the data shown in Table 5.6 by scanning a laser across the surface and detecting edge positions.

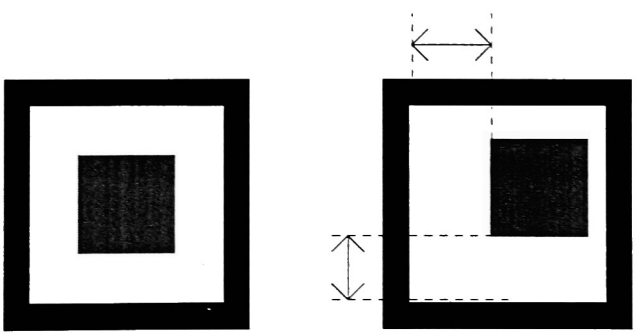

Correctly Aligned Misaligned

Figure 5.4

The following tables contain misalignment data measured using the box-in-box structures on the two microlens test reticles fabricated. Offsets of the first and second level fused silica etches to the chrome level (which contains the alignment flag used to register the electron beam) are given in microns.

Plate #1	Level 1		Level 2	
Location	X error (μm)	Y error (μm)	X error (μm)	Y error (μm)
Upper Left	-0.24	-0.07	-0.69	+0.46
Upper Right	-0.39	-0.38	-0.56	-0.32
Lower Left	-	-	-	-
Lower Right	-0.17	-0.01	-0.68	-

Plate #2	Level 1		Level 2	
Location	X error (μm)	Y error (μm)	X error (μm)	Y error (μm)
Upper Left	-1.18	+0.845	-0.06	-0.355
Upper Right	-0.795	+0.565	+0.27	-0.595
Lower Left	-	-	-	-
Lower Right	-1.09	+0.82	-0.06	-0.515

Table 5.6

At the time these plates were fabricated the electron beam system had been suffering chronic stage drift problems as large as 0.75μm so registration errors of this magnitude were expected in some areas. Most errors are around 0.5μm or less though values range from -1.18 to +0.82μm on the second plate. The fluctuation of these values is more characteristic of a stage drive problem than a gross system alignment error that would tend to produce more uniform alignment offsets at all positions. Such would be the case if there was a translation error in the registration process. For both plates, the alignment errors in the upper left corner correspond closely to those in the lower right. This is likely related to the fact that the pattern is written in "stripes" from top to bottom starting at the left and proceeding to the right. The shorter the time between the exposure of the alignment marks, the less likely a significant drift will be encountered to shift the offsets.

The fact that the first and second level errors at the same reticle position do not seem to correlate, shows that it is unlikely any systematic error in the position or reading of the alignment targets is responsible for the bulk of the error.

Surface Roughness of Etched Fused Silica:

Surface roughness is a critical concern for optical elements created using reactive ion etching techniques. Excessive roughness can cause scattering that reduces the transmitted intensity. Close examination of the steps in figure 5.5 reveals surface roughness on the order of 50 to 100 angstroms. Separate scans were done on each of the eight phase levels (from no etch to the sum of all three etches) to measure this roughness. The results of these scans are shown in figure 5.7. Gradual slopes over the length of the 3.5μm scans are due to sample tilt and should be disregarded. The zones 6 and 7 exhibit higher surface roughness than the other zones with the exception of zone 1. As expected, regions exposed to more etching exhibit greater surface roughness. (Zone 1 may be due to an

unfortunate choice of scan regions). Nevertheless, the differences between unetched and heavily etched regions are only on the order of 50 angstroms.

Figure 5.5 shows a line scan made over three zones of a microlens using an atomic force microscope (AFM). Note in reality each plateau is essentially flat. The slope within each "step" (including the steep decline at the far right) is due to a combination of sample tilt and nonlinearities in the piezoelectric stage drive. The largest step (around 4800Å) corresponds to the full π phase shift if exposed at 436nm. Note the two "spikes" near the center of the image bordering the center step. This is indicative of an undersized etch mask (in this case for the first etch level) as illustrated in figure 2.4. An image compiled from an array of scans such as than in figure 5.5 is shown in figure 5.6.

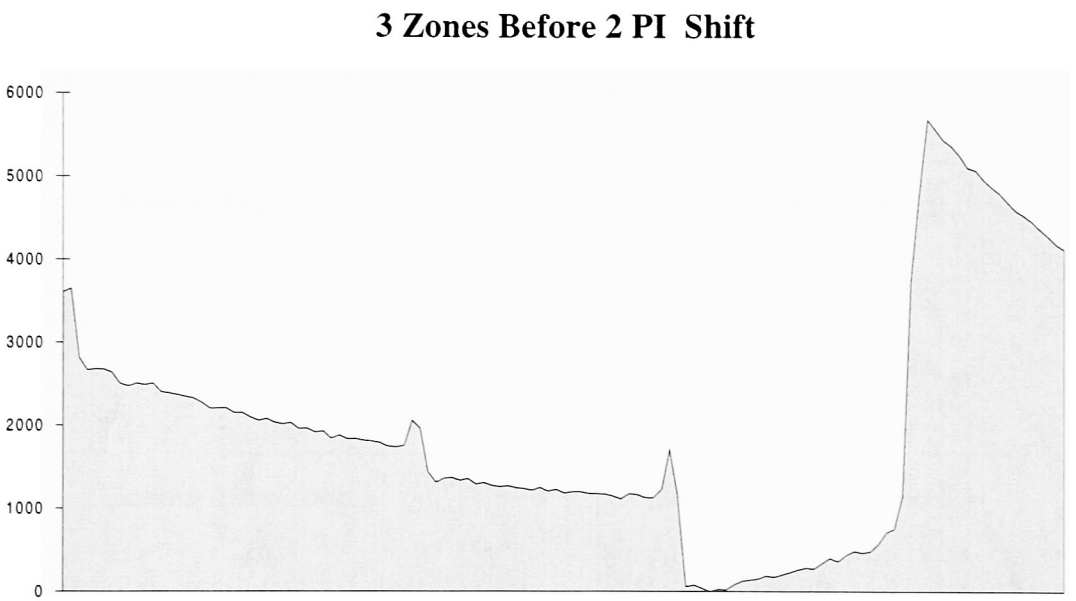

AFM cross section of microlens segment. Spikes at each step are the result of alignment errors.
Figure 5.5

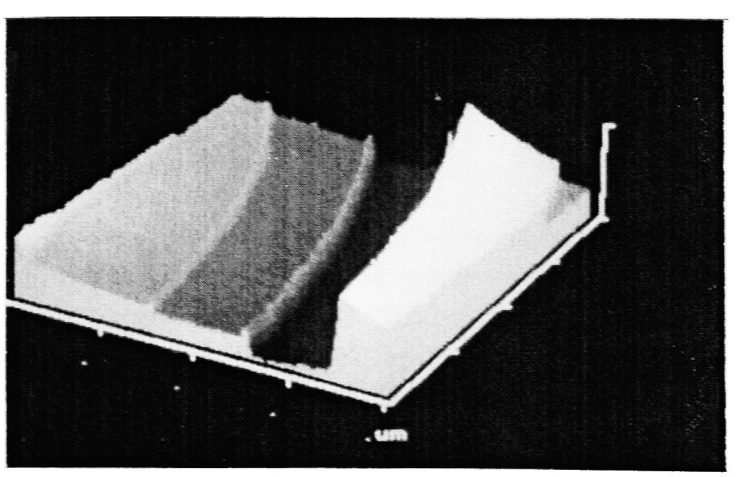

3D AFM image of lens segment shown in figure 5.5.
Figure 5.6

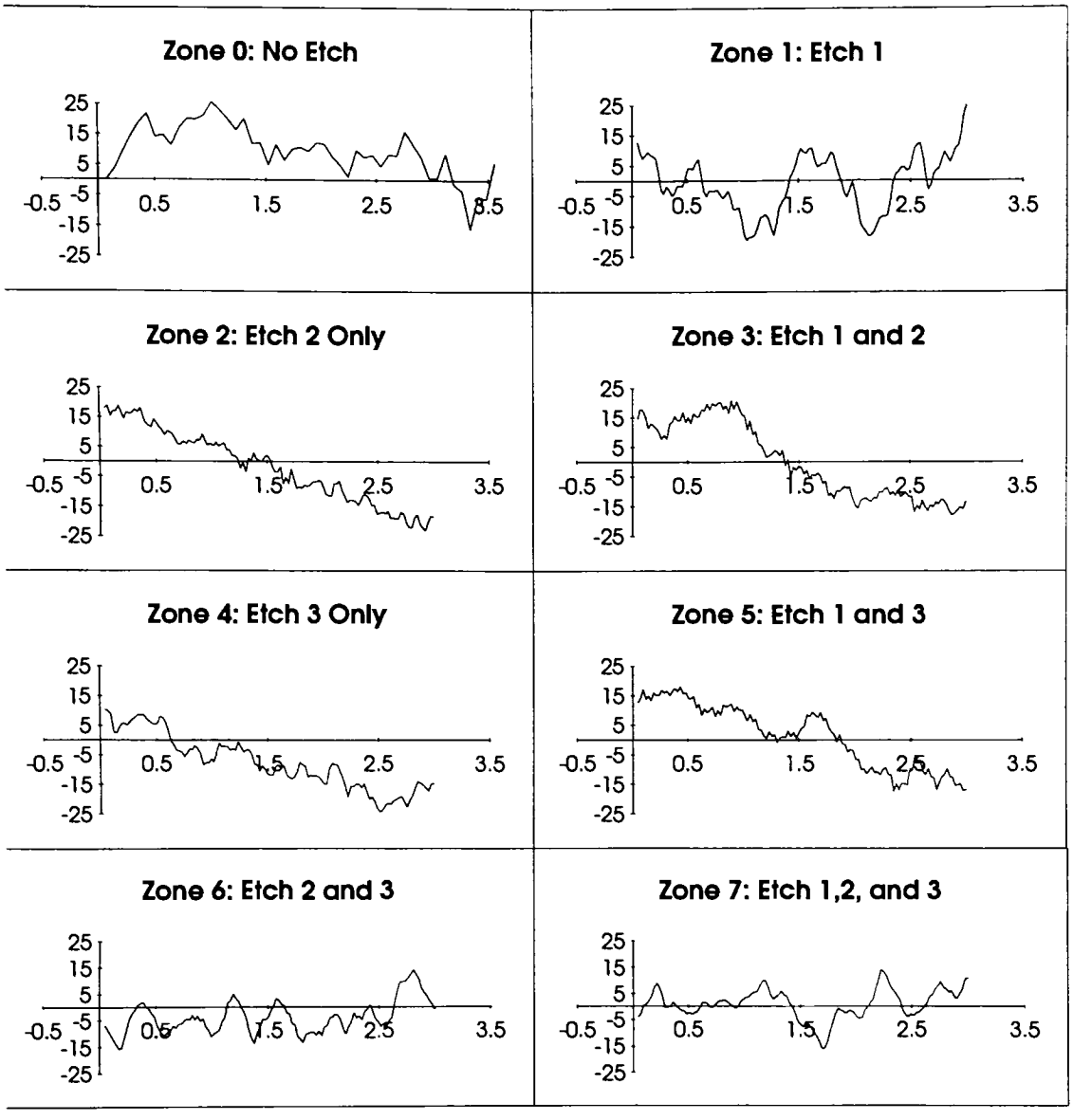

AFM scans of regions exposed to various etches for comparison of surface roughness.
Figure 5.7

Optical Performance results:

Initial verification of the phase shifting effect was based on the "chromeless" (phase only) features present on the test mask. Optical micrographs of the "dark field" phase gratings are shown in figures 5.8 and 5.9. The 0.5μm (figure 5.5 left) and 1.0μm (figure 5.8 right) gratings effectively produced "dark field" regions though some modulation was present in the 1.0μm region (resulting in a darker appearance). For gratings larger than 1.0μm such as the 2.5 and 3.0μm structures shown in figure 5.9, a dark region is formed only at the phase boundaries resulting in 0.6 μm resist lines that surround individual phase pixels.

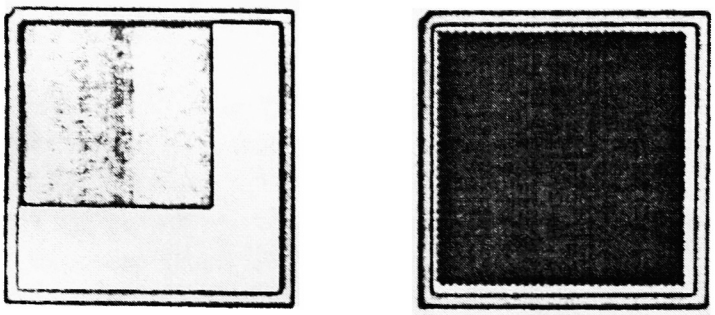

Dark field regions produced using 0.5 μm and 1.0 μm phase checkerboard patterns.
Figure 5.8

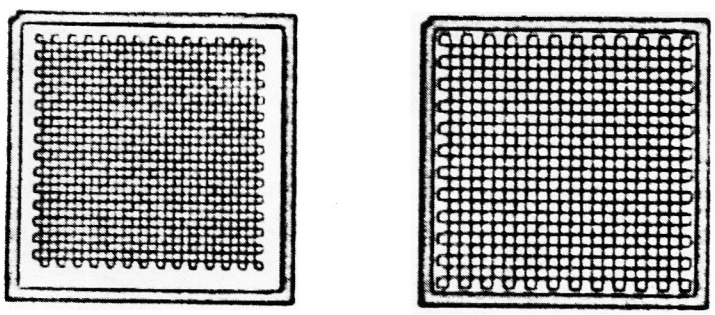

Dark "lines" exist only at phase boundaries of the 2.5 μm and 3.0 μm phase checkerboard patterns.
Figure 5.9

The structures shown in figure 5.10 are formed by the exposure of a π phase shift trench bounded on the top by a sloped phase transition. Ten different slopes are included on the mask. The steepest slope (0.5μm step size) in the upper left fails to eliminate the dark line formed at the upper phase edge. All subsequent transitions have successfully eliminated this transition producing phase trenches bounded on only three sides by resist lines.

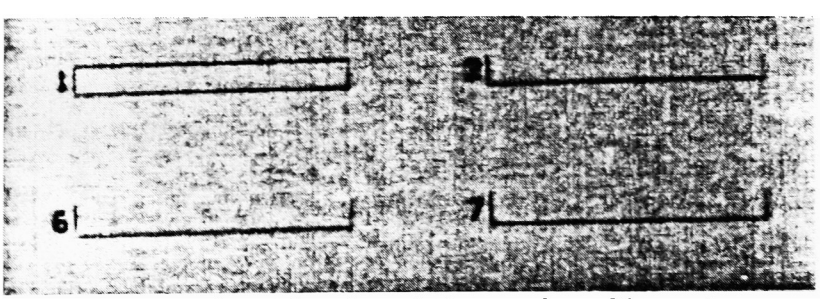

Elimination of printed phase edges through the use of a multi-step phase transition.
Figure 5.10

Electrical Linewidth Data:

Photoresist patterns on silicon wafers were transferred into a conductive polysilicon film via an RIE etch process. This enabled the measurement of both line and contact hole sizes. The results of the linewidth tests are plotted on pages 57 and 58. Exposures of 60, 80, and 100 mJ/cm2 are shown over a focus range of +/- 3 μm. Printing features over a range of focus and exposure values allows process latitude differences between phase shifted and standard masks to be evaluated. As expected, in all cases higher exposures produce smaller lines. Both phase shifted and standard techniques failed to image dense lines below 1.4 μm. For feature sizes at or above 1.4 μm there is almost no difference between phase shifted and non-phase shifted structures. This implies that surface roughness in etched regions does not significantly impact light intensity in these (larger) structures. Simulations (see figure 5.11) confirm that phase shifting fails to produce significant improvements for feature sizes above 1.4 μm at a wavelength of 436nm, partial coherence of 0.68, and a numerical aperture of 0.29. Only near the diffraction limit around 0.6 μm are significant benefits obtained.

Isolated lines for both standard and rim phase shift were resolved down to 0.6 μm. Rim phase shifting appeared to enhance the CD (critical dimension) control for features 1.0 μm and below. Fluctuations of linewidth through focus as well as the change with exposure were both reduced.

Similar data is shown for the contact structures on pages 59 and 60. The minimum contact size resolved for both phase shifted and non-phase shifted contacts was 0.8 μm. As expected, contacts biased 0.1 μm larger than standard sizes consistently resulted in 0.1 μm size differences in the electrical data adding confidence to the measurement technique. Serious problems were evident in the phase shifted structures. In all cases outrigger contacts measured significantly larger than the other contacts. Inspection of the wafer revealed that the outriggers themselves were on the verge of printing on the wafer. The intensity transmitted by these outriggers distorted the contacts causing the high readings. Rim shifted contacts typically measured smaller than their standard counterparts. An optical micrograph of a misaligned rim contact in Figure 5.12 explains this result. Rim shifted contacts are extremely alignment sensitive. Misalignments shift the 180/0 phase transition toward the center of the contact, significantly reducing the amount of light transmitted.

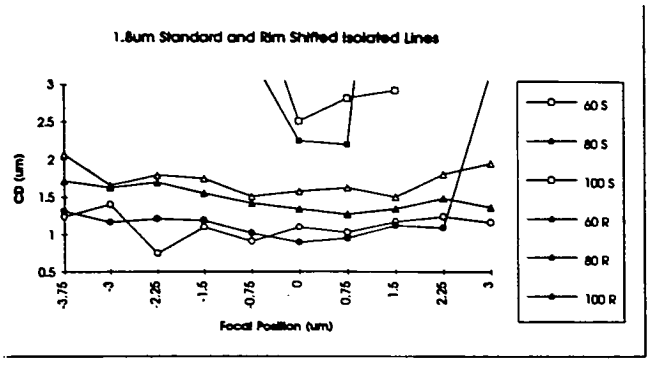
1.8um Standard and Rim Shifted Isolated Lines
CD (um)
Focal Position (um)
60 S
80 S
100 S
60 R
80 R
100 R

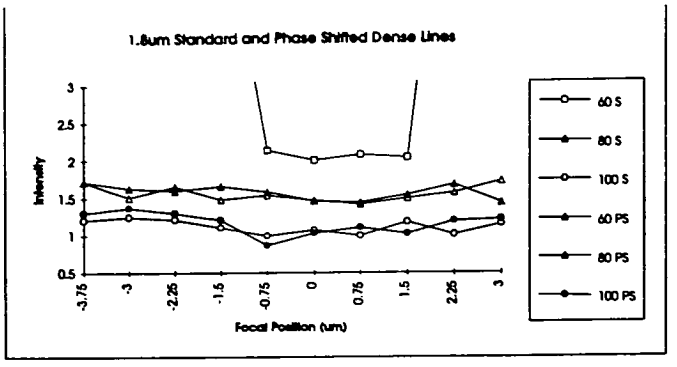
1.8um Standard and Phase Shifted Dense Lines
Intensity
Focal Position (um)
60 S
80 S
100 S
60 PS
80 PS
100 PS

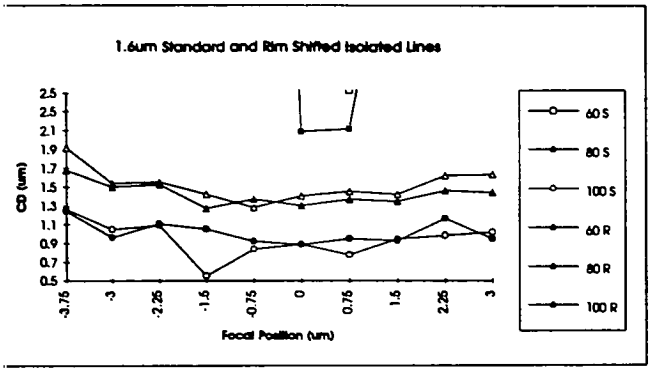
1.6um Standard and Rim Shifted Isolated Lines
CD (um)
Focal Position (um)
60 S
80 S
100 S
60 R
80 R
100 R

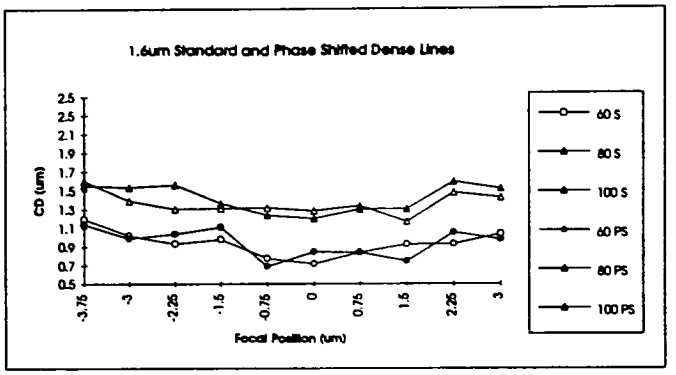
1.6um Standard and Phase Shifted Dense Lines
CD (um)
Focal Position (um)
60 S
80 S
100 S
60 PS
80 PS
100 PS

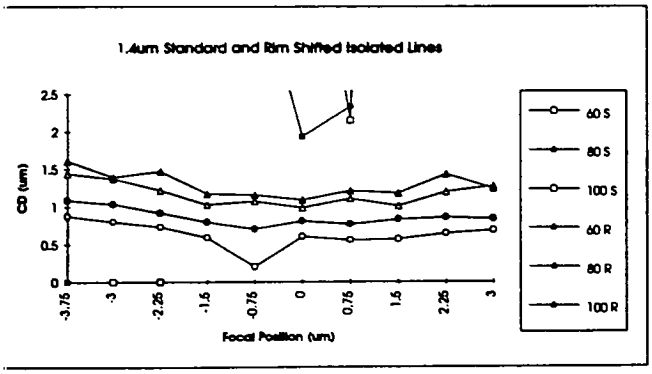
1.4um Standard and Rim Shifted Isolated Lines
CD (um)
Focal Position (um)
60 S
80 S
100 S
60 R
80 R
100 R

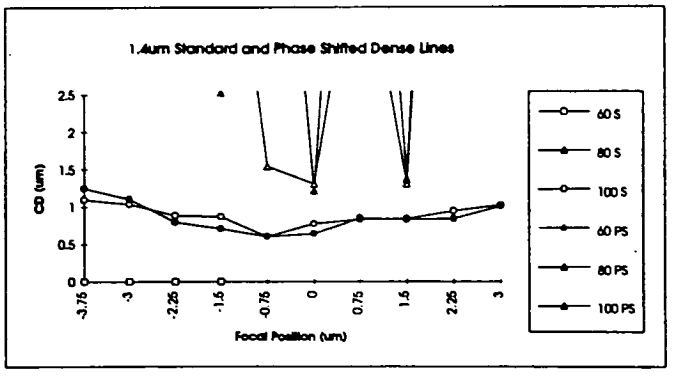
1.4um Standard and Phase Shifted Dense Lines
CD (um)
Focal Position (um)
60 S
80 S
100 S
60 PS
80 PS
100 PS

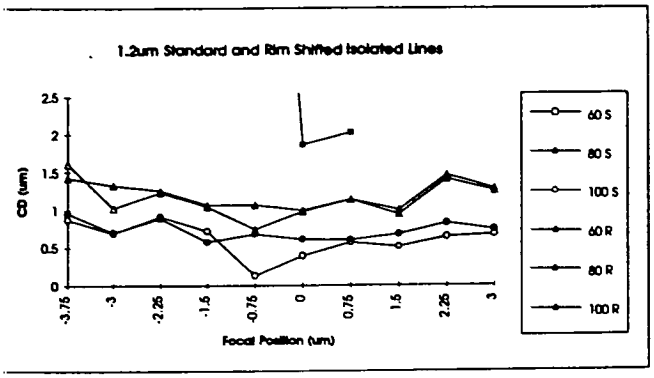
1.2um Standard and Rim Shifted Isolated Lines
CD (um)
Focal Position (um)
60 S
80 S
100 S
60 R
80 R
100 R

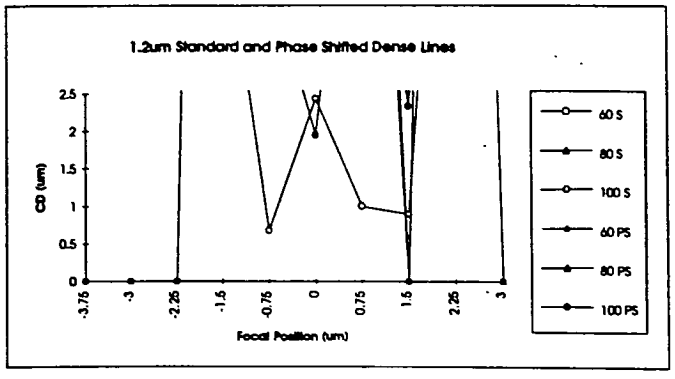
1.2um Standard and Phase Shifted Dense Lines
CD (um)
Focal Position (um)
60 S
80 S
100 S
60 PS
80 PS
100 PS

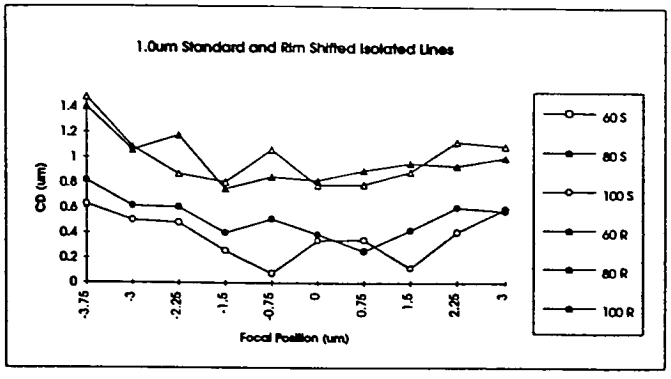
1.0um Standard and Rim Shifted Isolated Lines
CD (um)
Focal Position (um)
60 S
80 S
100 S
60 R
80 R
100 R

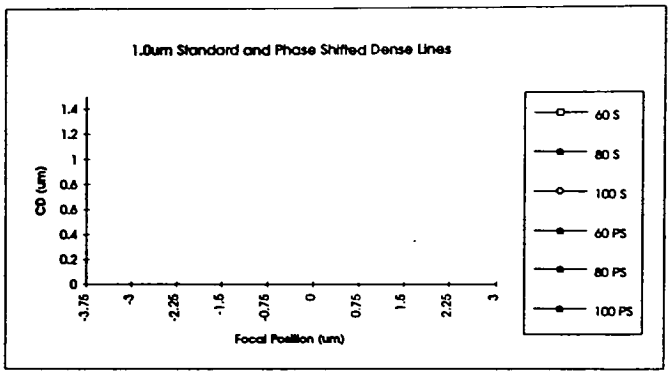
1.0um Standard and Phase Shifted Dense Lines
CD (um)
Focal Position (um)
60 S
80 S
100 S
60 PS
80 PS
100 PS

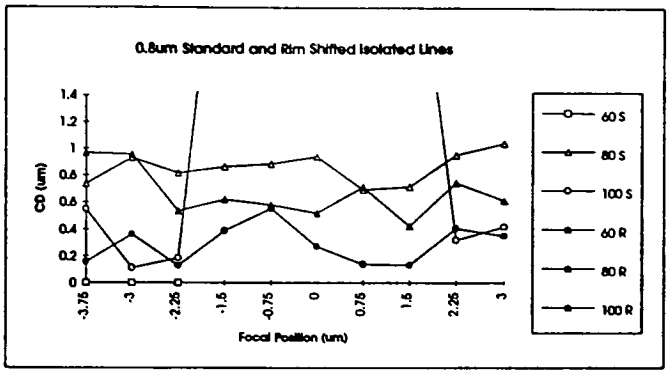
0.8um Standard and Rim Shifted Isolated Lines
CD (um)
Focal Position (um)
60 S
80 S
100 S
60 R
80 R
100 R

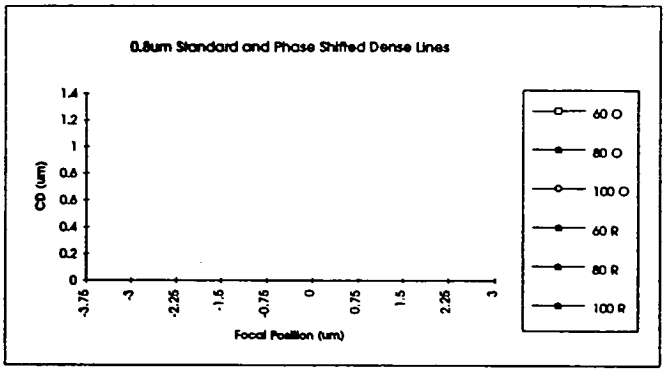
0.8um Standard and Phase Shifted Dense Lines
CD (um)
Focal Position (um)
60 O
80 O
100 O
60 R
80 R
100 R

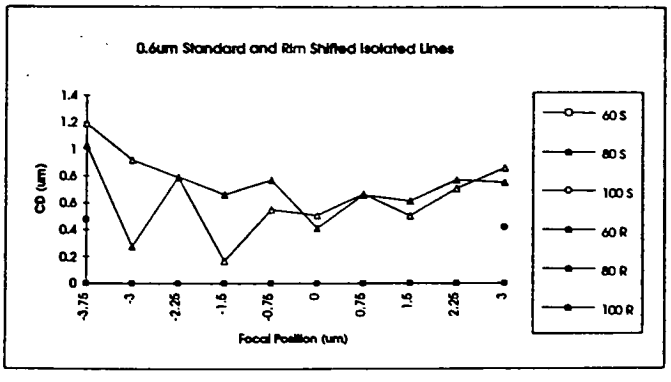
0.6um Standard and Rim Shifted Isolated Lines
CD (um)
Focal Position (um)
60 S
80 S
100 S
60 R
80 R
100 R

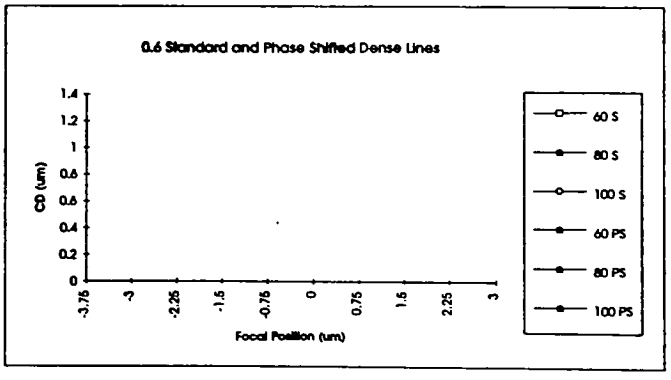
0.6 Standard and Phase Shifted Dense Lines
CD (um)
Focal Position (um)
60 S
80 S
100 S
60 PS
80 PS
100 PS

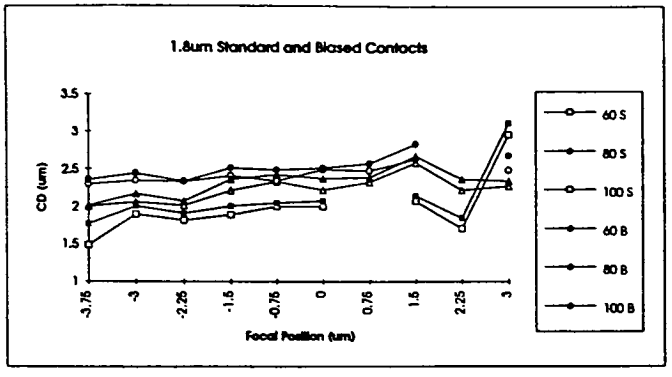
1.8um Standard and Biased Contacts
CD (um)
Focal Position (um)
60 S
80 S
100 S
60 B
80 B
100 B

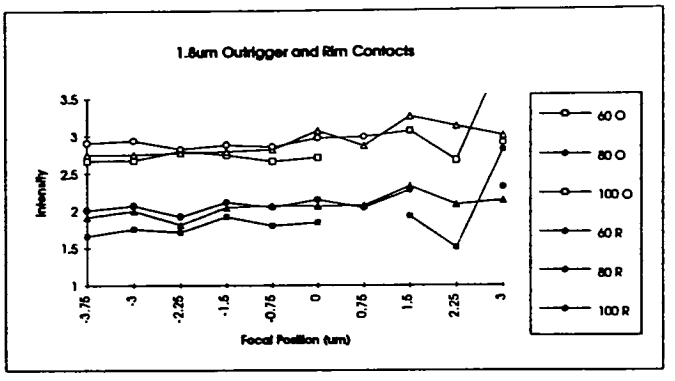
1.8um Outrigger and Rim Contacts
Intensity
Focal Position (um)
60 O
80 O
100 O
60 R
80 R
100 R

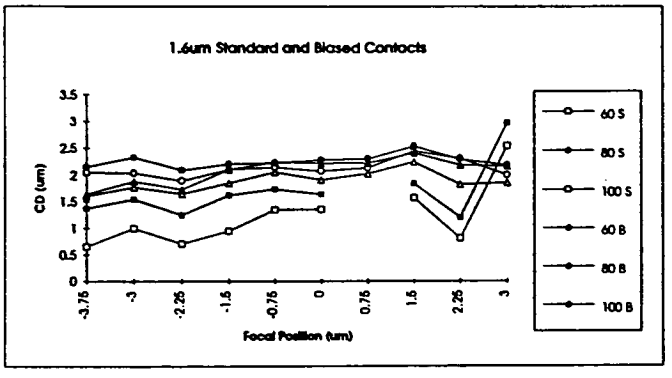
1.6um Standard and Biased Contacts
CD (um)
Focal Position (um)
60 S
80 S
100 S
60 B
80 B
100 B

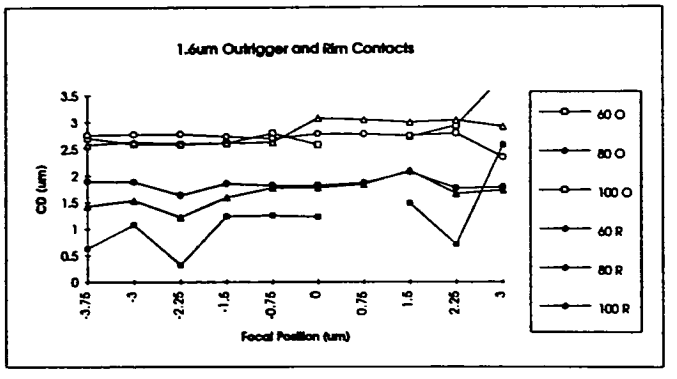
1.6um Outrigger and Rim Contacts
CD (um)
Focal Position (um)
60 O
80 O
100 O
60 R
80 R
100 R

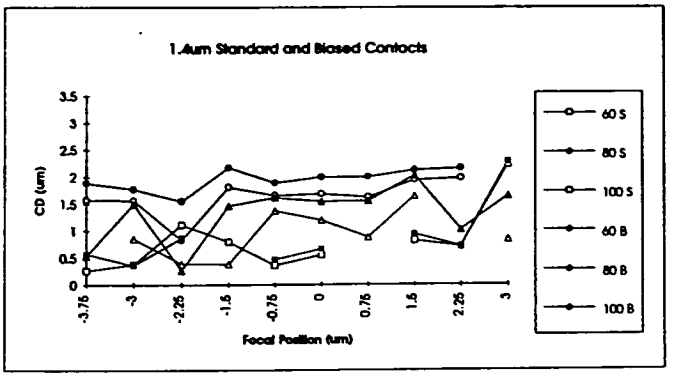
1.4um Standard and Biased Contacts
CD (um)
Focal Position (um)
60 S
80 S
100 S
60 B
80 B
100 B

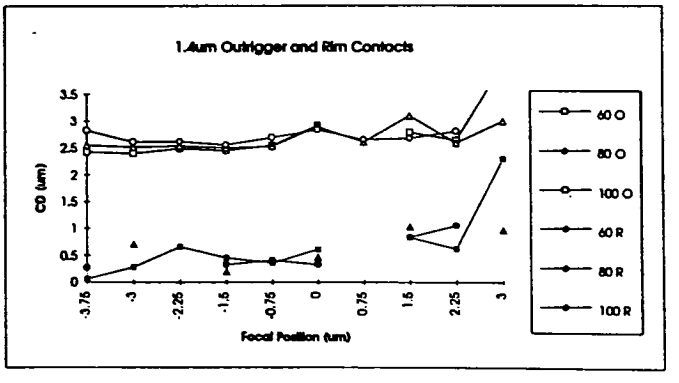
1.4um Outrigger and Rim Contacts
CD (um)
Focal Position (um)
60 O
80 O
100 O
60 R
80 R
100 R

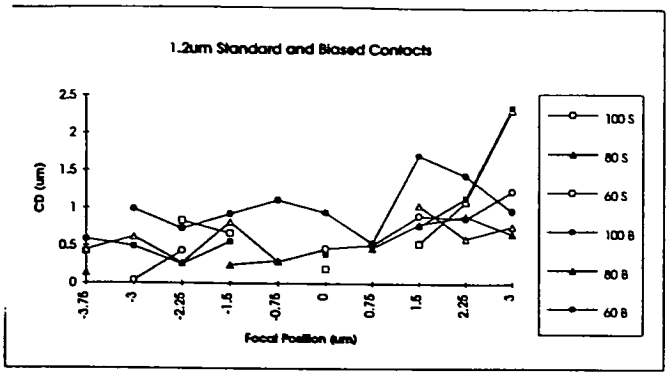
1.2um Standard and Biased Contacts
CD (um)
Focal Position (um)
100 S
80 S
60 S
100 B
80 B
60 B

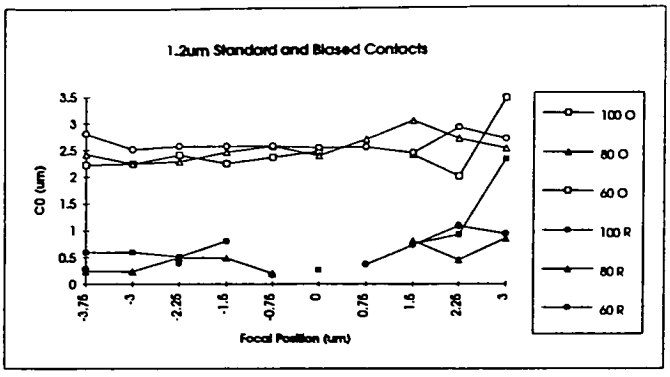
1.2um Standard and Biased Contacts
CD (um)
Focal Position (um)
100 O
80 O
60 O
100 R
80 R
60 R

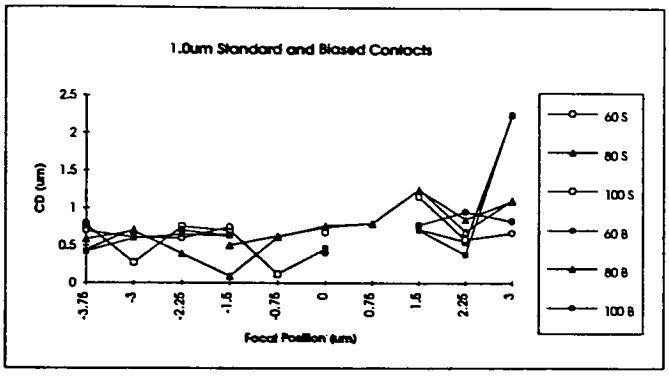
1.0um Standard and Biased Contacts
CD (um)
Focal Position (um)
60 S
80 S
100 S
60 B
80 B
100 B

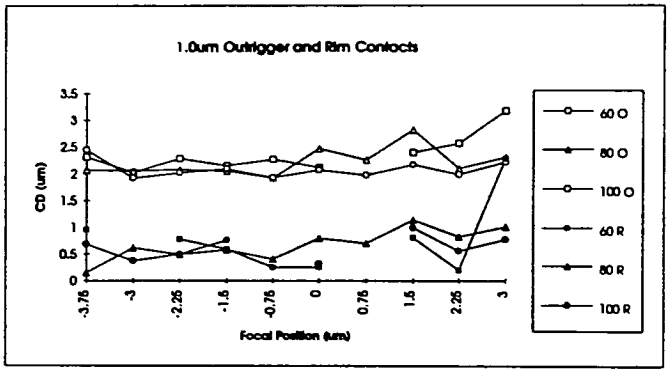
1.0um Outrigger and Rim Contacts
CD (um)
Focal Position (um)
60 O
80 O
100 O
60 R
80 R
100 R

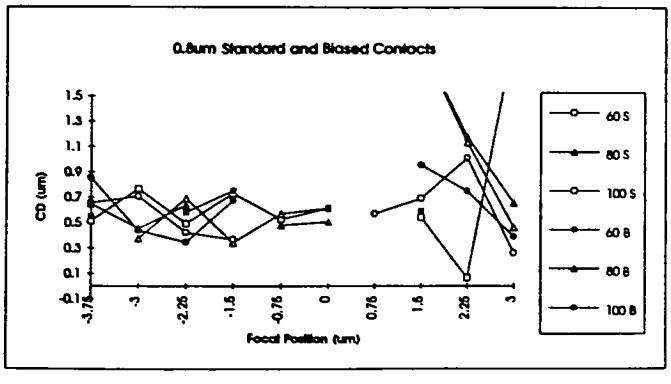
0.8um Standard and Biased Contacts
CD (um)
Focal Position (um)
60 S
80 S
100 S
60 B
80 B
100 B

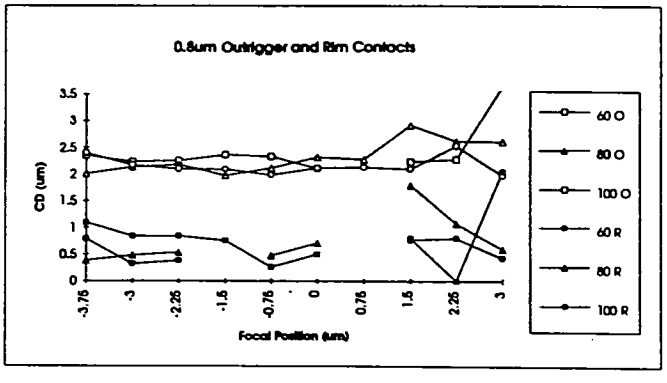
0.8um Outrigger and Rim Contacts
CD (um)
Focal Position (um)
60 O
80 O
100 O
60 R
80 R
100 R

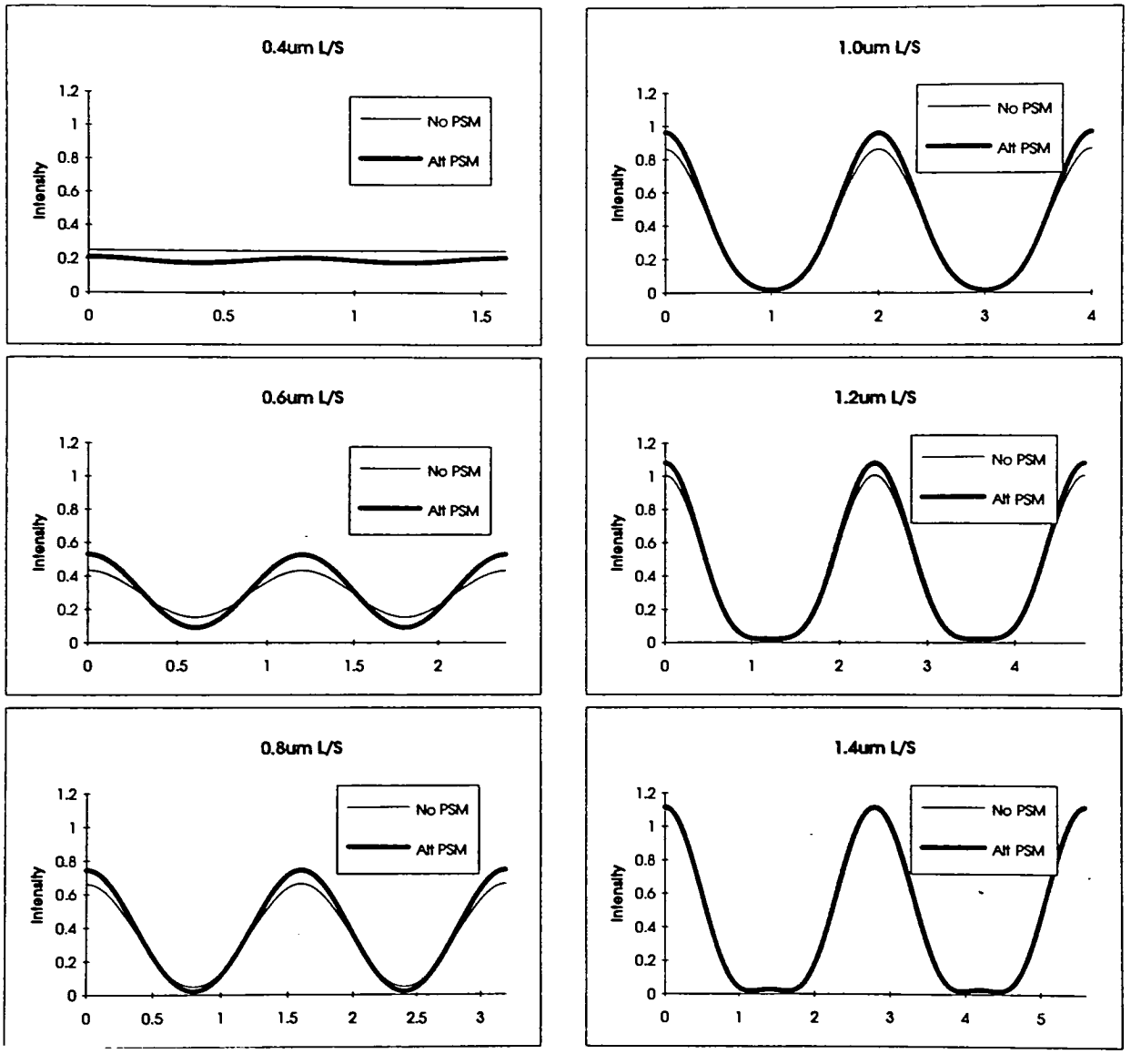

Figure 5.11

1DSIM results showing expected improvements using an alternating phase-shift mask.

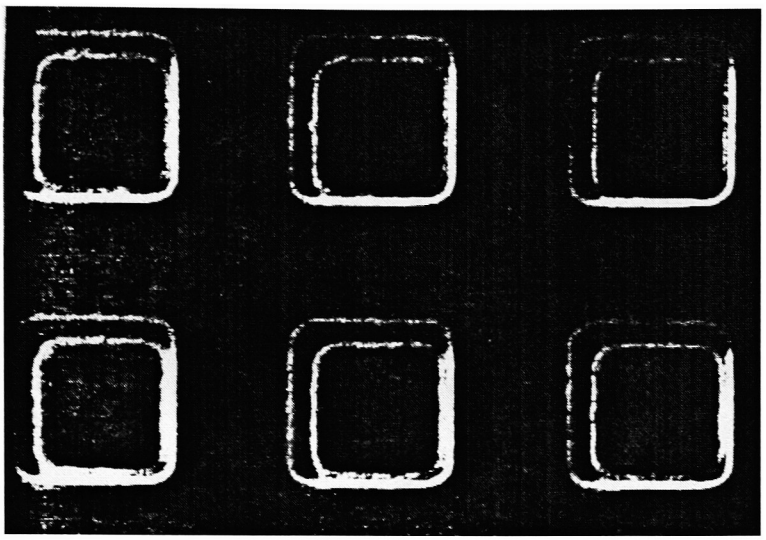

Misaligned Rim Phase Shifted Contacts

Figure 5.12

Microlens Results:

An electron micrograph of a fused silica microlens is shown in figure 5.13. The operation of these lenses were verified visually and with the use of a Spiricon LBA-100 laser beam analyzer with a Pulnix UV CCD camera. Beam profiler data for an array of four 35mm focal length contacts is presented for a range of focus positions in figure 5.14. Focal positions of 45 and 30mm were measured for the 35 and 25mm focal length lenses. This discrepancy was likely due to a combination of factors including etch and measurement errors, and lens aberrations. The low light intensity gathered by the 5 and 15mm lenses prevented the collection of reliable data from these structures.

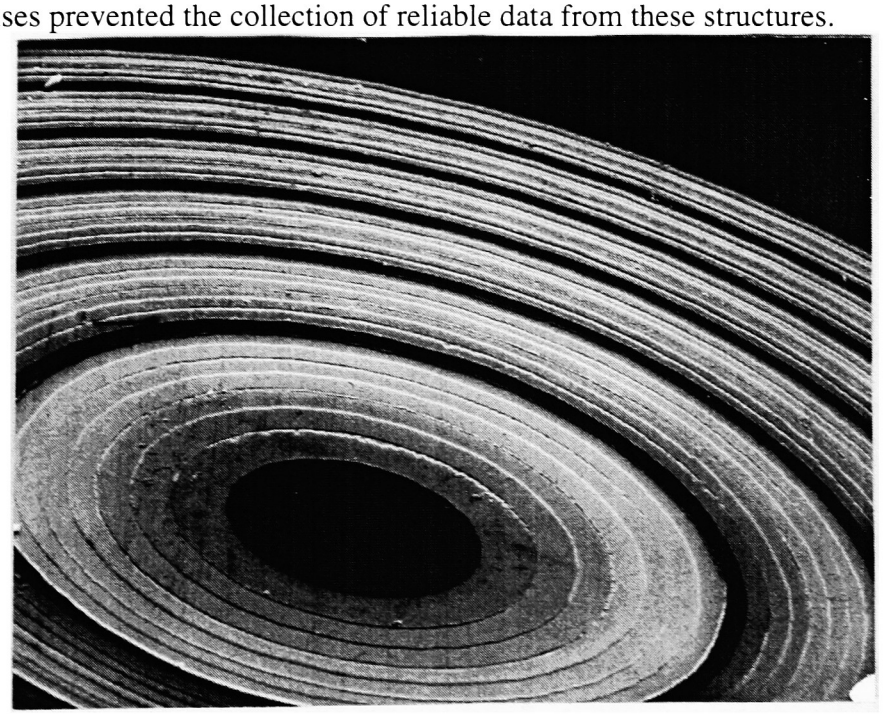

SEM micrograph of a microlens fabricated using binary optic approach.

Figure 5.13

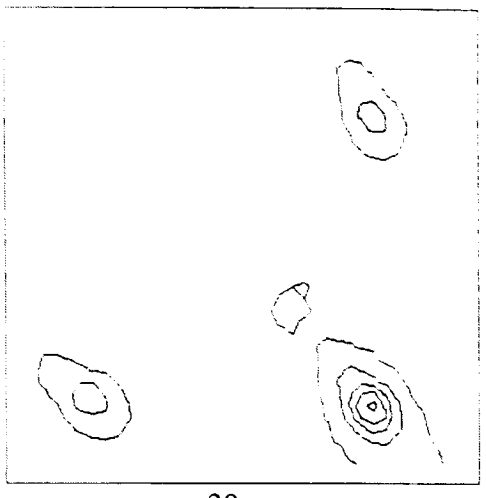

30mm

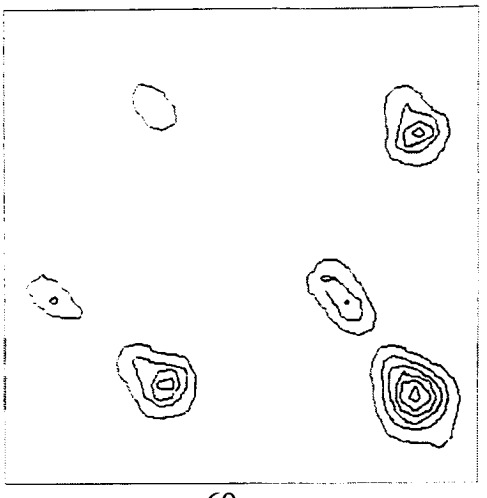

60mm

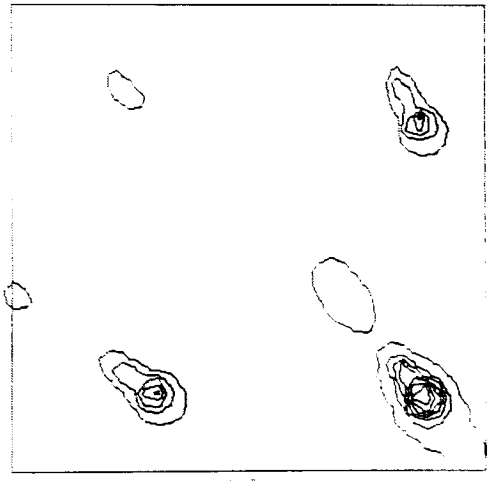

40mm

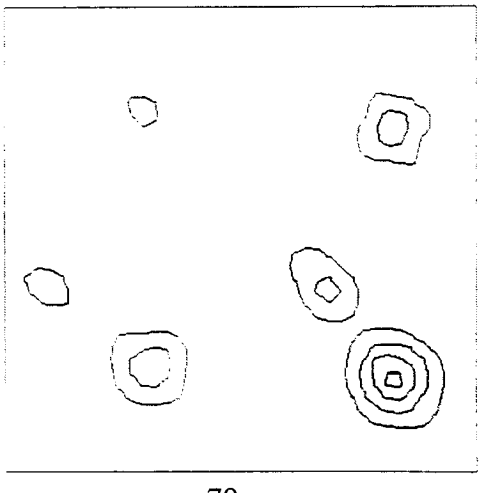

70mm

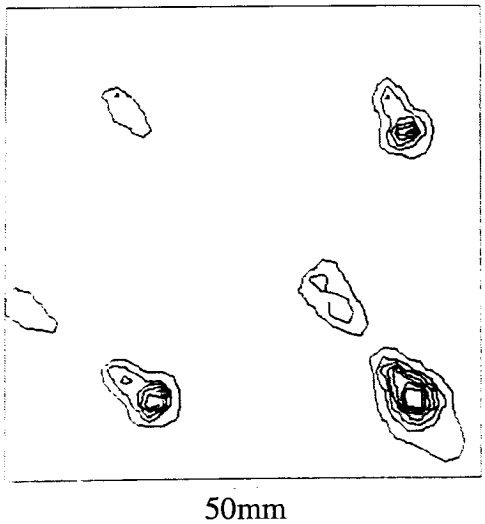

50mm

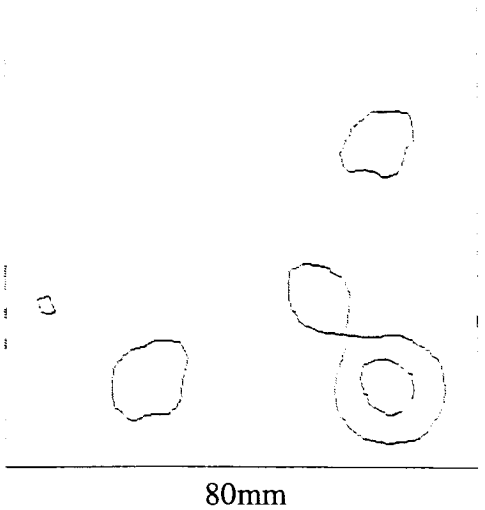

80mm

Beam profile data for 35mm focal length array. Positions shown repesent distance from the mask plane.Closely spaced contour lines indicate highest intensities. Maximum intensity occurs at about 45mm rather than the 35mm design value.

Figure 5.14

Conclusions/Summary

A new process for the fabrication of binary optics was established and tested. A sacrificial aluminum layer was used to provide both a conductive substrate for electron beam exposure, and a clean highly resistant etch stop for reactive ion etching. This enabled the use of a low pressure CF_4 RIE process that minimized the rates of polymerization during etch and provided stable etch rates necessary to achieve 100 angstrom etch depth control. Alignment errors of up to 1 micron were attributed to stage drifts on the electron beam exposure system. No systematic errors were found to indicate problems with the MEBES alignment system and alignment mark detection.

Simulations of multiphase PSMs were performed using a program developed as a part of this work capable of simulating a 1024 pixel array of arbitrary magnitude and phase under conditions of partially coherent illumination. Cases of annular (off-axis) illumination and defocus are also allowed. The program has demonstrated rapid calculation as well as flexibility of user input using a graphical user interface.

A three-etch, 8-phase level binary optic process was used to produce phase shifting masks and a quartz microlens array. Submicron "chromeless" phase mask features were demonstrated and gradient phase transitions were successfully used to eliminate unwanted lines at phase boundaries. Although photoresist process limitations prevented the realization of significant benefits from phase shifting, the electrical metrology structures demonstrated the ability to rapidly gather CD data useful in identifying problem areas.

Appendix I

Extended Source Model

An alternative approach for the calculation of partially coherent images described by Yeung involves the approximation of an extended incoherent source with an array of mutually incoherent point-source elements. Though the same assumption is implicit in Hopkin's mutual coherence function, the extended source algorithm used treats the source as a finite number of independent elements, rather than using the numerical integration employed by Hopkins. The image intensity distribution $I_i(x,y)$ due to each source element is calculated by assuming that each element acts as a point source providing coherent illumination at the object plane. The intensity calculation is straightforward since a coherently illuminated optical system can treated as linear in complex amplitude. Furthermore, since the elements are mutually incoherent, the total intensity at the image plane is simply the sum of intensities due to each source element $[\Sigma I_i(x,y)]$.

The image intensity distribution resulting from coherent illumination is given by the 2-D application of equation (21).

$$I(x,y) = \left| \iint f(x,y)k(x-x',y-y')dx'dy \right|^2 \tag{35}$$

The integral represents the 2-D convolution of the object function f(x,y) with the coherent transfer function k(x,y). In this simple representation, the object is illuminated by a plane wave normal to the optic axis. When this wave of unit magnitude and constant phase is multiplied by the object function f(x,y), the resulting disturbance is simply f(x,y). The result is more interesting when an off axis source point is considered. Rather than illuminating the object plane with a wave of constant phase, a linear phase is introduced as the plane wave is no longer normal to the optic axis. (See figure 10)

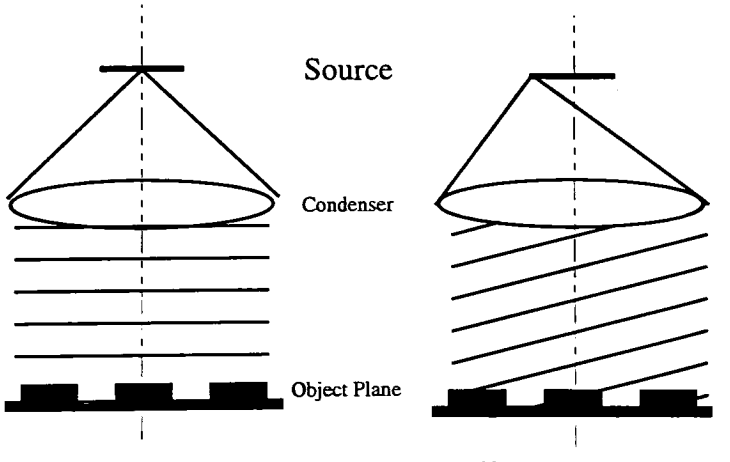

Figure 10

The wavefront at the object plane is no longer simply the complex transmission of the object f(x,y), but rather f(x,y) multiplied by some linear phase of the form $e^{i(2\pi/\lambda)(px+qy)}$. A

more general form of equation (35) includes the direction of propagation of the illumination:

$$I(x,y)=\left|\iint f(x,y)e^{i(2\pi/\lambda)(px'+qy')}k(x-x',y-y')dx'dy\right|^2 \tag{36}$$

where p and q are the x' and y' components of the direction of propagation. This exponential term goes to unity for the on-axis case. Note that a linear phase in the space domain corresponds to a translation in frequency space. These "shifts" are equivalent to the offsets used in the convolution described in Kintner's work in the previous section. The intensity distribution I(x,y) from an extended source can now be calculated by summing over source elements:

$$I(x,y)=\sum_{i=1}^{n}|A_i|^2\left|\iint f(x,y)e^{i(2\pi/\lambda)(p_ix'+q_iy')}k(x-x',y-y')dx'dy\right|^2 \tag{37}$$

where n is the number of source elements and A_i is the magnitude of the i-th source element. A_i is usually assumed to be unity for all i so the term $|A_i|^2$ is often replaced with 1/n to normalize the intensity.

The open questions remaining concern how many source points should be evaluated, and how they should be distributed across the source. It is reasonable to assume that the more source points considered, the better the agreement with Hopkin's numerical approach. Typically a uniform x,y grid of points is chosen over the condenser aperture shape. The literature has not been explicit as to the actual number of source points considered, but it is generally less than one hundred.

This description of the imaging properties of off axis source points will now be used to further study the resolution of coherent and incoherent systems. Consider a coherent (point) source illuminating the object plane of an optical system. Assume for simplicity that the distances are such that the spherical waves produced by diffraction in the object plane can be considered to be plane waves in the image plane. It is easily shown that two interfering plane waves will produce a periodic variation in intensity on a plane perpendicular to their direction of propagation. In fact, the period (P) of these variations is directly related to the angle (α) between the two waves by the following formula:

$$P=\frac{\lambda}{2\sin(\alpha/2)} \tag{38}$$

where λ is the wavelength. In an optical system, the angle (α) is limited by the aperture of the objective. The minimum period of modulation can therefore be represented by substituting the numerical aperture for sin(a/2) yielding,

$$P_{\min}=\frac{\lambda}{2NA_o}. \tag{39}$$

Therefore, the maximum spatial frequency of the intensity modulation generated by two-beam interference in an optical system is equal to $2NA/\lambda$. This corresponds to the maximum spatial frequency in the incoherent case in figures 5 and 6. The reason for this will become clearer in a moment.

Consider a binary transmission grating near the resolution limit of the system. In the case of on-axis coherent illumination, three diffracted orders (-1,0,+1) are collected by the objective. See Figure (11a). The 0th order supplies the DC bias, and the -1 and +1 orders represent wavefronts converging to some point in the image plane. In the case of off axis illumination, the addition of the linear phase on the object plane results in a shift of the diffracted orders in the pupil. This shift can cause an order to be lost as is shown with the +1 order in figure 11b. The result is a two-beam interference pattern in the image plane.

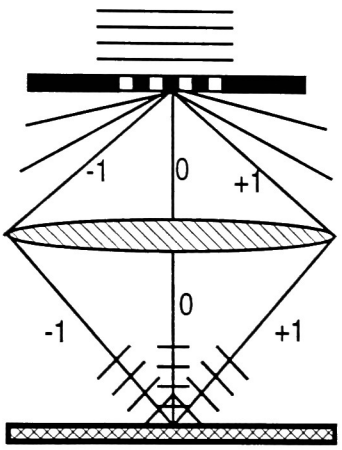

Figure 11a

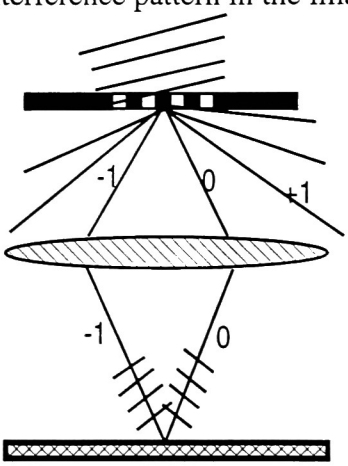

Figure 11b

In both cases (assuming the -1 and +1 orders of the on axis source point, and -1 and 0 orders of the off-axis source point enter the lens at the maximum angle) a sinusoidal variation in the electric field of frequency NA/λ will be produced. For the on-axis point, this cosine will be biased such that the field is always positive. The resulting intensity modulation equal to NA/λ. Off axis illumination as shown in fig. 11b results in an unbiased cosine. When the squared magnitude (intensity) is calculated, the resulting modulation in intensity has twice the frequency or 2NA/λ. For this reason the modulation transfer functions in figures 5 and 6 show (somewhat misleadingly) that incoherent illumination can produce twice the resolution as coherent.

Synthetic apertures have been used in lithographic systems to take advantage of these effects. Annular and quadrupole illuminators are designed to optimize specific spatial frequencies by producing a situation similar to that depicted in figure 11b.

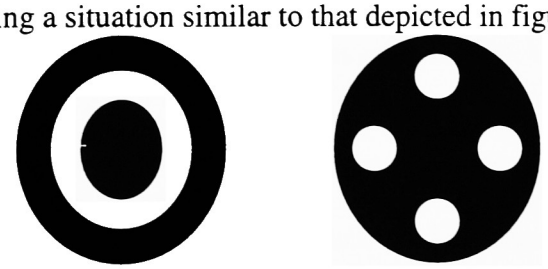
Annulus Quadrupole

Figure 12

Quadrupole illuminators are optimized for manhattan geometries where the diffracted orders are predominately in the x and y directions.

Appendix II

Reactive Ion Etching of Fused Silica

Reactive ion etching has become the preferred technique for the transfer of photoresist patterns into silicon oxides used in semiconductor fabrication. As a result, the process has been the subject of considerable research into the contributions and interactions of variables involved. The fundamental mechanism for etching silicon compounds in fluorine-based plasma involves three basic steps; the adsorption of fluorine ions to the silicon-containing surface, reaction of the fluorine with the silicon to form volatile products such as SiF_2 and SiF_4, and the deabsorption of the reaction products. Failure of any of these events to occur will halt the etching process.

A glow-discharge is a self-sustaining type of plasma (a partially ionized gas containing equal numbers of positive and negative charges)[18]. In an RF plasma system, a glow-discharge is formed when gas is released in vacuum chamber between the RF electrodes. The RF voltage (oscillating at 13.57MHz) causes the formation of energetic electrons that ionize the gas molecules. In this manner, chemically reactive species are formed from a relatively inert molecular gas. In a reactive ion etcher (RIE) a sample is placed on one of the electrodes and an additional DC bias applied. Ions created in the glow discharge are accelerated by this bias and bombard the surface to be etched. The result is a combination of chemical and physical (i.e. sputtering) etch processes that is more directional (anisotropic) than purely chemical systems. This directionality allows the formation of deep trenches with near vertical sidewalls desired for binary optics and phase shift mask applications.

The most common model used to describe the etching of silicon oxides is the fluorine-to-carbon ratio model (or F/C model)[19]. Typically fluorine is introduced into a plasma via a fluorocarbon molecule such as CF_4 (Freon 14) or CHF_3 (Freon 23). In general, the higher the concentration of fluorine at the surface, the faster the etch rate. Similarly, the higher the ratio of fluorine to carbon, the faster the etch will progress. Oxides would be expected to etch faster in CF_4, having a F/C ratio of 4, for example, than CHF_3 which has a F/C ratio < 4. The lower ratio is due both to the 3:1 F/C ratio in Freon 23 and the fact that hydrogen atoms will scavenge fluorine to form HF, thus further reducing the relative concentration of fluorine. If the sole goal of oxide etch processes was to rapidly etch oxide, the discussion would end here. In most applications (including the creation of phase steps), selectivity and side-wall angle are as critical as etch rate due to fluorine concentration.

Selectivity is simply the ratio of the etch rates of the material to be removed (oxide in this discussion), and either the etch mask or substrate material. If the etch mask (typically photoresist) is attacked by the etchant, linewidth control and sidewall angle (slope) will be degraded. (In extreme cases the entire etch mask can be removed obliterating the pattern being transferred). A low selectivity over the substrate material (usually silicon) could damage the surface and reduce device yields. A mechanism is required to minimize the etch rate of silicon and photoresist while maintaining the oxide etch process. The addition of hydrogen to a fluorine plasma has been shown to accomplish these tasks. It has been stated that hydrogen scavenges fluorine, thereby reducing the F/C ratio and decreasing the etch rates of both silicon and silicon dioxide. In areas where oxide is being

etched, oxygen is generated that combines to form CO and CO_2. The consumption of carbon locally increases the F/C ratio over the oxide causing an enhanced etch rate compared to that of bare silicon.

The addition of hydrogen also enhances the selectivity over photoresist. (Note hydrogen can be added in molecular form or directly incorporated in etch species such as CHF_3). In every fluorocarbon based plasma, carbon and fluorine ions will form inert compounds that are deposited on the substrate. The rate of this polymer formation is directly related to the F/C ratio of the plasma. The addition of hydrogen depletes the fluorine and forces the equilibrium toward increased carbon concentrations. These Teflon-like polymer residues are extremely inert, and are capable of stopping the etch if sufficient quantities are present. In areas where oxide is being etched, oxygen is present that consumes carbon and slows polymer formation. This is not the case over photoresist where the polymer film forms a protective layer that inhibits the removal of the resist. Optimum selectivities are achieved when the process is run near the boundary of polymerization and etch conditions. At this point, the small differences in the F/C ratio over oxide and the substrate or etch mask will cause significant changes in etch rate.

An equilibrium condition is reached in the oxide region where the rate of polymer removal exceeds the deposition rate. Polymer is removed via sputtering due to the ionic bombardment. The bombardment energy, and thus the rate of polymer removal, can be increased by increasing the bias voltage or lowering the pressure. At lower pressures, the distance traversed by ions without collisions with other molecules is increased allowing for greater acceleration to occur. For this reason lower pressures increase the rate of polymer removal.

In most semiconductor applications, precise etch rate control is not needed if sufficient selectivity can be achieved. Typically endpoint detectors are used to determine when the material to be etched has been removed, and etch times adjusted accordingly. In these circumstances the etch rate variations due to operation of the process near the polymerization/etch boundary are tolerable. Problems arise in applying these techniques to phase shift mask and binary optics applications. Since no substrate is present to act as an etch stop when the desired thickness has been removed, etch depths must be controlled by adjusting the etch time. Uniform etch rates are critical to the success of such a process.

The final aspect of the RIE oxide etch process to be discussed involves the mechanism for the creation of steep sidewalls. There are two distinct theories describing the directional nature of RIE processes. The first states that ionic bombardment disrupts the surface producing conditions favorable to the adsorption and reaction of fluorine. Since the vertical sidewalls of etch trenches do not receive this bombardment, etching proceeds faster at the bottom of the trench than the sides. The second theory involves the polymer deposition discussed previously. Polymer is deposited on all exposed surfaces during the etch. Horizontal surfaces are subject to ionic bombardment that removes the polymer via a sputtering process. The polymer residue on vertical sidewalls is shielded from this harassment and forms a protective film that limits etching in the horizontal direction.

In summary, high selectivity and etch rate control are often difficult to achieve simultaneously. Rates of polymer formation (which dramatically impact etch rates) are extremely sensitive to changes in process parameters such as pressure and gas flow, as well as environmental contamination such as residual water vapor. Increasing the rate of polymerization to improve selectivity correspondingly increases the influence of these

other variables on the etch rate. In a phase etch process, high selectivity to the etch mask is required while substrate selectivity is not an issue.

Appendix 3

1DSIM.C - Partially Coherent Aerial Image Simulator

```
/* The following global variables are defined:
/*      sigma       : partial coherence parameter
/*      defocus     : deviation from optimum focus
/*      na          : numerical aperature of the objective
/*      lambda      : average wavelength of quasimonochromatic source
/*      fieldsize   : size of field period (1/fieldsize defines sampling rate in freq space)
/*      kfield      : fieldsize in k space
/*      linewidth   : width of transparent part of grating
/*      tcc00=1     : initial value of the TCC(0,0)

#include <math.h>
#include <graphics.h>
#include <stdio.h>
#include <conio.h>
#include <alloc.h>
#include <stdlib.h>
#include <stdarg.h>
#include <dos.h>
#include <gprint.i>

#define PI 3.14159265359
#define MAXNUM 1024
#define NUMSEGMENTS 100
#define INPUT 0
#define OUTPUT 2
#define NO 0
#define YES 1
#define INNER 0
#define OUTER 1
#define FORWARD -1
#define REVERSE 1
#define NOTUSED 999

double tccreal,tccimag,defocus,sigma,fieldsize;
double kfield,p,tcc00=1;

struct xcomplex
{
  float real, imag;
};

/*                                                                          */
/*  The following two functions convert the array from real/imaginary format to magnitude   */
/*   /phase and visa versa                                                  */
/*                                                                          */

void real_imag(struct xcomplex *xarray)
{
   int i;
   float magnitude_temp,phase_temp;
```

```
    for(i=0;i<MAXNUM;i++)
    {
          magnitude_temp=xarray[i].real;
          phase_temp=xarray[i].imag;

          xarray[i].real=magnitude_temp*cos((double)(phase_temp));
          xarray[i].imag=magnitude_temp*sin((double)(phase_temp));
    }
}

void mag_phase(struct xcomplex *xarray)
{
  int i;
  float real_temp,imaginary_temp;

    for(i=0;i<MAXNUM;i++)
    {
          real_temp=xarray[i].real;
          imaginary_temp=xarray[i].imag;

          xarray[i].real=(float)(sqrt( (double)( (real_temp*real_temp) + (imaginary_temp*imaginary_temp)
) ));
          if(real_temp==0)
          { xarray[i].imag = 0; }
          else
          { xarray[i].imag=(float)(atan((double)(imaginary_temp/real_temp))); }
    }
}

/*                                                                    */
/*   The following function performs a 1-D fast fourier transform on a complex structure   */
/*                                                                    */

void fft(struct xcomplex *x,int m,int inv)
{
   static struct xcomplex *w;
   static int mstore=0;
   static int n=1;

   struct xcomplex u,temp,tm;
   struct xcomplex *xi,*xip,*xj,*wptr;

   int i,j,k,l,le,windex;

   float w_real,w_imag,wrecur_real,wrecur_imag,wtemp_real;
   double arg;

   if(mstore!=0) free(w);
   mstore=m;
   if(m==0) return;

   n=1<<m;
   le=n/2;

   w=(struct xcomplex *)calloc(le-1,sizeof(struct xcomplex));
```

```
if(!w)
{
  printf("\nUnable to allocate xcomplex W array \n");
  exit(1);
}

arg = 4.0*atan(1.0)/(double)(le);
wrecur_real = w_real = (float)(cos(arg));
wrecur_imag = w_imag = (float)(inv*sin(arg));
xj=w;
for(j=1;j<le;j++)
{
  xj->real = wrecur_real;
  xj->imag = wrecur_imag;
  xj++;
  wtemp_real = wrecur_real*w_real - wrecur_imag*w_imag;
  wrecur_imag = wrecur_real*w_imag + wrecur_imag*w_real;
  wrecur_real = wtemp_real;
}


/* start fft */

le = n;
windex=1;
for(l=0;l<m;l++)
{
  le = le/2;
  for(i=0;i<n;i=i+2*le)
  {
        xi=x+i;
        xip=xi+le;
        temp.real = xi->real + xip->real;
        temp.imag = xi->imag + xip->imag;
        xip->real = xi->real - xip->real;
        xip->imag = xi->imag - xip->imag;
        *xi = temp;
  }
  wptr = w + windex -1;
  for (j=1;j<le;j++)
  {
        u = *wptr;
        for(i=j;i<n;i=i+2*le)
        {
          xi=x+i;
          xip=xi+le;
          temp.real = xi->real + xip->real;
          temp.imag = xi->imag + xip->imag;
          tm.real = xi->real - xip->real;
          tm.imag = xi->imag - xip->imag;
          xip->real= tm.real*u.real - tm.imag*u.imag;
          xip->imag= tm.real*u.imag + tm.imag*u.real;
          *xi=temp;
        }
        wptr = wptr + windex;
```

```
    }
    windex = 2*windex;
  }
  j=0;
  for(i=1;i<(n-1);i++)
  {
    k=n/2;
    while(k<=j)
    {
        j=j-k;
        k=k/2;
    }
    j=j+k;
    if(i<j)
    {
        xi = x + i;
        xj = x + j;
        temp = *xj;
        *xj = *xi;
        *xi = temp;
    }
  }
  if(inv==FORWARD) /* scale forward transform by 1/N */
  {
    for(i=0;i<n;i++)
    {
        xi=x+i;
        xi->real=(xi->real/MAXNUM);
        xi->imag=(xi->imag/MAXNUM);
    }
  }
}

/*                                                                          */
/*  This function returns the area of intersection of two circles of radii r1 and r2 separated by  */
/*  a distance (dist)                                                       */
/*                                                                          */

double Area(double r1,double r2,double dist)
{
  double theta1,theta2,c,intersectarea;

  if(dist==0)
  {
    if(r1>=r2) intersectarea=PI*r2*r2;
    if(r2>r1) intersectarea=PI*r1*r1;
  }
  else
  {
    theta1=acos( ( (dist*dist) + (r1*r1) - (r2*r2) ) / ( 2*dist*r1) );
    theta2=acos( ( (dist*dist) + (r2*r2) - (r1*r1) ) / ( 2*dist*r2) );

    c=r1*sin(theta1);

    intersectarea=( (r1*r1*theta1) + (r2*r2*theta2) ) - (c*dist);
```

```
  }
  return(intersectarea);
}

/*                                                                    */
/*   The overlap_type routine is called by TCC to determine the type of overlap of the pupil   */
/*   functions with the condenser function given the pupil function shifts fx1 and fx2        */
/*                                                                    */

int overlap_type(double fx1,double fx2)
{
  double fxmax,fxmin;

  fxmax=fx2+1;
  fxmin=fx1-1;

  /* Test 1 ----- Coherent Source */

  if(sigma<0.01) return(10);

  /* Test 2 ----- Do K and K* intersect */

  if( (fx1-fx2)>2 ) return(1);

  /* Test 3 ----- Does Source intersect overlap region */

  if( !((fxmin<=sigma)&&(fxmax>=(-1*sigma))) ) return(1);

  /* Test 4 ----- Is source smaller than the unit pupil */

  if( (sigma<1) )
  {
    /* Test 7 */
    if( (fxmin>(-1*sigma)) && (fxmax<sigma) )  /* then Test 9 */
    {
          if( ((fx1*fx2)+1) <= (sigma*sigma) )
          {
            return(9);
          }
          else
          {
            return(8);
          }
    }
    if( fxmin>(-1*sigma))
    {
          return(6);
    }
    if( (fxmax<sigma))
    {
          return(7);
    }
    return(5);
  }
  else
```

```
  {
    if( (sigma>=fxmax) && ( (-1*sigma)<=fxmin) )    /* Test 5 */
    {
          return(2);
    }
    else  /*Test 6 */
    {
          if( (sigma*sigma) >= ((fx1*fx2) +1) )
          {
            return(3);
          }
          else
          {
            return(4);
          }
    }
  }
}

/*                                                                              */
/*   The following routine performs a numerical integration to evaluate the TCC under conditions */
/*   of defocus. Again several paths can be taken depending upon the nature of the overlap */
/*                                                                              */


void Integrate_Tcc(double f1,double f2,double f_limit[],double g_limit[],int overlap)
{
  int special=NO,do_extra_loop=NO;
  double g,c1,c2,c3,gstep,rtcc,itcc,g0real,g0imag,o1,o2,gmax,r1,r2,swap=NOTUSED;

  double const_real,const_imag;

  if((overlap==5)||(overlap==8))
  { gmax=sigma; }
  else
  { gmax=g_limit[0]; }
  if(overlap==8)
  {
    if(g_limit[1]>g_limit[0]) { gmax=g_limit[1]; }
    else { swap=g_limit[0]; g_limit[0]=g_limit[1]; g_limit[1]=swap; }
    if( (f_limit[0]<0)&&(f_limit[1]>0) ) gmax=sigma;
  }
  if((overlap==7)&&(f_limit[0]>0)) { special=YES; gmax=sigma; }
  if((overlap==6)&&(f_limit[0]<0)) { special=YES; gmax=sigma; }
  gstep=gmax/NUMSEGMENTS;

  c1=-1*PI*defocus/2;
  c2=c1*( (f2*f2)-(f1*f1) );
  c3=2*c1*(f1-f2);
  if(c3==0)
  {
    const_real=1;
    const_imag=1;
  }
  else
```

```
{
  const_real=sin(c2)/c3;
  const_imag=-1*cos(c2)/c3;
}
rtcc=0; itcc=0;

if((overlap==8)||(overlap==9)) { r1=r2=1; o1=f2; o2=f1; }
if(overlap==7) { r1=1; r2=sigma; o1=f2; o2=0;}
if(overlap==6) { r1=sigma; r2=1; o1=0; o2=f1;}
if(overlap==5) { r1=sigma; r2=sigma; o1=0; o2=0; }

for(g=gstep;g<g_limit[0];g=g+gstep)
{
  rtcc=rtcc+(cos(c3*(sqrt((r1*r1)-(g*g))+o1))*gstep)-(cos(c3*(( -1*sqrt((r2*r2)-(g*g)) ) +o2))*gstep);
  itcc=itcc+(sin(c3*(sqrt((r1*r1)-(g*g))+o1))*gstep)-(sin(c3*(( -1*sqrt((r2*r2)-(g*g)) ) +o2))*gstep);
}
  g0real=(cos(c3*(sqrt(r1*r1)+o1))*gstep)-(cos(c3*(( -1*sqrt(r2*r2) ) +o2))*gstep);
  g0imag=(sin(c3*(sqrt(r1*r1)+o1))*gstep)-(sin(c3*(( -1*sqrt(r2*r2) ) +o2))*gstep);

if((overlap==8)||(special==YES))
{
  if( special==YES ) { r1=r2=sigma; o1=o2=0; }
  else
  { /* overlap==8 */
      if( (f_limit[0]<0)&&(f_limit[1]<0) ) { r1=1; r2=sigma; o1=f2; o2=0;}
      if( (f_limit[0]>0)&&(f_limit[1]>0) ) { r1=sigma; r2=1; o1=0; o2=f1;}
      if( (f_limit[0]<0)&&(f_limit[1]>0) )
      {
        if( swap==NOTUSED /* g_limit[0]<g_limit[1] */ )
          { do_extra_loop=YES; r1=1; r2=sigma; o1=f2; o2=0;}
          else
          { do_extra_loop=YES; r1=sigma; r2=1; o1=0; o2=f1;}
      if( f_limit[0]==(-1*f_limit[1]) )
        { do_extra_loop=NO; r1=r2=sigma; o1=o2=0; g_limit[1]=sigma;}
      }

  }
  for(g=g;g<g_limit[1];g=g+gstep)
  {
      rtcc=rtcc+(cos(c3*(sqrt((r1*r1)-(g*g))+o1))*gstep)-(cos(c3*(( -1*sqrt((r2*r2)-(g*g)) )
+o2))*gstep);
      itcc=itcc+(sin(c3*(sqrt((r1*r1)-(g*g))+o1))*gstep)-(sin(c3*(( -1*sqrt((r2*r2)-(g*g)) )
+o2))*gstep);
  }
  if(do_extra_loop==YES)
  {
      for(g=g;g<sigma;g=g+gstep)
      {
        rtcc=rtcc+(cos(c3*sqrt((sigma*sigma)-(g*g)))*gstep)-(cos(-1*c3*sqrt((sigma*sigma)-
(g*g)))*gstep);
        itcc=itcc+(sin(c3*sqrt((sigma*sigma)-(g*g)))*gstep)-(sin(-1*c3*sqrt((sigma*sigma)-
(g*g)))*gstep);
      }
  }
}
```

```
  rtcc=(rtcc*2)+g0real; itcc=(itcc*2)+g0imag;
  tccreal=(rtcc*const_real)-(itcc*const_imag);
  tccimag=(itcc*const_real)+(rtcc*const_imag);
}

/*                                                                          */
/*  TCC is the main function that controls calculation of the TCC. The coordinates of the pupil  */
/*  function and its conjugate are transferred to the routine, and the overlap_type function called. */
/*  Depending on the result returned from overlap_type different routines are used to calculate  */
/*  the TCC. The result is returned via global variables tccreal and tccimag                     */
/*                                                                          */

void TCC(double f1,double f2)
{
  int num;
  double fx1abs,fx2abs,swap,d,signedf1,signedf2;
  double g_limit[4],f_limit[4],radius[4]; /* Store limits of integration */

  signedf1=f1; signedf2=f2;
  if(f2>f1) { swap=f1; f1=f2; f2=swap; } /* f1 always > f2 */

  num=overlap_type(f1,f2);

  fx1abs=f1; if(fx1abs<0) fx1abs=fx1abs*-1;
  fx2abs=f2; if(fx2abs<0) fx2abs=fx2abs*-1;

  tccreal=0; tccimag=0;

  switch(num)
  {
    case 1:
          tccreal=0;
          break;
    case 2:
          tccreal=Area(1,1,(f1-f2));
          break;
    case 3:
          if(fx1abs<fx2abs)
          {
            tccreal=Area(1,1,(f1-f2))+Area(sigma,1,fx1abs) - (PI);
          }
          else
          {
            tccreal=Area(1,1,(f1-f2))+Area(sigma,1,fx2abs) - (PI);
          }
          break;
    case 4:
          if(fx1abs>fx2abs)
          {
            tccreal=Area(sigma,1,fx1abs);
          }
          else
          {
```

```
            tccreal=Area(sigma,1,fx2abs);
          }
          break;
    case 5:
          tccreal=PI*sigma*sigma;
          f_limit[0]=sigma;
          g_limit[0]=sigma;
          break;
    case 6:
          tccreal=Area(1,sigma,fx1abs);
          d=f1;
          f_limit[0]=(((sigma*sigma)+(d*d)-1)/(2*d));
          g_limit[0]=sqrt((sigma*sigma)-((f_limit[0])*(f_limit[0])));
          break;
    case 7:
          tccreal=Area(1,sigma,fx2abs);
          if(f2<0) {d=f2*-1;} else {d=f2;}
          f_limit[0]=-1*(((sigma*sigma)+(d*d)-1)/(2*d));
          g_limit[0]=sqrt((sigma*sigma)-((f_limit[0])*(f_limit[0])));
          g_limit[1]=sigma;
          break;
    case 8:
          tccreal=Area(1,sigma,fx1abs)+Area(1,sigma,fx2abs)-(PI*sigma*sigma);
          d=f1;
          f_limit[0]=(((sigma*sigma)+(d*d)-1)/(2*d));
          g_limit[0]=sqrt((sigma*sigma)-((f_limit[0])*(f_limit[0])));
          if(f2<0) {d=f2*-1;} else {d=f2;}
          f_limit[1]=-1*(((sigma*sigma)+(d*d)-1)/(2*d));
          g_limit[1]=sqrt((sigma*sigma)-((f_limit[1])*(f_limit[1])));
          break;
    case 9:
          tccreal=Area(1,1,(f1-f2));
          f_limit[0]=(f1+f2)/2;
          g_limit[0]=sqrt(1-((f_limit[0]-f2)*(f_limit[0]-f2)));
          break;
    case 10:
          if( (fx1abs<=1) && (fx2abs<=1) )
          {
            tccreal=1;
          }
          else
          {
            tccreal=0;
          }
          break;
  }

  if( ((num>4)&&(num<10)) && (f1!=f2) && ((defocus>.00001)||(defocus<-.00001)) ) {
Integrate_Tcc(f1,f2,f_limit,g_limit,num); }
  tccreal=tccreal;
  tccimag=tccimag;
}

/*                                                                    */
/*   TCCMAIN is called by the graphical user interface. Numerical aperature, wavelength   */
```

```
/*    illuminator information, fieldsize, and input data arrays (frequency domain) are      */
/*    transferred to the function. Results are returned via the xoutput complex array      */
/*                                                                                         */
/*                                                                                         */

void tccmain(struct xcomplex *xinput,struct xcomplex *xoutput,double xdefocus,double xfieldsize,double
                                        xsigma,double xna,double xlambda,double xsigma2,int annular)
{
  int i,ii,n,fx,m,n_index,m_index,mloc,nloc,nmloc;
  float temp_real,temp_imag,temp_tccreal,temp_tccimag;

  sigma=xsigma;
  fieldsize=xfieldsize*xna/xlambda;
  defocus=xdefocus*(2*xna*xna)/xlambda;
  if( (defocus<.000001)&&(defocus>.000001) )defocus=0;

  tcc00=(PI*sigma*sigma)-(PI*xsigma2*xsigma2);

  n_index= (1*(int)( ( (1+sigma)*fieldsize ) )) /*+ 1*/;
  m_index= ( (int)( (    2    *fieldsize ) )) /*+ 1*/;

  for(i=0;i<=MAXNUM;i++)
  {
        xoutput[i].real=0;
        xoutput[i].imag=0;
  }

  for(m=-1*m_index;m<=m_index;m++)
  {
    if(m<0) {mloc=m+MAXNUM;} else {mloc=m;}

    xoutput[mloc].real=0;
    xoutput[mloc].imag=0;

    for(n=-1*n_index;n<=n_index;n++)
    {
        if(n<0) {nloc=n+MAXNUM;} else {nloc=n;}
        if((n+m)<0) {nmloc=n+m+MAXNUM;} else {nmloc=n+m;}
        if(annular==YES)
        {
          TCC((double)(n+m)/fieldsize,(double)(n)/fieldsize);
          temp_tccreal=tccreal; temp_tccimag=tccimag;
          sigma=xsigma2;
          TCC((double)(n+m)/fieldsize,(double)(n)/fieldsize);
          tccreal=(temp_tccreal-tccreal)/tcc00;
          tccimag=(temp_tccreal-tccreal)/tcc00;
          sigma=xsigma;
        }
        else
        {
          TCC((double)(n+m)/fieldsize,(double)(n)/fieldsize);
          tccreal=tccreal/tcc00;
          tccimag=tccimag/tcc00;
        }
        temp_real = (xinput[nmloc].real*xinput[nloc].real)+(xinput[nloc].imag*xinput[nmloc].imag);
```

```
            temp_imag = (xinput[nmloc].imag*xinput[nloc].real)-(xinput[nloc].imag*xinput[nmloc].real);
            xoutput[mloc].real=xoutput[mloc].real + (temp_real*(float)(tccreal)) -
(temp_imag*(float)(tccimag));
            xoutput[mloc].imag=xoutput[mloc].imag + (temp_imag*(float)(tccreal)) +
(temp_real*(float)(tccimag));
        }
      }
}
```

Appendix V

EMGJS81.JB - 8 Level Phase Shift Mask Job

```
SLICE EDIT,14
OPTION AA=0.5, BA=0.5, PA, SA=40, VA=10, F2,3,4=5
DTITLE 1,JOE SUMMA THESIS
MTITLE 1,8 PHASE PLATE #1
ITITLE 1,gpsm934JS1
ORIENT A,ITITLE, TITLEROT=90, LOC=116000,20000
REPEAT A,17
FID 5,(W=22, WX=22, WY=22) 62500,45000,82500,45000,72500,102500
MARKTYPE 5,(A,2)
CHIP 1,(A,XYVERN1-50-01),
ROWS 15000,2,95000/15000,2,95000
CHIP 2,(1,RITLOGO-50-01)
ROWS 10000/62500
CHIP 3,(1,GCA6700-FI-05),
ROWS 62500;62500/5000;120000
CHIP 4,(1,GPSM934-JS-01),                    <- Chrome Layer
ROWS 72500/72500
CHIP 5,(2,GPSM934-JS-02),                    <- Phase Level 1
ROWS 72500/72500
CHIP 6,(3,GPSM934-JS-03),                    <- Phase Level 2
ROWS 72500/72500
CHIP 7,(4,GPSM934-JS-04),                    <- Phase Level 3
ROWS 72500/72500
CHIP 8,(1,SILMARK-00-07),                    <- Alignment Marks
ROWS 45000/62500
ROWS 45000/82500
ROWS 102500/72500
CHIP 9,(A,XYVERN1-50-02),
ROWS 15000,2,95000/15000,2,95000
END
```

EMGJSML.JB - 8 Level Microlens Array

```
SLICE EDIT,14
OPTION AA=0.5, BA=0.5, PA, SA=40, VA=10, F2,3,4=5
DTITLE 1,JOE SUMMA THESIS
MTITLE 1,441NM MICROLENS ARRAY #1
ITITLE 1,GMCRLNSJS1
ORIENT A,ITITLE, TITLEROT=90, LOC=116000,20000
REPEAT A,17
FID 5,(W=22, WX=22, WY=22) 62500,45000,82500,45000,72500,102500
MARKTYPE 5,(A,2)
CHIP 1,(A,XYVERN1-50-01),
ROWS 15000,2,95000/15000,2,95000
CHIP 2,(1,RITLOGO-50-01)
ROWS 10000/62500
CHIP 3,(1,GCA6700-FI-05),
ROWS 62500;62500/5000;120000
CHIP 4,(1,GMCRLNS-JS-01),                    <- Chrome Layer
ROWS 72500/72500
CHIP 5,(2,GMCRLNS-JS-02),                    <- Phase Level 1
ROWS 72500/72500
CHIP 6,(3,GMCRLNS-JS-03),                    <- Phase Level 2
ROWS 72500/72500
CHIP 7,(4,GMCRLNS-JS-04),                    <- Phase Level 3
ROWS 72500/72500
CHIP 8,(1,SILMARK-00-07),                    <- Alignment Marks
ROWS 45000/62500
ROWS 45000/82500
ROWS 102500/72500
CHIP 9,(A,XYVERN1-50-02),
ROWS 15000,2,95000/15000,2,95000
END
```

References

1. E. Hecht: *Optics*, 2nd edition, Chaper 7, Addison-Wesley (1987).

2. J.W. Goodman: *Introduction to Fourier Optics*, McGraw-Hill (1968).

3. H. H. Hopkins: "The concept of partial coherence in optics," *Proc. Roy. Soc.*, A, **208** (1951), 263.

4. M. Born and E. Wolf: Principles of Optics, 6th edition, Chapter 10, Pergamon Press (1980)

5. H. H. Hopkins: "On the diffraction theory of optical images," *Proc. Roy. Soc.*, A, **217** (1953), 408.

6. E. C. Kintner, "Method for the calculation of partially coherent imagery," *Applied Optics*, vol. 17, no. 17, pp. 2748, 1 September 1978.

7. E. C. Kintner, "Method for the calculation of partially coherent imagery," *Applied Optics*, vol. 17, no. 17, pp. 2747-53, 1 September 1978.

8. H. H. Hopkins: "On the diffraction theory of optical images," *Proc. Roy. Soc.*, A, **217** (1953), 409.

9. E. C. Kintner, Appendix.

10. S. Subramanian, "Rapid Calculation of Defocused Partially Coherent Images," *Applied Optics*, vol. 20, no. 10, pp. 1854-57, 15 May 1981.

11. K. K. H. Toh, "Two-Dimensional Imaging with Effects of Lens Aberration in Optical Lithography", M.S. Thesis, University of California, Berkeley, May 1988.

12. K. K. H. Toh, "Chromeless Phase-Shifted Masks: A New Approach to Phase Shifting Masks", Proceedings of BACUS Symp., Santa Clara, Sept. 26,1990.

13. H. Ohtsuka, "Conjugate Twin-Shifter for the New Phase Shift Method to High Resolution Lithography," SPIE Vol. 1463, Optical/Laser Microlithography IV, 1991.

14. M. B. Stern, "Fabricating Binary Optics: Process variables critical to optical efficiency", J. Vac. Sci. Technol., pp.3117-3121, Nov/Dec 1991.

15. A. Neureuther, SPIE vol. 470, pp. 228-232, 1984.

16. Y. Hirai, 37th Semiconductors and Integrated Circuits Technology, pp. 43-48, 1990.

17. B. Lin, "The attenuated phase-shifting mask", Solid State Technology, 43, Jan. 1992.

18. S. Wolf, *Silicon Processing for the VLSI Era*, Chapter 10, Lattice Press, 1986.

19. J.W. Coburn, J. Vac. Sci. Technol., 16, 391, 1979.